Doctoral theses at NTNU, 2018:391

Shilpa Kumari

Initiation and Propagation of Intergranular Corrosion on AA6005 Aluminium Alloy

NTNU
Norwegian University of
Science and Technology

Doctoral thesis

Shilpa Kumari

ISBN 978-82-326-357 (printed ver.)
ISBN 978-82-326-3571-9 (electronic ver.)
ISSN 1503-8181

NTNU
Norwegian University of
Science and Technology

Doctoral theses at NTNU, 2018:391

NTNU
Norwegian University of Science and Technology
Thesis for the Degree of
Philosophiae Doctor
Faculty of Natural Sciences
Department of Materials Science and
Engineering

NTNU

Shilpa Kumari

Initiation and Propagation of Intergranular Corrosion on AA6005 Aluminium Alloy

Thesis for the Degree of Philosophiae Doctor

Trondheim, December 2018

Norwegian University of Science and Technology
Faculty of Natural Sciences
Department of Materials Science and Engineering

NTNU
Norwegian University of
Science and Technology

NTNU
Norwegian University of Science and Technology

Thesis for the Degree of Philosophiae Doctor

Faculty of Natural Sciences
Department of Materials Science and Engineering

ISBN 978-82-326-3570-2 (printed ver.)
ISBN 978-82-326-3571-9 (electronic ver.)
ISSN 1503-8181

Doctoral theses at NTNU, 2018:391

Printed by NTNU Grafisk senter

Preface

This work has been performed at the Department of Materials Science and Engineering, Norwegian University of Science and Technology (NTNU), from November 2015 to October 2018. This work is part of the project Fundamentals of Intergranular Corrosion in Aluminium Alloys – FICAL (247598), a Knowledge Building Project for Industry co-financed by The Research Council of Norway (RCN), and the industrial partners Norsk Hydro, Sapa, Gränges, Benteler, and Steertec. RCN and the industrial partners are gratefully acknowledged for their financial support. The main supervisor has been Professor Kemal Nisancioglu (NTNU), with Professor Otto Lunder (SINTEF and NTNU) and Professor John Walmsley (NTNU and Cambridge University) as co-supervisors.

The author has performed all the experimental work presented in this thesis except FIB sample preparation and TEM analysis that was performed by Sigurd Wenner (SINTEF).

Trondheim, 13th November 2018

Shilpa Kumari

Acknowledgements

First of all, I would like to express my sincere gratitude to my supervisor Professor Kemal Nisancioglu, for providing me with the opportunity to carry out my PhD studies at NTNU and work on the FICAL project during the last three years. I greatly appreciate him for his kindness, patience, expertise, and willingness to assist whenever needed. It has been a great pleasure to work with him. This work would not have been accomplished without his guidance.

My sincere gratitude is extended to Professor Otto Lunder, for interesting discussions and extensive help during these years. Professor John Walmsley is highly acknowledged for providing critical comments during my entire PhD study. Sigurd Wenner deserves special attention being a dedicated researcher and electron microscopist. He made a huge contribution to the TEM results of this work.

I am grateful for being a part of the FICAL project, for having many fruitful discussions through meetings and email exchange- all of which provided a contribution to the completion of this work. Therefore, I would like to thank Randi Holmestad (Project leader), Calin Marioara, Yanjun Li, Dongdong Zhao, Jesper Friis and Adrian Lervik.

Special thanks to my officemate Bruno Burmas for our discussion about everything including even work. I would like to thank all my colleagues at NTNU for their kind help and assistance during my PhD study. Furthermore, I would like to thank all my friends for helping and supporting me.

Finally, I want to express my sincere gratitude to my parents and my siblings. Thanks for all your supports and encouragements which have given me the utmost motivation and kept me moving forward. I am very thankful to my life partner Anjan Mukherjee for his encouragement to take PhD and motivating me constantly in this adventure.

Summary

The increasing use of 6xxx series aluminium alloys (AlMgSi) in automotive applications is due to its high strength to weight ratio (enabling substantially reduced fuel consumption and CO_2 emissions than for heavier materials in use today), good extrudability and overall good corrosion resistance. Even though the 6xxx series are considered resistant to intergranular corrosion (IGC), these alloys may develop susceptibility due to unfavourable alloying and thermomechanical treatment. The objective of this thesis is to understand the mechanisms of initiation and propagation of IGC in extruded AA6005 alloy. In addition, the role of Cu on IGC mechanism and the effect of grain boundary properties on IGC were studied.

The material investigated was extruded aluminium alloy AA6005-T5 with a nominal composition of 0.64 Si, 0.21 Fe, 0.14 Cu, 0.16 Mn, 0.57 Mg in wt.%. Samples were investigated for IGC susceptibility in the as-received condition and after pretreatment of the surface (alkaline etching, metallographic polishing, and argon sputtering). The corrosion test used was a modified version of the standard BS 11846 method B, which involves immersion in acidified chloride solution for various periods in order to capture the initiation of IGC and different stages of propagation.

IGC initiated at the α-Al(Fe,Cu,Mn)Si particles located at the grain boundaries. However, these particles corroded rapidly in the test solution forming a residue of Cu, which acted as an effective external cathode for IGC. Furthermore, Cu became enriched on the Al matrix alloy surface by dealloying, shown by Glow Discharge Optical Emission Spectroscopy (GD-OES) depth profiling, which also contributes increasingly to the formation of an effective external cathode for IGC. The hypothesis that IGC propagation depended on the presence of nearly continuous nanolayer of Cu along the grain boundary (GB), probably acting as the internal cathode, and adjacent particle-free zone (PFZ), which acted as the active path for propagating IGC fissures, was verified. Coarsening of the Cu layer into discrete AlMgSiCu (Q-phase) particles, with Cu-free segments of grain boundary (GB) in between, increased the resistance against IGC by acting as barriers against fissure propagation. These particles, present as primary particles and secondary hardening phases in the grains and GBs, were relatively stable in the test solution both against anodic oxidation and as cathodic sites.

Initiation of IGC was delayed by 1 h on the as-received surface compared to the pretreated surface (10-15 min). Transmission electron microscope (TEM) analysis revealed this was due to the presence of an approximately 8 nm thick crystalline oxide layer formed during extrusion.

IGC attacked GB surfaces were exposed by tensile fracture of the corroded samples for the characterization of the fissure-wall morphology. These surfaces showed extensive crystallographic etch morphology, which is typical for etching of Al alloys in strong HCl acid, indicating the expected low pH of the IGC anolyte relative to the pH of the external bulk solution, which gave a milder micro-pitted morphology in contact with the external surface. This is along the lines required by the classical electrochemical theory of propagation of localized corrosion. Cu films along the grain boundary and the adjacent solute depleted zone were destroyed by IGC filament propagation, while Cu became enriched on the widened GB walls in the tail part of the filaments by the same dealloying mechanism as on the surface grains.

Extruded AA6005 alloy consists of inhomogeneous grain structure with the surface grains perpendicular to extrusion direction and bulk grain randomly oriented with respect to extrusion direction. In order to investigate the effect of these differences in surface and bulk grains on IGC, the as-received surface and the bulk grains exposed by milling 400 μm off the surface were tested. Surface grains were more susceptible to IGC than the bulk grains in terms of both the penetration depth and weight loss. However, the penetration depth appeared to reach a limiting value, while increased rate of lateral spreading of the IGC attack was observed. Propagation of IGC fissures was faster along the surface grains (larger grains) than along the bulk grains (tortuous boundaries).

The cause of the higher IGC rate in the surface grains compared to the bulk grains was related to the GB structure. Electron backscatter diffraction (EBSD) and TEM studies showed that IGC attack can be related to its crystallographic misorientation and GB precipitation. Low angle boundaries were resistant to IGC since they showed discrete Q-phase precipitates rather than a continuous Cu film in contrast to the high-angle GBs at the surface region. However high angle grain boundary shows segregated Cu film and is more susceptible to corrosion.

This work provides new information about the role of external and internal cathodes in initiation and propagation of IGC. It also highlights the importance of GBs properties and chemistry for IGC and manipulating these parameters can help in preventing IGC in 6xxx series.

Contents

Chapter 1 Introduction

1.1 Background

Extruded aluminium 6xxx series (AlMgSi) alloys are among the most useful engineering materials. One example is the automotive industry, where the demand for fuel efficiency without compromising the performance and vehicle size can be achieved by replacing conventional steel with aluminium alloys. Replacing the steel with lighter alloys will result in weight loss without compromising strength and reduce CO_2 emission [1]. 6xxx series alloys are preferred for applications in the automobile industry [2]. 6xxx series are characterized by good corrosion resistance, medium to high strength, compliance to surface treatment, good extrudability, relatively low associated cost and low quench sensitivity [3]. However, susceptibility to intergranular corrosion (IGC) may occur because of unfavourable alloying and thermomechanical treatment.

IGC is localized corrosion along the grain boundaries of the material and has a detrimental effect on fatigue life and mechanical properties. IGC is not readily observed as it propagates deeply into the material through narrow paths along the grain boundaries causing almost no visible damage on the surface, and hence it is difficult to detect without the aid of microscopes and specialized sample preparation [4].

Unfavourable heat treatment, e.g., slow quenching after solution heat treatment can introduce IGC [5]. The occurrence of IGC may increase due to artificial aging and reduce during overaging [5-13]. Apart from unfavourable heat treatment, alloying may introduce susceptibility to IGC, e.g., high Cu and Si content, the latter in excess of the Mg_2Si stoichiometry. It has been claimed that IGC can be avoided if the Cu content is kept below a critical value of 0.1 wt.% [14].

It is suggested that IGC is caused by a microgalvanic coupling between enriched Cu along the grain boundary (noble) and the adjacent depleted zone (active) [15], but the mechanisms of Cu segregation due to dealloying was not explained. Recent work suggests that the role of α-phase

[Al(Mn,Fe)Si] particles as cathodes is limited in the accelerated IGC test standard [16] since they corrode rapidly in the acidified chloride solution [17]. The Q-phase [AlMgSiCu] particles, which are common precipitates in Cu containing alloys, are relatively resistant to the test solution because of their Cu content. These particles also appear to be quite inert as local cathodes in promoting IGC on the 6xxx series alloy investigated [17, 18]. Therefore, IGC propagation can be sustained only by the Cu-rich grain boundary nanofilm, known to segregate along the grain boundaries as a result of underaging. IGC occurs along the adjacent solute-depleted zone, which is anodically active. Coarsening of the Cu-rich boundary layer film as discrete Q-phase particles in the T5 temper makes the material resistant to IGC. The validity of the accelerated test in relation to service exposure is questioned since the external cathodes are not expected to corrode in the absence of an acidified chloride environment [17]. Microstructure characteristics such as grain size, precipitates along the grain boundary and grain boundary misorientation is also known to affect IGC susceptibility [19-21].

The foregoing background motivates us to analyse the role of external and internal cathodes in initiation and propagation of IGC in detail in acid solution and to investigate the role of grain boundary chemistry and microstructure in IGC propagation.

1.2 Objectives

The main objective of the present work is to understand the mechanisms of initiation and propagation of IGC in the extruded AA6005 alloy, nominally containing (by weight) 0.64% Si, 0.57% Mg, 0.14% Cu, 0.21% Fe, 0.16% Mn. The influence of surface microstructure and the role of external cathodes on IGC initiation and propagation are of particular interest for understanding the corrosion mechanism. A further objective is to perform the surface analytical studies of corroded IGC fissure to understand localized surface morphology and chemistry to understand the effect of grain boundary characteristics on IGC.

1.3 Structure of the thesis

Chapter 2 consists of a literature review of the relevant work for IGC of 6xxx alloys to elaborate on the preceding background and validate the objective of the thesis. The experimental work is organized in four chapters, 3 through 6.

Chapter 3 presents the role of different pretreatment and intermetallic phases in the initiation of IGC. The oxide layer formed on extruded AA6005 alloy is thoroughly investigated. In chapter 4, the role of external cathodes, in particular in the form of Cu film and nanoparticles segregated by dealloying during corrosion is investigated, in combination with the chemistry of the grain surface along the IGC fissure trail, using post mortem opening of the fissure tip by fracturing. Effect of grain structure and different corrosion times on maximum depth of propagation on IGC is explored in chapter 5. Chapter 6 presents an investigation of the effect of grain boundary structure and chemistry on IGC. It also presents the role of high and low angle grain boundary on IGC. An overall discussion and suggestion for future work are included in chapter 7. Overall conclusions about the significance of the results obtained in the thesis are presented in chapter 8.

1.4 References

[1] H. Helms, U. Lambrecht, Energy savings by light-weighting. Final report for the International Aluminium Institute, *Institute for Energy and Environmental Research,* Heidelberg, Germany (**2003**).

[2] W.S. Miller, L. Zhuang, J. Bottema, A. Wittebrood, P. De Smet, A. Haszler, A. Vieregge, Recent development in aluminium alloys for the automotive industry, *Materials Science and Engineering A,* 280 (**2000**) 37-49.

[3] D.G. Altenpohl, Aluminium viewed from within: an introduction into the metallurgy of aluminium fabrication, *Aluminium-Verlag*, Düsseldorf, Germany (**1982**).

[4] J.R. Davis, Corrosion of aluminum and aluminum alloys, *ASM International*, Metals Park, OH, USA (**1999**).

[5] D.O. Sprowls, R.H. Brown, Stress corrosion mechanisms for alumnium alloys, *Proceedings of fundamental aspects of stress corrosion cracking,* The Ohio State University, OH, USA (**1969**) 466-506.

[6] J.E. Hatch, Aluminum properties and physical metallurgy, *ASM International,* Metals Park, OH, USA (**1984**).

[7] H.P. Godard, The corrosion of light metals, *John Wiley & Sons Inc*, New York, USA (**1967**).

[8] A.K. Bhattamishra, K. Lal, Microstructural studies on the effect of Si and Cr on the intergranular corrosion in Al-Mg-Si alloys, *Materials & Design,* 18 (**1997**) 25-28.

[9] A.K. Bhattamishra, K. Lal, Influence of ageing on corrosion behaviour of Al-Mg-Si alloys in chloride and acid media, *Zeitschrift fur Metallkunde,* 89 (**1998**) 793-796.

[10] V. Guillaumin, G. Mankowski, Influence of overaging treatment on localized corrosion of Al 6056, *Corrosion Science,* 56 (**2000**) 12-23.

[11] G. Svenningsen, M.H. Larsen, J.H. Nordlien, K. Nisancioglu, Effect of high temperature heat treatment on intergranular corrosion of AlMgSi(Cu) model alloy, *Corrosion Science,* 48 (**2006**) 258-272.

[12] R. Ambat, A.J. Davenport, G.M. Scamans, A. Afseth, Effect of iron-containing intermetallic particles on the corrosion behaviour of aluminium, *Corrosion Science,* 48 (**2006**) 3455-3471.

[13] G. Svenningsen, M.H. Larsen, J.C. Walmsley, J.H. Nordlien, K. Nisancioglu, Effect of artificial aging on intergranular corrosion of extruded AlMgSi alloy with small Cu content, *Corrosion Science,* 48 (**2006**) 1528-1543.

[14] G. Svenningsen, J.E. Lein, A. Bjørgum, J.H. Nordlien, Y. Yu, K. Nisancioglu, Effect of low copper content and heat treatment on intergranular corrosion of model AlMgSi alloys, *Corrosion Science,* 48 (**2006**) 226-242.

[15] G. Svenningsen, M.H. Larsen, J.H. Nordlien, K. Nisancioglu, Effect of thermomechanical history on intergranular corrosion of extruded AlMgSi(Cu) model alloy, *Corrosion Science,* 48 (**2006**) 3969-3987.

[16] Determination of resistance to IGC of solution heat-treatable aluminium alloys, Standard, BS 11846, *British Standards Institution,* (**1995**).

[17] K. Shimizu, K. Nisancioglu, High resolution SEM investigation of intercrystalline corrosion on 6000-Series aluminum alloy with low copper content, *ECS Electrochemistry Letters,* 3 (**2014**) C29-C31.

[18] S.K. Kairy, P.A. Rometsch, C.H.J. Davies, N. Birbilis, On the electrochemical and quasi in situ corrosion response of the Q-Phase (AlxCuyMgzSiw) intermetallic particle in 6xxx series aluminum alloys, *Corrosion Science,* 73 (**2016**) 87-99.

[19] R. Zhang, R.K. Gupta, C.H.J. Davies, A.M. Hodge, M. Tort, K. Xia, N. Birbilis, The influence of grain size and grain orientation on sensitization in AA5083, *Corrosion Science,* 72 (**2015**) 160-168.

[20] M. Yang, S. Liu, X. He, J. Wang, Y. Kong, P. Zhao, K. Li, Y. Du, Effect of stamping deformation on microstructure and properties evolution of an Al–Mg–Si–Cu alloy for automotive panels, *Journal of Materials Science,* 52 (**2017**) 5569-5581.

[21] T. Minoda, H. Yoshida, Effect of grain boundary characteristics on intergranular corrosion resistance of 6061 aluminum alloy extrusion, *Metallurgical and Materials Transactions A,* 33 (**2002**) 2891-2898.

Chapter 2 Literature review

2.1 Introduction

This thesis deals with the mechanism of initiation and propagation of IGC on 6xxx series aluminium alloys, in particular, the extruded alloy AA6005-T5, whose composition is given in Table 2.1. T5 is the temper, indicating that the material was aged artificially to maximum hardness after extrusion.

Table 2.1 Composition of the aluminium alloy AA6005-T5 (wt.%).

	Al	Si	Fe	Cu	Mn	Mg
6005-T5	Balance	0.64	0.21	0.14	0.16	0.57

The purpose of this chapter is to give a brief but general review of the metallurgical, chemical and corrosion properties of 6xxx series (AlMgSi) alloys as the necessary background to meet the above objective. Properties of other alloy groups, especially in the 5xxx and 7xxx are also referred to for comparison or if relevant to the properties of 6xxx alloys. 6xxx series alloys are, in general, considered to be resistant to IGC. If it occurs, IGC is often related to the grain boundary microstructure and chemistry. The type of intermetallic phases and their distribution in the matrix alloy are often important in initiation and propagation of localized corrosion on aluminium alloys. In particular, the use of small amounts of Cu on these alloys for increased strength has been detrimental in recent occurrence of IGC [1]. In addition, the effect of geometrical factors in the microstructure, such as grain size, geometry and orientation is supposed to have an influence on the propagation of IGC [2]. Finally, thermal and chemical processing during the fabrication of specific components and products need to be discussed since such processes may modify the grain boundary microstructure, which may be undesirable for IGC resistance [3-5].

2.2 Metallurgical properties of AlMgSi(Cu) alloys relevant to corrosion

Wrought 6xxx series alloys are heat treatable with Mg and Si as their principal alloying elements [6]. The strength of these alloys is increased by increasing the Si, Mg and Cu concentrations, as these are the principal components of the hardening phases of type Mg_2Si and AlMgSiCu (Q-phase) [7]. Iron is always present as one of the main impurities in commercial aluminium alloys. It usually has a negative effect on the alloy's resistance to localized corrosion. Alloying with small amounts of Mn and Cr is often used to reduce the negative effect of Fe. The mechanisms are reviewed further below.

2.2.1 Microstructure of extrusions

Extrusion of aluminium is a deformation process performed at high temperature. Extruded profiles are manufactured by pressing a pre-heated billet through a precision die. During hot extrusion surface imperfections, such as peripheral coarse grains (PCG), develop. These are detrimental to the strength, toughness, formability and weldability [8, 9]. Extruded 6xxx alloys often show duplex grain structure consisting of an elongated or fibrous grain structure in the core of the material and an equiaxed layer near the surface [10-12]. Possible factors, which contribute are alloying, thermomechanical treatment and deformation [10]. The surface layer consists of randomly oriented grains, which generally have high angle grain boundaries as compared to the core grain structure [2]. Presence of thick recrystallized surface layer is known to be harmful (due to material fracture) to the mechanical performance of the final product [13].

2.2.2 Intermetallic phases in AlMgSi alloys

The solid solubility of iron in molten aluminium is about 0.04 wt.% at 655 °C [6]. Thus most of the iron present appears in the form of Fe containing intermetallics, such as α-Al(Fe,Mn)Si, Al_5FeSi and Al_3Fe phases, which are formed during casting and homogenization of 6xxx Al alloys.

In alloys which contain Mn, the cubic α-Al(Fe,Mn)Si phase becomes stable with an approximate stoichiometry of $Al_{12}(Fe,Mn)_3Si$, in which the Mn atoms are interchangeable with the Fe or Cu atoms [6, 14]. The corrosion potential of α-phase in 0.1 M NaCl is -0.3 V [15], with respect to saturated calomel electrode (SCE). However, the surface condition of the intermetallics may change as a function of the variable compositions of the transition elements and time of exposure to the test solution, the latter because of selective corrosion of the active components aluminium and magnesium [16].

In AlMgSi alloys, the formation of the equilibrium hardening phase Mg_2Si occurs through a number of metastable phases in the precipitation sequence.

The precipitation sequence of AlMgSi alloys is generally written as [17, 18]:

SSSS → Atomic clusters → GP-zones → β'' (Mg_5Si_6) → β' (Mg_2Si), Q′ → Q

The Super Saturated Solid Solution (SSSS) is obtained by performing solution heat treatment (SHT) of the alloys. As described above, the first step in the precipitation sequence for 6xxx alloys is the formation of the Guinier Preston (GP) zones. It is well known that the metastable GP zones dissolve in the presence of a more stable phase, and this causes the formation of precipitates free zones (PFZs) around the stable phases (such as the Q-phase) and grain boundaries (GBs) [19]. The PFZs along the GBs are formed mainly by the depletion of vacancies or solute atoms at GBs. This is a diffusion controlled process, and hence, the width of PFZ strongly depends on the diffusivity of vacancies or solute atoms at GBs [20-23]. These PFZs will then have different electrochemical properties compared to the grain boundary precipitates and the surrounding matrix.

The crystal structure of the Q-phase is hexagonal [6]. Limited information available about the electrochemical properties of the Q-phase indicates that it is nobler than the aluminium matrix and the Θ-phase (Al_2Cu) [24].

The precipitation sequence in AlMgSi(Cu) alloys is quite complex due to simultaneous formation of several metastable phases [25-28]. The presence of Cu was claimed to enhance the precipitation kinetics of the metastable β'' phase [25, 29]. In alloys with low Cu content, metastable versions of the Q-phase were claimed to contribute to the hardening process [26].

2.2.3 Grain boundary misorientation

The solidification process is governed by the kinetics of grain nucleation and growth. Grains grow in random orientations giving rise to misoriented grain boundaries upon joining. A grain boundary is classified in two categories based on the orientations of the adjacent grains [30]. If the misorientation between the grains is < 15 ° the grain boundary is classified as low angle grain boundary LAGB, and grain boundary with misorientation > 15 ° is termed as high angle grain boundary HAGB [31]. The interfacial energy between the grain boundaries increases with misorientation because the atoms become less regularly bonded [32]. Therefore, the HAGBs are high energy sites relative to the LAGBs, and segregation of alloying elements at HAGBs will be more favourable than at the LAGBs.

2.3 IGC mechanisms

2.3.1 Electrochemical factors

IGC on Cu containing AA6005 alloy initiates at intermetallic phases exposed at the surface [33] and propagates into the bulk material along the GBs supporting active PFZ and noble Cu film [4, 5, 11, 34, 35]. It has been claimed to occur by microgalvanic coupling between the PFZ and Cu film [1, 3-5, 34, 35]. Participation of noble areas on the external surface (external cathodes), such as intermetallic particles, was ruled out for accelerated IGC testing in acidified chloride solution [35]. The alloy was most susceptible to IGC in the underaged T4 condition, which favoured segregation of the Cu-rich nanolayer. However, in the peak-aged T6 and overaged T7 conditions, nanolayer coarsened into larger and discrete Cu precipitation along the GBs, thereby reducing the susceptibility to IGC [5]. This observation has recently been verified by Kairy et al., and with the help of atom probe tomography, the thickness of the segregated Cu nanofilm was shown to be about 2 nm [36].

IGC of 6xxx alloys has also been related to the dissolution of a continuous network of anodic Mg_2Si precipitates at the grain boundary [37, 38]. The Mg_2Si-precipitates become enriched with Si as Mg is preferentially dissolved, thereby transforming the precipitates from active to noble. However, this mechanism is unable to explain why unbalanced alloys (which contain Si in excess of that required to form stoichiometric Mg_2Si) are more susceptible than the balanced alloys (stoichiometric content of Mg/Si ratio for precipitation of the Mg_2Si). Additionally, Si is not regarded as an efficient cathode in aluminium alloys, based on the slow reaction kinetics on a fairly inert surface [35, 39, 40].

Stress corrosion cracking (SCC) of high strength aluminium alloys is an intergranular phenomenon [41], and two different mechanisms [anodic dissolution and hydrogen embrittlement (HE)] are proposed [42]. Furthermore, the mechanisms of IGC and SCC in Al alloys have been suggested to be related [43-46]. However, recent SCC data so far for the 6xxx series failed to show any HE effect or any significant susceptibility of 6xxx series to SCC [12]. These results thus suggest that IGC on 6xxx alloys in general [47] and on AA6005 [12] in particular is essentially an electrochemical process affected by certain microstructural factors to be discussed further below.

2.3.2 Effect of microstructure

Possibly related to the microstructural differences between the surface and bulk, IGC was observed to occur on the surface of 6061 alloy, while little IGC occurred at the center plane [2]. The difference was attributed to the high angle grain boundaries of the surface as opposed to low angle boundaries at the center. The effect of GB microstructure, in particular geometrical (size and orientation), on the IGC of 6xxx series alloys is a little investigated subject despite its possible significance, as shown to be the case for other types of alloys, as reviewed briefly below.

Glenn et al. claimed for the AA2024 alloy that IGC spread laterally at the outset. With increasing time, extensive grain attack occurred [48]. Yan et al. have studied correlation of grain boundary misorientation with susceptibility of IGC in Al- 5.3 wt.% Mg alloy [49]. High angle grain boundaries were more susceptible to IGC than the low angle grain boundaries for different aluminium alloys, e.g., AA5182 (Al-4.5%Mg), AA5083 (Al-4.4%Mg-0.5%Mn), AA7021 (5.0-6.0%Zn-1.2-1.8%Mg-0.4%Fe-0.25%Cu-0.25%Si), and AA7046 (6.6-7.6%Zn-1.0-1.6%Mg, 0.4%Fe, 0.25%Cu, 0.20%Si), all by weight [49-51]. IGC growth rate was fastest in the long transverse direction and the slowest in the short transverse direction [52, 53], as shown by both experimental [53] and modelling results [52]. Kairy et al. have shown in recent studies that the type and electrochemical behaviour of grain boundary precipitates are the dominant factors in determining whether GBs are susceptible to IGC or not [54].

The foregoing review indicates that the IGC propagation depends on factors such as grain texture, segregation, precipitation, development of PFZ along the grain boundary and grain boundary misorientation. These factors should therefore be investigated in detail for understanding the mechanism of IGC.

2.3.3 Effect of common alloying and impurity elements on IGC susceptibility

Mg and Si: The 6xxx series are known to be heat treatable [26] because the main alloying elements Mg and Si precipitate as the hardening phase Mg_2Si (β phase) by artificial aging. The alloys, in which the alloyed Mg to Si ratio by weight is equal to the stoichiometric ratio 1.73 are called "balanced", while those with Si in excess of what is required to form the Mg_2Si precipitate are known as "unbalanced" alloys [26, 55]. Although the solubility of Mg in Al is high (maximum 18.9 at. % at the eutectic temperature of 450 °C [56]), its concentration in 6xxx series alloys is normally less than 1 wt.%, and this has little influence on the corrosion potential. However, while the solubility of Si (about 1.5 at.% at 577 °C [57]) is much less, Si concentrations up to 1 wt.% are not uncommon for increasing the strength [58]. Such alloys are normally of the unbalanced type and considered susceptible to IGC in comparison to the balanced alloys [35, 59]. The unbalanced alloys with excess Si normally have Si-depleted zones along the grain boundaries, which are electrochemically more active than the grain bodies with higher Si. Elemental Si can also precipitate along the grain boundaries by heat treatment, reducing the amount of Si in the depleted zones. This continuous, active depleted area along the grain boundary can make the material susceptible to IGC [59]. Similar to Si, Mg also gets depleted along the grain boundary [59].

Cu: Cu may be added to 6xxx series alloys to increase their hardness [17]. It is well known that the susceptibility to IGC increases as the Cu content increases [37, 60]. The maximum solid solubility of Cu in aluminium drops from 5.7 wt.% at 548 °C [6, 61]. Cu containing precipitates or phases are formed from supersaturated solid solution as a result of slow cooling from high temperature. These phases (e.g., Q-phase) are normally considered to be efficient cathodic sites around the particles, The Al matrix becomes depleted of Cu as a result of Q-phase precipitation, and hence these areas become an active site, which may cause IGC in the presence of corrosive environment.

There is disagreement about the critical level of Cu content for IGC susceptibility. Some sources claim that Cu content up to 0.1- 0.2 wt.% is acceptable [62], while some report levels as high as 0.4 wt.% [6]. In contrast to these results, smaller Cu contents (0.01-0.13 wt.%) were shown to cause IGC [1, 3, 4, 63]. More detailed recent investigations suggest that the small Cu content is more important than excess Si in causing IGC of 6xxx series alloys. [35, 64, 65].

Mn: Mn is generally added to 6xxx series alloys to control the grain size. Grain size increases with the Mn content. Since the solubility of Mn in the Al alloy is limited, it forms various Al-based intermetallic compounds in the alloy [66].

Mn is believed to improve the corrosion resistance by increasing the Mn:Fe ratio. This reduces the potential difference between the Fe-rich intermetallics and the matrix [6, 67]. In the absence of Mn, noble phases such as Al_3Fe and Al_6Fe are formed. The added presence of Mn causes precipitation of the less noble AlMnFe phases. Moreover, the AlMnFe phases have a significant solubility for Si, which reduces excess Si in solid solution, thereby improving the resistance of the alloy to IGC. Apart from this positive effect on the intermetallic particles, Mn in solid solution increases the nobility of the Al matrix, thereby reducing the potential difference between the intermetallics and the matrix to give even better corrosion resistance.

The presence of **Cr** as an alloying element has effects which are very similar to those of Mn.

Fe: Fe is always present in commercial aluminium alloys, usually as impurity introduced during primary production and recycling. The solubility of Fe in Al is very low (around 0.04 wt.% at 655 °C and nearly zero at room temperature). As a result, most of the iron present in the alloy precipitates as intermetallic phases in combination with aluminium and other phases [6, 68]. The presence of iron-containing intermetallic particles has a negative effect on the corrosion resistance despite the reduction effect by the addition of Mn, Cr and Si [67-69]. Fe containing intermetallic phases are uniformly distributed throughout the metal as they are formed during casting and homogenization [70].

2.3.4 Dealloying

Dealloying refers to the selective removal of one or more less noble elements from an alloy through a corrosion mechanism. Due to dealloying, the noble elements such as Cu and Fe may become enriched in the intermetallic particles, and their cathodic behaviour may become enhanced. In 2xxx series S-phase (Al_2CuMg) particles are initially more active than the Al solid-solution alloy. Due to selective dissolution of magnesium and aluminium, they become enriched in Cu, thereby ennobling the particles. Further, Cu rich remnants act as cathodes and form a galvanic couple with the adjacent matrix which leads to localized corrosion [71, 72]. When these Cu rich remnants encountered a grain boundary, corrosion developed preferentially along the grain boundary and IGC started.

2.3.5 Effect of thermomechanical history

In age hardening alloys, the peak-strength T6 temper is considered to be most susceptible to IGC [7, 37, 73-76]. This is related to the grain boundary precipitation of intermetallic phases in the course of artificial ageing.

IGC susceptibility of the AA6005 analogue AlMgSiCu alloys (with the nominal composition in wt.% 0.57 Mg, 0.62 Si, 0.13 Cu, 0.21 Fe, 0.21 Mn) is governed by cooling rate after extrusion and aging. Slow cooling in air resulted in the most susceptible condition in the naturally aged condition because precipitation of Cu as continuous GB film occurred under such conditions, as shown schematically in Fig. 2.1. Further to maximum hardness T6, temper coarsened the film into discrete Q-phase (or precursors) particles, which eliminated IGC. Overaging was, in general, concluded as beneficial in reducing the IGC susceptibility though it introduced pitting corrosion due to continuing coarsening of the Q-phase [1, 3-5, 74, 77-81].

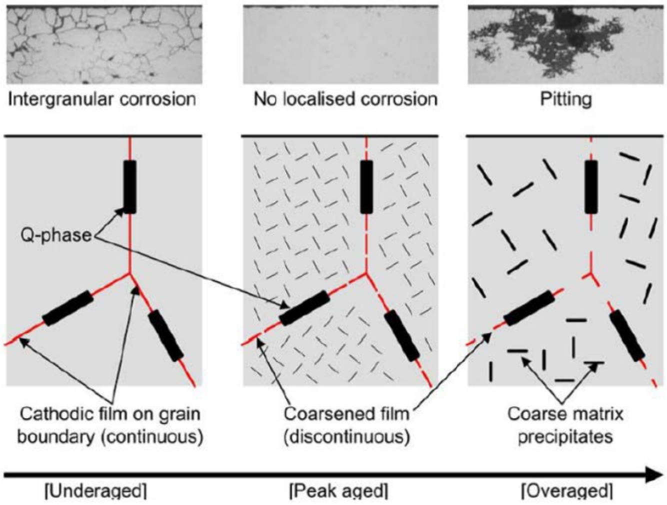

Fig. 2.1 Conceptual sketch of the effect of aging on the microstructure and corrosion mode in a 6xxx alloy [5].

2.4 Testing for IGC susceptibility

Field tests, involving exposure in service environments, such as marine, seawater and industrial environments, is commonly used for IGC testing [80, 82-84]. In addition, a number of accelerated tests have been developed. These tests involve immersion in aqueous NaCl solutions containing either H_2O_2 (ASTM G110, MIL-H-6088) or HCl (BS ISO 11846 method B) [73, 85, 86]. The solution containing HCl is more aggressive than that containing H_2O_2. Due to this reason BS ISO 11846 is preferred for 6xxx series while ASTM G110 is mostly used for 2xxx and 7xxx alloys [85, 87]. The tests typically involve degreasing and etching before immersion to remove surface oxides and contamination. Although these tests are highly accelerated and aggressive relative to the normal service exposure, they are claimed to give consistent results in evaluating whether an alloy is susceptible to IGC or not, and for ranking alloys qualitatively in terms of IGC resistance. Moreover, the materials, which do not show IGC in accordance with these tests, are likely to be resistant in much milder service exposure [1].

2.5 Discussion

Thermomechanical treatment, alloying and grain boundary characteristics are the most important factors affecting IGC of 6xxx series alloys. Effect of thermomechanical treatment and alloying on IGC has been documented to a certain extent, with contradicting results, such as the effect of aging temper on resistance against IGC. Yet, in relation to this, the information about the effect of grain boundary properties on IGC as a function of the foregoing factors is very limited. In addition, the above review suggests that there is a need for a better understanding of IGC propagation, especially in clarifying the role of Cu and electrochemical factors.

Despite the availability of literature on initiation of IGC [33, 88, 89], the available results have to be confirmed, especially information about the effect of surface microstructure and chemistry. In recent work [33] the role of α-phase particles as cathodes was suggested to be limited as they dissolve in the acidified chloride accelerated test solution. The importance of external vs. internal cathodes in IGC initiation and propagation is not clear. The grain boundary structure and chemistry of AlMgSiCu alloys of present interest and modification of these during IGC, along with the evolution of the solution chemistry in the IGC fissures, are not too well documented. These subjects need further investigation.

In addition, the above study indicated that there is little work on the effect of grain boundary misorientation on 6xxx series alloys in relation to the 2xxx and 5xxx series. It is known that the grain boundary misorientation can affect the formation of grain boundary precipitates and PFZs and thereby influence the IGC properties. Therefore, the detailed further study of the possible effects of these factors on the grain boundary microstructure in AA6005 alloy and their effect on IGC properties is required.

2.6 References

[1] G. Svenningsen, J.E. Lein, A. Bjørgum, J.H. Nordlien, Y. Yu, K. Nisancioglu, Effect of low copper content and heat treatment on intergranular corrosion of model AlMgSi alloys, *Corrosion Science,* 48 (**2006**) 226-242.

[2] T. Minoda, H. Yoshida, Effect of grain boundary characteristics on intergranular corrosion resistance of 6061 aluminum alloy extrusion, *Metallurgical and Materials Transactions A,* 33 (**2002**) 2891-2898.

[3] G. Svenningsen, M.H. Larsen, J.H. Nordlien, K. Nisancioglu, Effect of high temperature heat treatment on intergranular corrosion of AlMgSi(Cu) model alloy, *Corrosion Science,* 48 (**2006**) 258-272.

[4] G. Svenningsen, M.H. Larsen, J.H. Nordlien, K. Nisancioglu, Effect of thermomechanical history on intergranular corrosion of extruded AlMgSi(Cu) model alloy, *Corrosion Science,* 48 (**2006**) 3969-3987.

[5] G. Svenningsen, M.H. Larsen, J.C. Walmsley, J.H. Nordlien, K. Nisancioglu, Effect of artificial aging on intergranular corrosion of extruded AlMgSi alloy with small Cu content, *Corrosion Science,* 48 (**2006**) 1528-1543.

[6] L.F. Mondolfo, Aluminum alloys structure and properties, *Butterworth Inc,* London, UK (**1976**).

[7] J.E. Hatch, Aluminum properties and physical metallurgy, *ASM International,* Metals Park, OH, USA (**1984**).

[8] W.H. Van Geertruyden, H.M. Browne, W.Z. Misiolek, P.T. Wang, Evolution of surface recrystallization during indirect extrusion of 6xxx aluminum alloys, *Metallurgical and Materials Transactions A,* 36 (**2005**) 1049-1056.

[9] T. Furu, H.E. Vatne, Grain structure control of flat extruded AA6082 alloy, *Materials Science Forum,* 331-337 (**2000**) 843-848.

[10] K.O. Pedersen, O.G. Lademo, T. Berstad, T. Furu, O.S. Hopperstad, Influence of texture and grain structure on strain localisation and formability for AlMgSi alloys, *Journal of Materials Processing Technology,* 200 (**2008**) 77-93.

[11] M.H. Larsen, Effect of composition and thermomechanical processing on the Intergranular corrosion of AA6000 aluminium alloys, *NTNU PhD Thesis,* (**2010**).

[12] D.J. Seguin, Intergranular corrosion and stress corrosion cracking of extruded AA6005A, *Michigan Technological University PhD Thesis,* (**2013**).

[13] Y. Birol, Impact of partial recrystallization on the performance of 6005A tube extrusions, *Engineering Failure Analysis,* 17 (**2010**) 1110-1116.

[14] P. Donnadieu, G. Lapasset, T.H. Sanders, Manganese induced ordering in the alpha (Al-Mn-Fe-Si) approximant phase, *Philosophical Magazine Letters,* 70 (**1994**) 319-326.

[15] O. Lunder, C. Simensen, Y. Yu, K. Nisancioglu, Formation and characterisation of Ti–Zr based conversion layers on AA6060 aluminium, *Surface and Coatings Technology,* 184 (**2004**) 278-290.

[16] K. Nisancioglu, Electrochemical behavior of aluminum-base intermetallics containing iron, *Journal of the Electrochemical Society,* 137 (**1990**) 69-77.

[17] C.D. Marioara, S.J. Andersen, T.N. Stene, H. Hasting, J. Walmsley, A.T.J. Van Helvoort, R. Holmestad, The effect of Cu on precipitation in Al–Mg–Si alloys, *Philosophical Magazine,* 87 (**2007**) 3385-3413.

[18] G.A. Edwards, K. Stiller, G.L. Dunlop, M.J. Couper, The precipitation sequence in Al–Mg–Si alloys, *Acta Materialia,* 46 (**1998**) 3893-3904.

[19] J.R. Davis, Corrosion of aluminum and aluminum alloys, *ASM International*, Metals Park, OH, USA (**1999**).

[20] D.W. Pashley, M.H. Jacobs, J.T. Vietz, The basic processes affecting two-step ageing in an Al-Mg-Si alloy, *Philosophical Magazine,* 16 (**1967**) 51-76.

[21] Z.W. Huang, M.H. Loretto, R.E. Smallman, J. White, The mechanism of nucleation and precipitation in 7075-0.7 Li Alloy, *Acta Metallurgica et Materialia,* 42 (**1994**) 549-559.

[22] J.K. Park, A.J. Ardell, Microchemical analysis of precipitate free zones in 7075-A1 in the T6, T7 and RRA tempers, *Acta Metallurgica et Materialia,* 39 (**1991**) 591-598.

[23] K.K. Soni, D.B. Williams, J.M. Chabala, R. Levi-Setti, D.E. Newbury, Electron and ion microscopy studies of Fe-rich second-phase particles in Al-Li alloys, *Acta Metallurgica et Materialia,* 40 (**1992**) 663-671.

[24] S.K. Kairy, P.A. Rometsch, C.H.J. Davies, N. Birbilis, On the electrochemical and quasi in situ corrosion response of the Q-Phase (AlxCuyMgzSiw) intermetallic particle in 6xxx series aluminum alloys, *Corrosion Science,* 73 (**2016**) 87-99.

[25] D.G. Eskin, Decomposition of supersaturated solid solutions in Al–Cu–Mg–Si alloys, *Journal of Materials Science,* 38 (**2003**) 279-290.

[26] D.J. Chakrabarti, D.E. Laughlin, Phase relations and precipitation in Al–Mg–Si alloys with Cu additions, *Progress in Materials Science,* 49 (**2004**) 389-410.

[27] C. Cayron, P.A. Buffat, Transmission electron microscopy study of the β′ phase (Al–Mg–Si alloys) and QC phase (Al–Cu–Mg–Si alloys): ordering mechanism and crystallographic structure, *Acta Materialia,* 48 (**2000**) 2639-2653.

[28] C. Cayron, L. Sagalowicz, O. Beffort, P.A. Buffat, Structural phase transition in Al-Cu-Mg-Si alloys by transmission electron microscopy study on an Al-4 wt% Cu-1 wt% Mg-Ag alloy reinforced by SiC particles, *Philosophical Magazine A,* 79 (**1999**) 2833-2851.

[29] D.J. Chakrabarti, B.K. Cheong, D.E. Laughlin, Precipitation in Al-Mg-Si-Cu alloys and the role of the Q phase and its precursors, *Automotive Alloys, TMS,* Warrendale, USA (**1998**) 27-44.

[30] D. McLean, Grain boundaries in metals, *Oxford University Press,* London, UK (**1957**).

[31] P. Lejcek, Grain boundary segregation in metals, *Springer Series in Materials Science*, New York, USA (**2010**).

[32] W.D. Callister, D.G. Rethwisch, Materials science and engineering, *John Wiley & Sons,* New York, USA (**2011**).

[33] K. Shimizu, K. Nisancioglu, High resolution SEM investigation of intercrystalline corrosion on 6000-Series aluminum alloy with low copper content, *ECS Electrochemistry Letters,* 3 (**2014**) C29-C31.

[34] M.H. Larsen, J.C. Walmsley, O. Lunder, R.H. Mathiesen, K. Nisancioglu, Intergranular corrosion of copper-containing AA6xxx AlMgSi aluminum alloys, *Journal of the Electrochemical Society,* 155 (**2008**) C550-C556.

[35] M.H. Larsen, J.C. Walmsley, O. Lunder, K. Nisancioglu, Effect of excess silicon and small copper content on intergranular corrosion of 6000-series aluminum alloys, *Journal of the electrochemical society,* 157 (**2010**) C61-C68.

[36] S.K. Kairy, T. Alam, P.A. Rometsch, C.H.J. Davies, R. Banerjee, N. Birbilis, Understanding the origins of intergranular corrosion in copper-containing Al-Mg-Si alloys, *Metallurgical and Materials Transactions A,* 47a (**2016**) 985-989.

[37] K. Yamaguchi, K. Tohma, The effect of Cu content on susceptibility to intergranular corrosion of Al-Mg-Si, *Japan Institute of Light Metals,* 47 (**1997**) 285-291.

[38] F.l. Zeng, Z.l. Wei, J.f. Li, C.x. Li, T. Xing, Z. Zhang, Z.q. Zheng, Corrosion mechanism associated with Mg2Si and Si particles in Al–Mg–Si alloys, *Transactions of Nonferrous Metals Society of China,* 21 (**2011**) 2559-2567.

[39] K. Mizuno, A. Nylund, I. Olefjord, Surface reactions during pickling of an aluminium–magnesium–silicon alloy in phosphoric acid, *Corrosion Science,* 43 (**2001**) 381-396.

[40] S. Tierce, N. Pebere, C. Blanc, C. Casenave, G. Mankowski, H. Robidou, Corrosion behaviour of brazing material AA4343, *Electrochimica Acta,* 52 (**2006**) 1092-1100.

[41] R.H. Jones, Stress Corrosion Cracking in ASM Handbook, *ASM International,* Metals Park, OH, USA (**2003**) 346-366.

[42] T.D. Burleigh, The postulated mechanisms for stress-corrosion cracking of aluminum alloys-a review of the literature 1980-1989, *Corrosion Science,* 47 (**1991**) 89-98.

[43] X.D. Liu, G.S. Frankel, B. Zoofan, S.I. Rokhlin, Effect of applied tensile stress on intergranular corrosion of AA2024-T3, *Corrosion Science,* 46 (**2004**) 405-425.

[44] X.D. Liu, G.S. Frankel, B. Zoofan, S.I. Rokhlin, In-situ observation of intergranular stress corrosion cracking in AA2024-T3 under constant load conditions, *Corrosion Science,* 49 (**2007**) 139-148.

[45] S. Dymek, M. Dollar, TEM investigation of age-hardenable AA 2519 alloy subjected to stress corrosion cracking tests, *Materials Chemistry and Physics,* 81 (**2003**) 286-288.

[46] M.O. Speidel, Stress corrosion cracking of aluminum alloys, *Metallurgical Transactions A,* 6 (**1975**) 631-651.

[47] K.F. Veium, Effect of cathodic polarization on the susceptibility to hydrogen embrittlement in 5xxx, 6xxx and 7xxx series aluminium alloys, *NTNU*, Master Thesis (**2015**).

[48] A.M. Glenn, T.H. Muster, C. Luo, X. Zhou, G.E. Thompson, A. Boag, A.E. Hughes, Corrosion of AA2024-T3 part III: propagation, *Corrosion Science,* 53 (**2011**) 40-50.

[49] J. Yan, N.M. Heckman, L. Velasco, A.M. Hodge, Improve sensitization and corrosion resistance of an Al-Mg alloy by optimization of grain boundaries, *Scientific Reports,* 6 (**2016**) 26870.

[50] A.J. Davenport, Y. Yuan, R. Ambat, B.J. Connolly, M. Strangwood, A. Afseth, G.M. Scamans, Intergranular corrosion and stress corrosion cracking of sensitised AA5182, *Materials Science Forum,* 519-521 (**2006**) 641-646.

[51] A. Cassell, G.E. Thompson, X.R. Zhou, T. Hashimoto, G. Scamans, Relating grain misorientation to the corrosion behaviour of low copper 7xxx aluminium alloys, *Materials Science Forum,* 765 (**2013**) 623-628.

[52] S. Zhao, D.A. Wolfe, T.S. Huang, G.S. Frankel, Generalized model for IGC growth in aluminum alloys, *Journal of Statistical Planning and Inference,* 137 (**2007**) 2405-2412.

[53] T.S. Huang, G.S. Frankel, Intergranular corrosion morphology and growth kinetics in AA7075 and AA7178, *Pits and Pores III: Formation, Properties, and Significance for Advanced Materials: Proceedings of the International Symposium,The Electrochemical Society*, 2000 (**2006**) 434-446.

[54] S.K. Kairy, S. Turk, N. Birbilis, A. Shekhter, The role of microstructure and microchemistry on intergranular corrosion of aluminium alloy AA7085-T7452, *Corrosion Science,* (**2018**).

[55] A.K. Gupta, D.J. Lloyd, Precipitation hardening in Al–Mg–Si alloys with and without excess Si, *Materials Science and Engineering: A,* 316 (**2001**) 11-17.

[56] J.L. Murray, The Al−Mg (aluminum−magnesium) system, *Journal of Phase Equilibria,* 3 (**1982**) 60.

[57] A. Mostafa, M. Medraj, Binary phase diagrams and thermodynamic properties of silicon and essential doping elements (Al, As, B, Bi, Ga, In, N, P, Sb and Tl), *Materials (Basel),* 10 (**2017**) 676.

[58] R. Dorward, C. Bouvier, A rationalization of factors affecting strength, ductility and toughness of AA6061-type Al–Mg–Si–(Cu) alloys, *Materials Science and Engineering: A,* 254 (**1998**) 33-44.

[59] A. Shi, B.A. Shaw, E. Sikora, The role of grain boundary regions in the localized corrosion of a copper-free 6111-like aluminum alloy, *Corrosion Science,* 61 (**2005**) 534-547.

[60] E.A.G. Liddiard, J.A. Whittaker, Atmospheric corrosion behaviour of two structural aluminium alloys (H10 and H15), *Journal of the Institute of Metals,* 89 (**1960**).

[61] I.L. Muller, J.R. Galvele, Pitting potential of high purity binary aluminium alloys Al-Cu alloys. pitting and intergranular corrosion, *Corrosion Science,* 17 (**1977**) 179-193.

[62] K. Nisancioglu, Ø. Strandmyr, Corrosion of AlMgSi alloys with Cu additions: the effect of Cu content up to 0.9 weight percent, Report no, *STF34 A78052, SINTEF,* Trondheim, Norway (**1978**).

[63] H. Hug, Ueber den einfluss geringer schwermetallgehalte auf die korrosionsbestandigkeit von AlMgSi legierungen, *Aluminium,* 23 (**1941**) 33.

[64] W.J. Liang, P.A. Rometsch, L.F. Cao, N. Birbilis, General aspects related to the corrosion of 6xxx series aluminium alloys: Exploring the influence of Mg/Si ratio and Cu, *Corrosion Science,* 76 (**2013**) 119-128.

[65] S.K. Kairy, P.A. Rometsch, C.H.J. Davies, N. Birbilis, On the intergranular corrosion and hardness evolution of 6xxx series Al alloys as a function of Si:Mg ratio, Cu content, and aging condition, *Corrosion Science,* 73 (**2017**) 1280-1295.

[66] Y. Tamura, T. Haitani, N. Kono, Liquid solubility of manganese and its influence on grain size of Mg-Al alloys, *Materials Transactions,* 47 (**2006**) 1968-1974.

[67] M. Zamin, The role of Mn in the corrosion behavior of Al-Mn alloys, *Corrosion Science,* 37 (**1981**) 627-632.

[68] R. Ambat, A.J. Davenport, G.M. Scamans, A. Afseth, Effect of iron-containing intermetallic particles on the corrosion behaviour of aluminium, *Corrosion Science,* 48 (**2006**) 3455-3471.

[69] A.P. Bond, G.F. Bolling, H.A. Domian, H. Biloni, Microsegregation and the tendency for pitting corrosion in high-purity aluminum, *Journal of The Electrochemical Society,* 113 (**1966**) 773-778.

[70] H. Tanihata, T. Sugawara, K. Matsuda, S. Ikeno, Effect of casting and homogenizing treatment conditions on the formation of Al–Fe–Si intermetallic compounds in 6063 Al–Mg–Si alloys, *Journal of Materials Science,* 34 (**1999**) 1205-1210.

[71] X. Zhou, C. Luo, T. Hashimoto, A.E. Hughes, G.E. Thompson, Study of localized corrosion in AA2024 aluminium alloy using electron tomography, *Corrosion Science,* 58 (**2012**) 299-306.

[72] R.G. Buchheit, L.P. Montes, M.A. Martinez, J. Michael, P.F. Hlava, The electrochemical characteristics of bulk-synthesized Al2CuMg, *Journal of the Electrochemical Society,* 146 (**1999**) 4424-4428.

[73] A.K. Bhattamishra, K. Lal, Influence of ageing on corrosion behaviour of Al-Mg-Si alloys in chloride and acid media, *Zeitschrift fur Metallkunde,* 89 (**1998**) 793-796.

[74] H.P. Godard, The corrosion of light metals, *John Wiley & Sons Inc*, New York, USA (**1967**).

[75] D.O. Sprowls, R.H. Brown, Stress corrosion mechanisms for alumnium alloys, *Proceedings of fundamental aspects of stress corrosion cracking,* The Ohio State University, OH, USA (**1969**) 466-506.

[76] A.K. Bhattamishra, K. Lal, Microstructural studies on the effect of Si and Cr on the intergranular corrosion in Al-Mg-Si alloys, *Materials & Design,* 18 (**1997**) 25-28.

[77] V. Guillaumin, G. Mankowski, Influence of overaging treatment on localized corrosion of Al 6056, *Corrosion Science,* 56 (**2000**) 12-23.

[78] T.D. Burleigh, Aluminium alloys, their physical and mechanical properties, *ICAA-3,* 2 (**1992**) 435.

[79] T.D. Burleigh, E. Ludwiczak, R.A. Petri, Intergranular corrosion of an aluminum-magnesium-silicon-copper alloy, *Corrosion Science,* 51 (**1995**) 50-55.

[80] R. Dif, D. Bechet, T. Warner, H. Ribes, 6056 T78: a corrosion resistant copper-rich 6XXX alloy for aerospace applications, *Proceedings of the 6th International Conference on Aluminium Alloys (ICAA6), Japan Institute of Light Metals,* Tokyo (**1998**) 1991-1996.

[81] R. Dif, B. Bès, J.-C. Ehrström, C. Sigli, H. Mayet, P. Lassince, H. Ribes, Understanding and modelling the mechanical and corrosion properties of 6056 for aerospace applications, *Materials Science Forum* 331-337 (**2000**) 1613-1618.

[82] E.A.G. Liddiard, J.A. Whittaker, H.K. Farmery, The exfoliation corrosion of aluminium alloys, *Journal of the Institute of Metals,* 89 (**1961**) 377-384.

[83] W. Huppatz, Natural sea water corrosion testing of aluminum materials: corrosion behavior of extruded Al-Mg-Si and Al-Zn-Mg materials, *Werkst. Korros.,* 36 (**1985**) 35-36.

[84] G.J. Metcalfe, Atmospheric corrosion and stress-corrosion of aluminium copper magnesium and aluminium magnesium silicon alloys in the fully heat-treated condition, *Journal of the Institute of Metals,* 81 (**1953**) 269.

[85] Determination of resistance to IGC of solution heat-treatable aluminium alloys, Standard, BS 11846, *British Standards Institution,* (**1995**).

[86] V.G. Davydov, V.S. Siniavski, L.B. Ber, K.H. Rendigs, G. Tempus, V.D. Valkov, V.D. Kalinin, Y.V. Titkova, O.G. Ukolova, Y.A. Lukina, Influence of SSTT, ageing regime and stretching on IGC, complex of properties and precipitation behavior of 6013 alloy, *Materials Science Forum* 331-337 (**2000**) 1315-1320.

[87] A. G110, Standard practice for evaluating intergranular corrosion resistance of heat treatable aluminum alloys by immersion in sodium chloride + hydrogen peroxide solution, (**2015**).

[88] Y.Y. Zheng, B.H. Luo, Z.H. Bai, J. Wang, Y. Yin, Study of the precipitation hardening behaviour and intergranular corrosion of Al-Mg-Si Alloys with differing Si contents, *Metals,* 7 (**2017**) 387.

[89] S. Pournazari, D.M. Maijer, E. Asselin, FIB/SEM study of pitting and intergranular corrosion in an Al-Cu alloy, *Corrosion Science,* 73 (**2017**) 927-941.

Chapter 3 Initiation of Intergranular Corrosion

Abstract

Initiation of intergranular corrosion (IGC) was investigated on extruded aluminium alloy AA6005-T5 with small Cu content. The purpose of this work is to understand the effect of modifying the extruded surface by metallographic polishing, argon sputtering, and alkaline etching before exposing to acidified chloride solution according to the standard BS ISO 11846. Initiation of IGC was delayed on the as-received surface compared to the modified surface. Transmission electron microscope (TEM) analysis revealed this was due to the presence of an approximately 8 nm thick crystalline oxide layer formed during extrusion. IGC initiated at the primary α-Al(Fe,Cu,Mn)Si particles for all types of surfaces. However, these particles corroded rapidly in the test solution forming a residue of Cu and Si on the exposed particle surface, which acts as increasingly effective external cathodes for IGC. Enrichment of Cu on the Al matrix alloy surface by dealloying, shown by Glow Discharge Optical Emission Spectroscopy (GD-OES) depth profiling, also contributes increasingly to the formation of an effective external cathode for IGC. The AlMgSiCu (Q-phase) particles, present as primary and secondary particles, were relatively stable in the test solution both against anodic oxidation and as cathodic sites.

3.1 Introduction

Al-Mg-Si (6xxx series) alloys are generally considered to have good corrosion resistance [1]. However, unfavourable thermomechanical treatment [2, 3] and alloying have proven to increase the IGC susceptibility, e.g., presence of Cu [4] and/or Si in excess of the stoichiometric ratio Mg/Si = 1.73 for the hardening phase Mg_2Si [5, 6]. A comprehensive study in the last decade of IGC susceptibility of alloy 6xxx series extrusions, containing nominally 0.6 wt.% Mg, 0.6 wt.% Si and 0.2 wt.% Cu, indicated significant IGC if the profiles were air cooled after extrusion [7-10]. A variant of the alloy with 0.02 wt.% Cu content was resistant to IGC. However, the IGC susceptibility was reduced and finally eliminated by artificial ageing, although overageing introduced pitting susceptibility [8]. Svenningsen et al. showed that IGC susceptibility was correlated with segregation of nearly continuous Cu film of a few nm thick along the grain boundaries in the underaged condition [9]. This result has recently been confirmed by Kairy et al. [11]. Furthermore, the intermetallic particles α-Al(Fe,Mn)Si and AlMgSiCu (Q-phase), which are commonly present in the alloy, were considered important as external cathodes at the initiation phase [12] , losing their significance in relation to the Cu film along the susceptible grain boundaries (internal cathodes) as IGC propagated into the metal.

More recently, the role of α-phase particles as cathodes was suggested to be limited during accelerated IGC testing according to the standard BS ISO 11846, since they corroded rapidly in the acidified chloride test solution [13]. The Q-phase particles were relatively resistant to the test solution, attributed to their high nobility in relation to the other elements in the alloy and existing intermetallic particles [13]. The mechanisms behind the initiation and propagation of IGC in 6xxx alloys containing of the order 0.1 wt.% Cu is still not fully understood.

The purpose of this work is to provide additional information about the effect of surface microstructure and chemistry on IGC initiation on alloy AA6005. The test solution was restricted to the acidified chloride solution used in the BS ISO 11846 standard, which is frequently used for ranking of commercial alloys in research and practice, with claims about the good qualitative correspondence between the accelerated test results and atmospheric field exposure [10].

3.2 Experimental

3.2.1 Materials

The test materials were provided by Hydro AS as extruded profiles with the following thermomechanical processing: Billets were homogenized by heating from room temperature to 585 °C in 6.5 h and held at that temperature for 2.5 h. The billets were then air cooled and extruded. Subsequent ageing was performed for 5 h at 185 °C, followed by cooling in the air for obtaining the T5 condition. This condition will be referred to as the as-received condition. The chemical composition of the alloy, determined by spark optical emission spectroscopy, is given in Table 3.1.

Table 3.1 Composition of 6005-T5 alloys (wt.%).

	Al	Si	Fe	Cu	Mn	Mg
6005-T5	Balance	0.64	0.21	0.14	0.16	0.57

Samples were examined in the as-received condition and, also, after the application of various pretreatments, such as metallographic polishing, alkaline etching and Ar-sputtering. Polished samples were prepared by grinding with SiC papers and then metallographic polishing through

1 µm diamond paste. Alkaline etching was performed by immersion in 7.5 wt.% NaOH solution for 3 min at 55-60 °C followed by 2 min desmutting in concentrated HNO_3. Ar-sputtered samples were prepared in a Horiba Jobin-Yvon GD-OES instrument [13]. Samples were sputtered in an argon atmosphere of 600 Pa and 32 W power with an anode diameter of 4 mm.

The amount of metal removed by these pre-treatments from the surface is shown in Table 3.2. These treatments were selected as control (polishing), common pretreatment before corrosion test (alkaline etching), and a fast and convenient cleaning method used in earlier work (Ar-sputtering) for comparison [13].

Table 3.2 Thickness removed by pretreatment before corrosion testing in acidified chloride solution.

Pretreatment	Thickness removed (µm)
Polished	10-15
Alkaline-etched	10-15
Ar-sputtered	1-2

3.2.2 Corrosion testing

Samples of dimension 20 × 20 mm were used in corrosion testing. Accelerated corrosion testing was based on the standard BS ISO 11846 method B. The standard test requires that the samples are the first alkaline etched for 1-3 min in a solution consisting of 7.5 wt.% NaOH at 55-60 °C and then desmutted in concentrated HNO_3 acid. Samples are subsequently immersed for 24 h in acidified chloride solution (test solution) at room temperature (~ 22 °C) consisting of 30 g NaCl and 10 ml concentrated HCl per litre at pH 0.95. The corrosion products are then removed by dipping in concentrated HNO_3 acid. In the present work, the samples modified according to one of the methods as specified in Table 3.2 and explained in the previous section were subsequently exposed to the test solution for 10 min. The as-received samples were immersed for 60 min. These modifications in the pretreatment and corrosion test were introduced in order to understand the effect of initial surface condition on IGC initiation, in particular, the induction time, location and morphology.

3.2.3 Surface characterization

The morphology of IGC initiation sites was investigated by use of a Zeiss Ultra field emission gun scanning electron microscope (FE-SEM). Identification and response of the intermetallic particles and matrix to etching and corrosion was done semi-quantitatively by using energy dispersive X-ray spectroscopy (EDS) at an accelerating voltage of 5 kV. The grain boundary chemistry and surface oxide layer was otherwise investigated by a Jeol JEM 2100F microscope while the high-resolution TEM image in Fig. 3.9 is from Jeol JEM ARM200F double corrected cold FEG microscope TEM, operated at 200 kV. The TEM foils were prepared from the surface, the sample was ground very lightly on the surface to make it flat and then from the back to make thin foils for electropolishing. The electropolished samples were ion milled gently to remove the surface layer that had been exposed to the electrolyte. Cross-sectional TEM samples for analysis of the grain boundaries and metal-oxide interfaces were prepared by the focused ion beam (FIB) lift out technique [14]. Details of the technique are given in appendix A.

The oxide layer was analyzed by using the precession -assisted crystal orientation mapping technique (PACOM) on cross-sectional foils prepared for the near-surface region of the as-received sample. This is a TEM based technique, in which the diffraction pattern is acquired for a grid of points by scanning a focused probe over the area of interest. Automated indexing of the diffraction patterns allows determination of crystal structure and orientation of grains down to nanometers in size [15].

3.2.4 Electrochemical characterization

The electrochemical tests were performed using a DC 105 Gamry potentiostat. A conventional three electrode electrochemical cell was used. 1 cm^2 area of the working electrode (sample) was exposed to the test solution by masking the rest of the sample area with beeswax. A saturated calomel electrode (SCE) was used as the reference, and a platinum electrode was used as the counter electrode. Open circuit potential (OCP) was measured for 200 s prior to a potentiodynamic run. Cathodic polarization tests were performed at a scan rate of 0.5 mV/s starting from the OCP at 25 °C . At least three replicate measurements were made for each type of sample.

3.3 Results

3.3.1 As-received and pretreated samples

Surface morphology

Morphology of the as-received surface, dominated by extrusion lines, is shown as secondary and back-scattered electron images in Fig. 3.1a and 3.1b, respectively. The matrix alloy appears to be partially smeared over the intermetallic particles (Fig. 3.1a) during extrusion, which becomes more distinctly visible in the backscattered electron image (Fig. 3.1b).

The pretreated surface morphologies obtained before the corrosion test are shown as secondary-electron images in Fig. 3.2. Metallographic polishing makes the intermetallic particles visible as randomly distributed bright features at the surface (Fig. 3.2). Ar-sputtering (Fig. 3.2b) and alkaline etching (Fig. 3.2c) reveal both the grain boundaries and intermetallic phases. The grain size is seen to be in the range 10-80 µm.

Semi-quantitative EDS spot analyses of the particles on polished and alkaline-etched samples are shown in Fig. 3.3a and 3.3b, respectively. These results, indicate that the particles are α-Al(Mn,Fe,Cu)Si phases. Cu is enriched in the classical α-Al(Mn,Fe)Si composition [16]. These spot analyses, combined with qualitative elemental EDS maps of an α-phase on an alkaline-etched surface in Fig. 3.4, indicate that the nobler components of the phase were enriched due to selective corrosion of the active Al component during alkaline etching (Fig. 3.3b and 3.4), as compared to the α-phase on the polished surface (Fig. 3.3a).

The α-particles are irregularly shaped and have a size range between 0.1-5 µm, based on the quantification of the distribution shown in Fig. 3.5. The analysis was performed by use of image J software based on 16 SEM backscattered electron images, acquired from replicate polished samples.

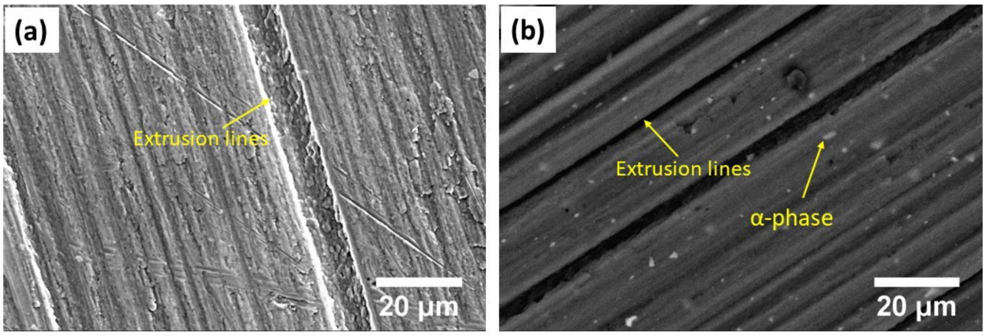

Fig. 3.1 (a) Secondary and (b) back-scattered electron images of the as-received surface obtained at accelerating voltages of 10 kV and 25 kV, respectively.

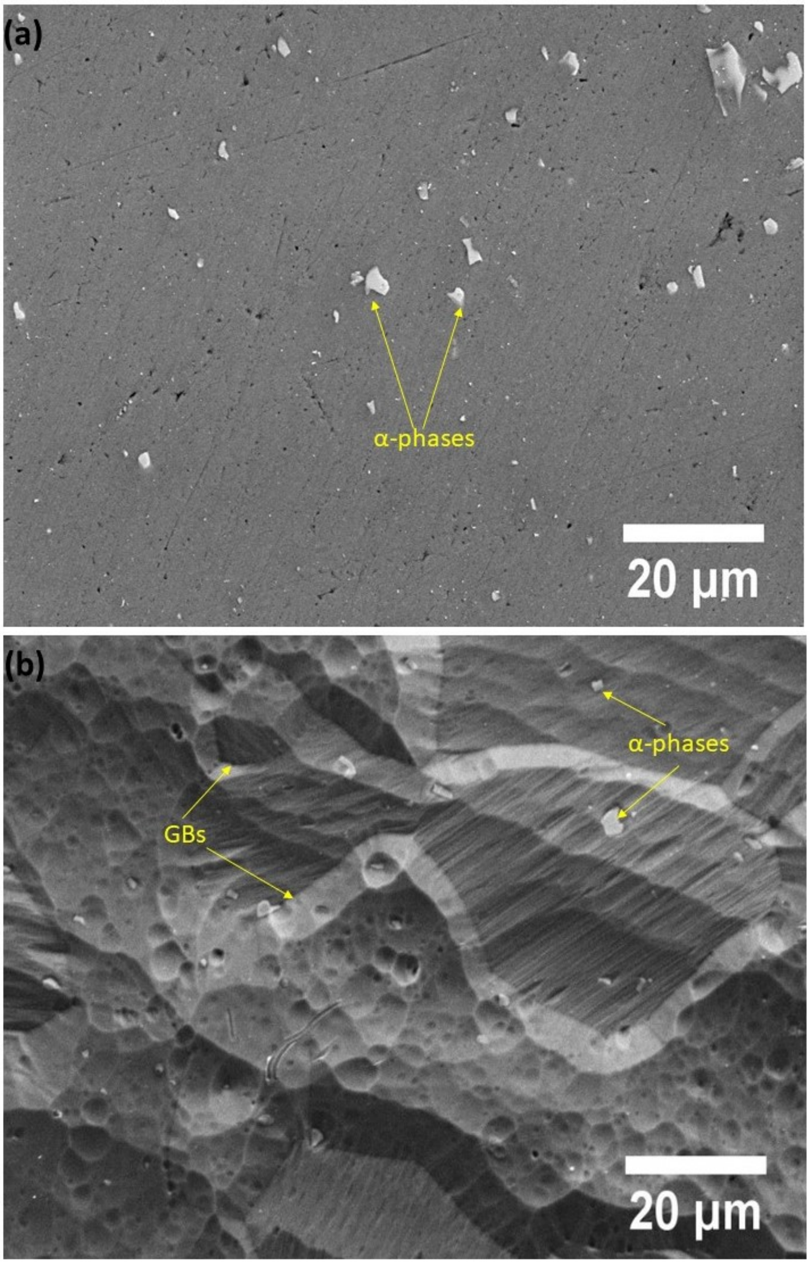
(a)
α-phases
20 μm
(b)
α-phases
GBs
20 μm

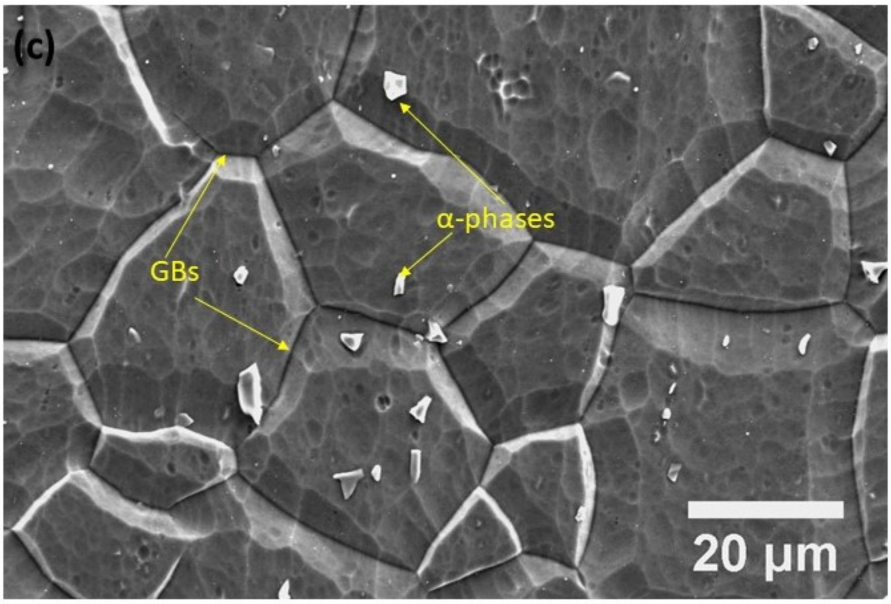

Fig. 3.2 Secondary electron images of (a) mechanically polished, (b) Ar-sputtered and (c) alkaline etched surfaces.

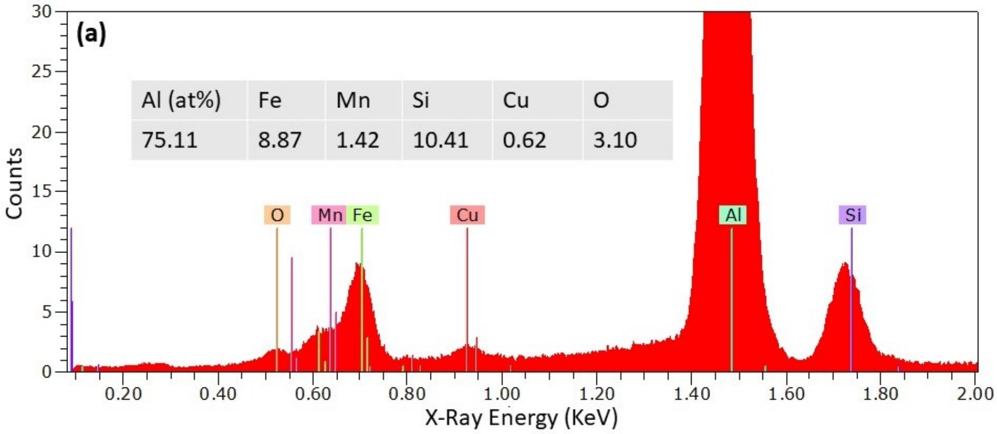

Al (at%)	Fe	Mn	Si	Cu	O
75.11	8.87	1.42	10.41	0.62	3.10

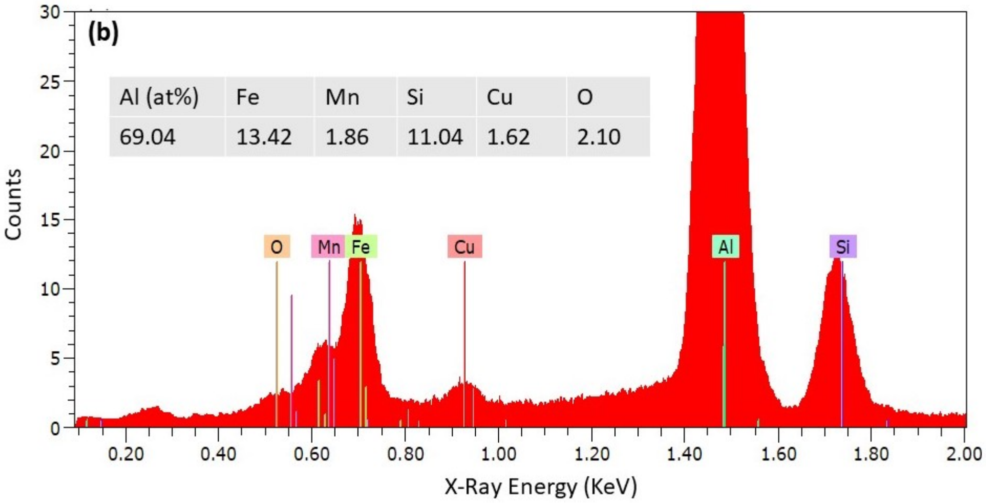

Al (at%)	Fe	Mn	Si	Cu	O
69.04	13.42	1.86	11.04	1.62	2.10

Fig. 3.3 EDS elemental analysis of α-phases on (a) polished and (b) alkaline etched surfaces.

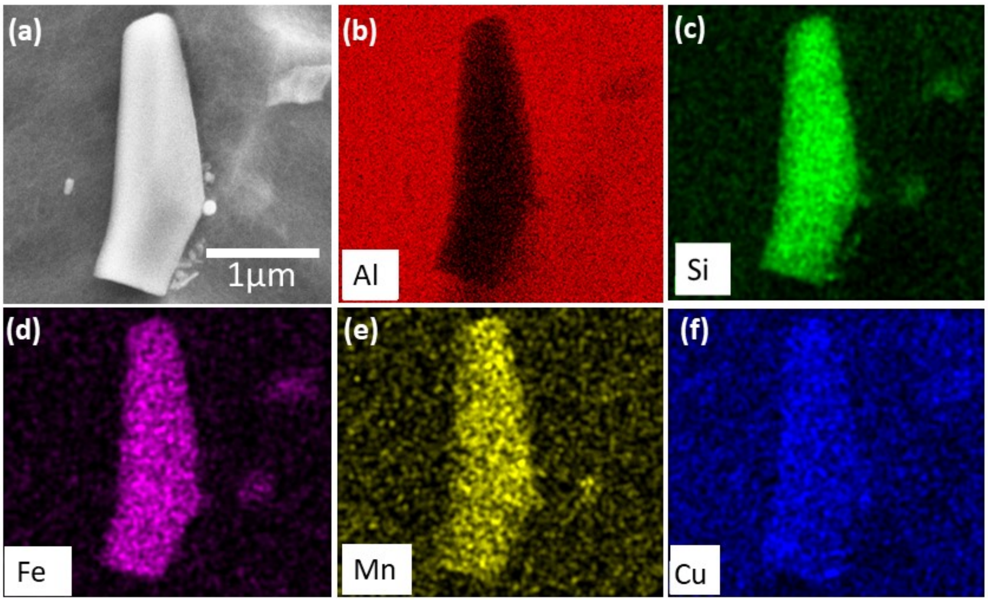

Fig. 3.4 (a) SEM-image of α-Al (Fe,Mn,Cu)Si phase on the alkaline etched surface. EDS maps of the α-phase for (b) Al, (c) Si, (d) Fe, (e) Mn, and (f) Cu.

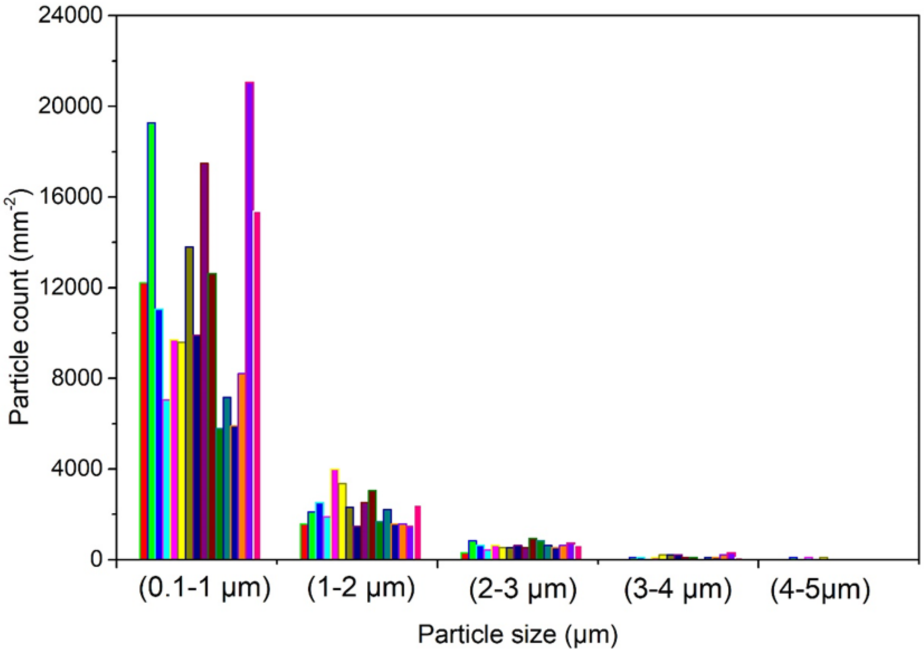

Fig. 3.5 Size distribution of α-phases on the polished AA6005 alloy.

Fig. 3.6 shows the alkaline etched surface at higher magnification (Fig. 3.2c) revealing the well-known scalloped morphology [17]. Quantitative point analysis of the grain-boundary phase is shown in Fig. 3.7. The STEM-EDS elemental map of a similar area on an uncorroded foil (Fig. 3.8a) shows that the rod-shaped grain boundary particles are the AlMgSiCu-phase (Q-phase). Fig. 3.8b indicates depletion of aluminium in the Q-phase with respect to the matrix, while Fig. 3.8(c, d, e) show enrichment of Si, Mg and Cu, respectively, in the Q-phase. These phases, which have their sizes in the range 100-500 nm, also precipitate in the grains as one of the hardening phases and around the α-phase particles, as discussed in more detail elsewhere [13]. STEM-EDS mapping (Fig. 3.8e) confirms [9] further the presence of a nanoscale, continuous Cu-film along the grain boundaries between the Q-phase particles. The corresponding depletion of these elements adjacent to the grain boundary in these EDS maps and increased purity of the matrix Al indicates the presence of a precipitate free zone (PFZ). These results agree well with the recent literature about Cu segregation along the grain boundaries and simultaneous formation of PFZ on low Cu containing 6xxx series alloys [9, 11, 18].

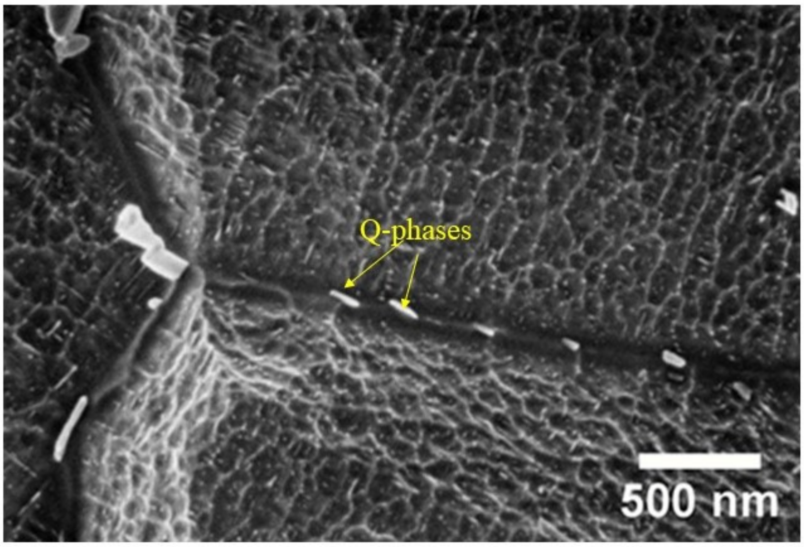

Fig. 3.6 Typical distribution of Q-phases on the alkaline etched surface. Densely distributed, much smaller particles are the hardening precipitates.

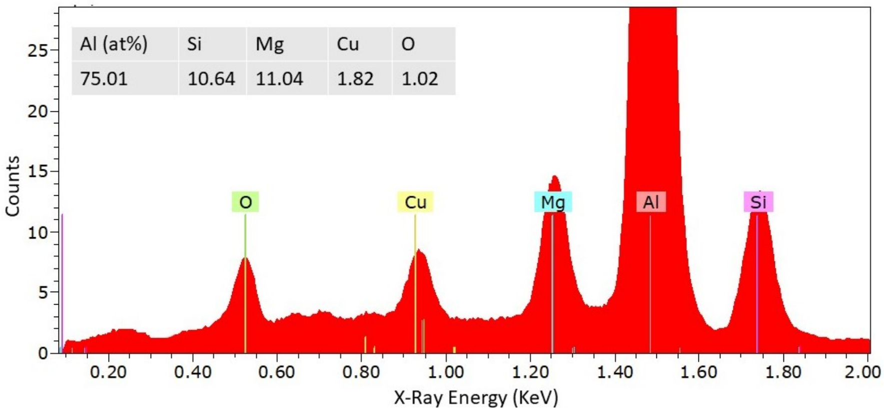

Al (at%)	Si	Mg	Cu	O
75.01	10.64	11.04	1.82	1.02

Fig. 3.7 SEM-EDS elemental analysis of a Q-phase particle on the alkaline etched surface.

.

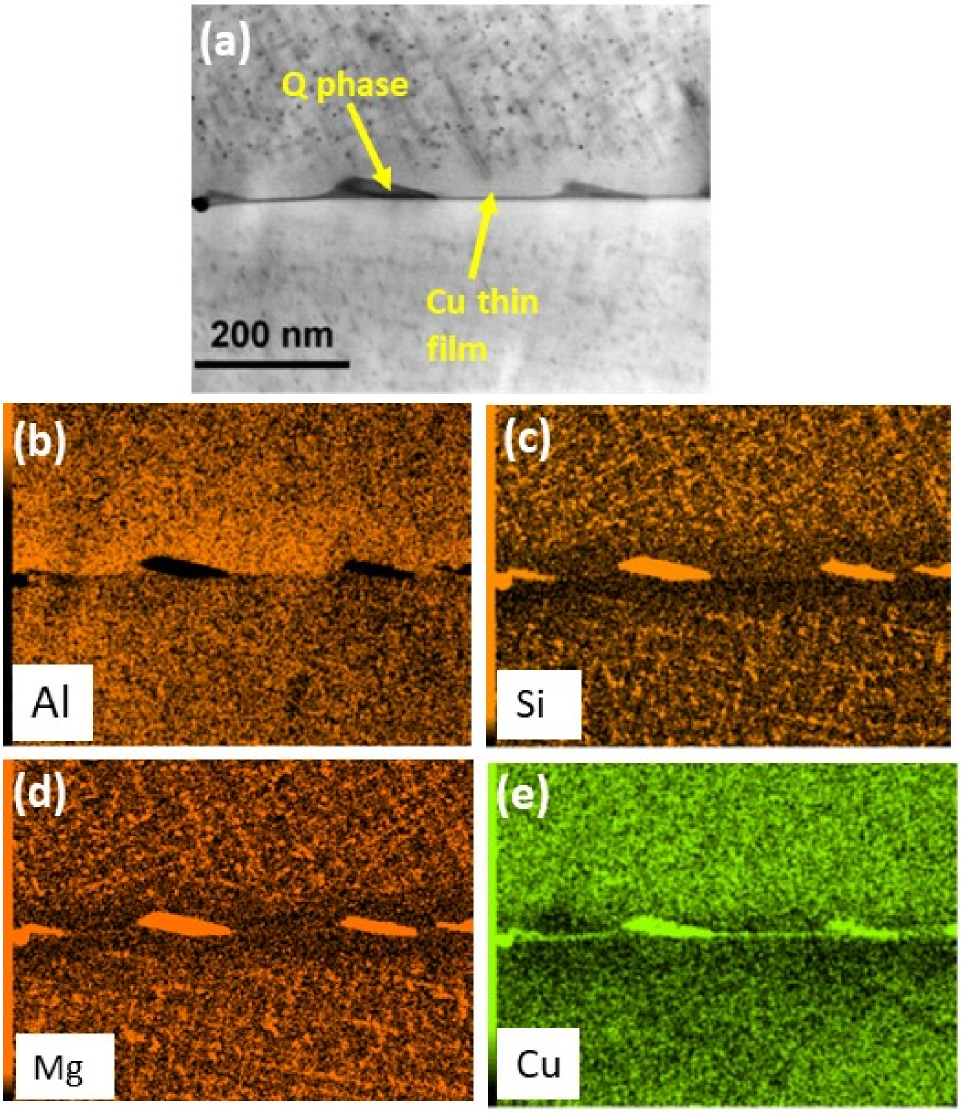

Fig. 3.8 STEM image showing (a) Q-phase particles decorating a grain boundary and Cu film joining the particles. EDS maps for (b) Al (c) Si (d) Mg (e) Cu for the grain boundary.

3.3.2 Oxide layer

The air-formed oxide on aluminium alloys is normally amorphous and a few nm thick [19]. Because of its relevance to corrosion initiation in the present work, the nature of the oxide on the as-received surface was of interest. No published literature could be found about the nature of the oxide on extruded Al surfaces. A cross-sectional study of the as-received, prepared by FIB and analysed by the PACOM technique, explained in the experimental section, was used for characterization of the oxide layer. TEM analysis, shown in Fig. 3.9a revealed that 8 nm thick crystalline oxide layer (Fig. 3.9b) was present on the extruded surface. Fig. 3.10a and b indicate that the crystallinity of the oxide layer is continuous along the surface. Fig. 3.10c is the diffraction pattern of Fig. 3.10b. Due to the similar structures and diffraction spacings obtained from γ-Al_2O_3 and spinel $MgAl_2O_4$, it was difficult to distinguish between the two phases as calculated diffraction patterns are very similar. STEM-EDS mapping of the oxide layer, as shown in Fig. 3.11, indicated, in addition to the expected Al (Fig. 3.11b) and O (Fig. 3.11c), enrichment of Mg (Fig. 3.11d) and Si (Fig. 3.11e). Therefore, the oxide layer was probably a mixture of the oxides γ-Al_2O_3, $MgAl_2O_4$ and SiO_2.

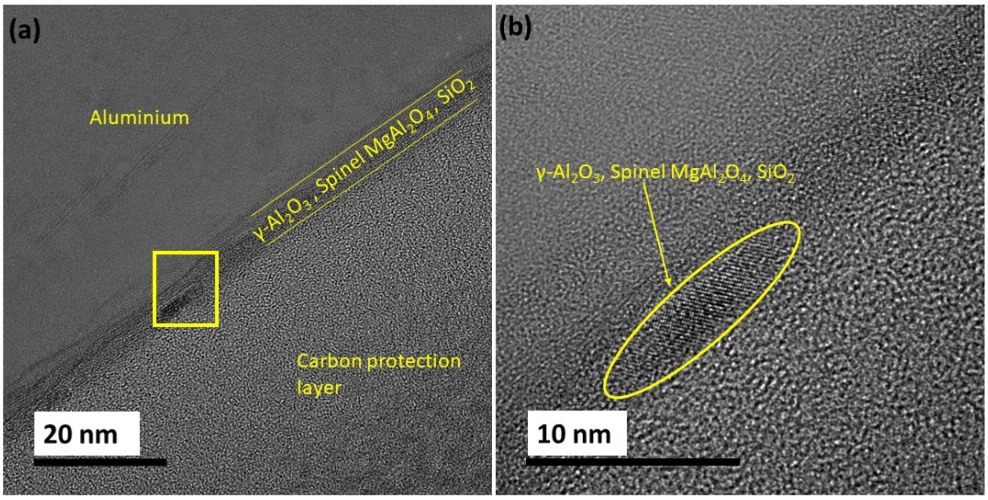

Fig. 3.9 (a) High-resolution TEM image of the cross-section of an oxide layer on the as-received surface. (b) The area marked with a yellow square in (a).

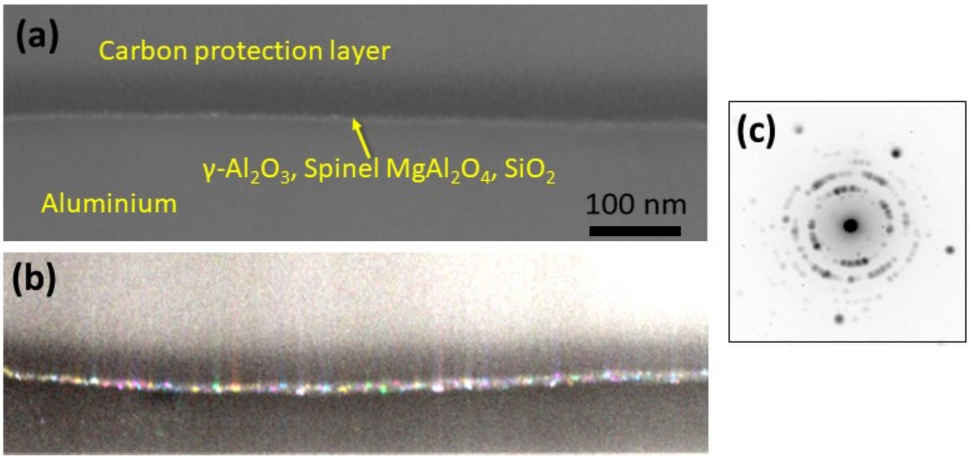

Fig. 3.10 (a) TEM image of the cross-section of the oxide layer. (b) The crystal orientation of the image of the oxide. (c) The diffraction pattern of oxide in (b).

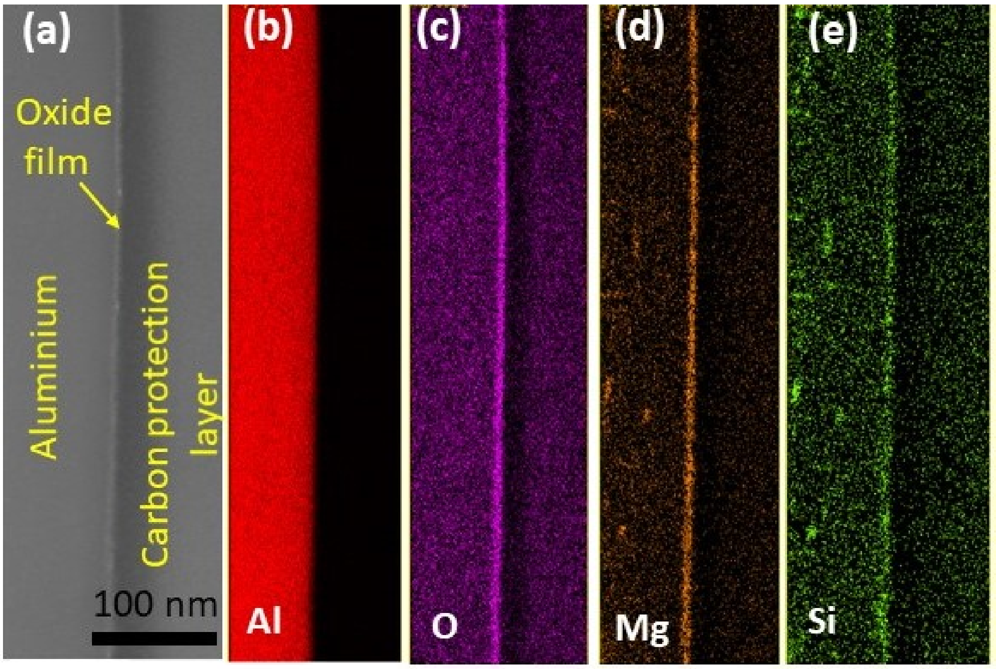

Fig. 3.11 (a) TEM image of the cross-section of the oxide layer. EDS maps for (b) Al, (c) O, (d) Mg, and (e) Si.

3.3.3 GD-OES analysis

The results in this section were reproducible for identical replicate samples within 10% experimental error. GD-OES depth profiling was performed on the as-received surface and the surfaces modified by pretreatment and corrosion, as shown in Fig. 3.12.

The profiles for Al and O are shown in Fig. 3.12a and b, respectively. These profiles shift towards the left in the order as-received, polished, alkaline etched and corroded, indicating a slightly decreasing thickness.

The profiles for Cu, as shown in Fig. 3.12c did not change significantly from the bulk value for the as-received and polished cases. They show a significant increase, by about an order of magnitude, with respect to the bulk value for the alkaline etched condition, starting from about 50 nm depth below the surface. This is attributed to the enrichment of Cu as a result of selective corrosion of the more active components in the alloy and the α-phase particles, especially Al. The Si profiles are seen (Fig. 3.12d) to become enriched for the as-received and alkaline-etched samples, also by about an order of magnitude with respect to the bulk concentration. Polished samples show a smaller, but still significant, enrichment by about a factor of 3. The Si enrichment occurred closer to the surface than that for Cu, starting at about 25 nm depth, i.e., about half that for Cu, indicating the possibility of enriching in the oxide layer, as suggested by the TEM results of the previous section for the as-received sample. The Mg profile for the as-received sample (Fig. 3.12e) was similar to that of Si both in terms of magnitude and thickness (about 10 nm) of the enrichment close to the sample surface. This result verifies the TEM analysis of the oxide above. The Mg profiles for the polished and alkaline etched surfaces did not show a significant change from the bulk value, possibly a slight depletion toward the surface. Mg oxide is expected to become enriched in the oxide as a result of alkaline etching. It probably dissolved during desmutting in nitric acid.

The GD-OES profiles for Fe and Mn, as shown in Fig. 3.12f and g, respectively, were somewhat similar to one another, but they were quite different from the profiles of the elements discussed above. The profiles for the two elements were quite constant at about their bulk concentrations towards the surface. They decreased closer toward the surface for as-received, and polished variants, while the profiles for the alkaline etched variants increased to maxima, at about 0.5 wt.% and 0.1 µm depth for Fe and 0.3 wt.% and 0.05 µm depth for Mn, before decreasing toward the surface. The results for the elements Fe and Mn were more scattered than those for Cu, Si and Mg, and the changes occurred within a larger thickness (largest of about 0.5 µm for the alkaline etched surface) from the surface, in relation to the concentrations of the other elements. These differences are related to the fact that Fe and Mn are largely incorporated in the α-phase particles, which are scattered in terms of size and position at the surface, while the others are segregated within a more uniform and thinner layer closer to the surface either in the oxide or solid solution matrix.

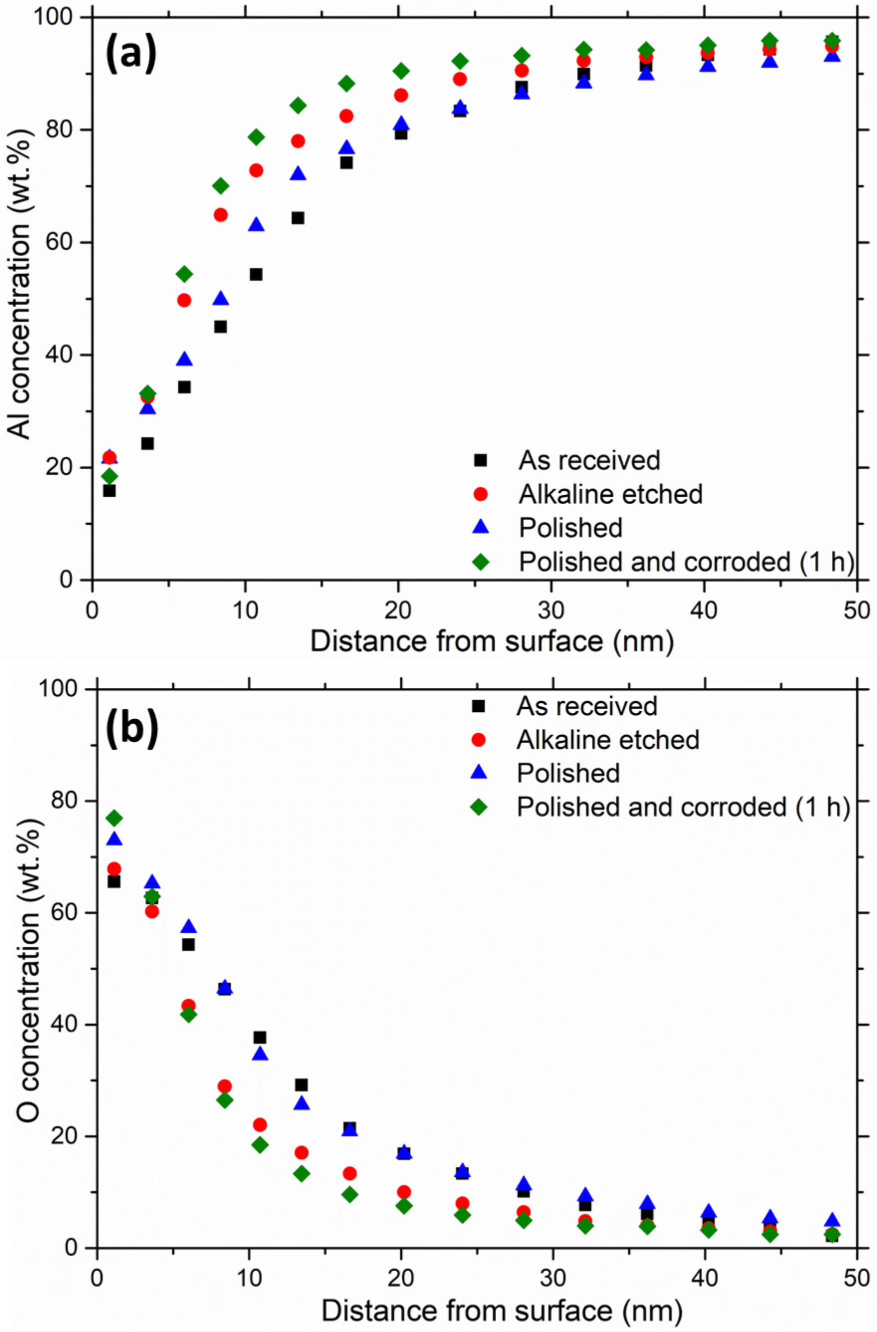
(a)
Al concentration (wt.%)
Distance from surface (nm)
0
20
40
60
80
100
0
10
20
30
40
50
As received
Alkaline etched
Polished
Polished and corroded (1 h)
(b)
O concentration (wt.%)
Distance from surface (nm)
0
20
40
60
80
100
0
10
20
30
40
50
As received
Alkaline etched
Polished
Polished and corroded (1 h)

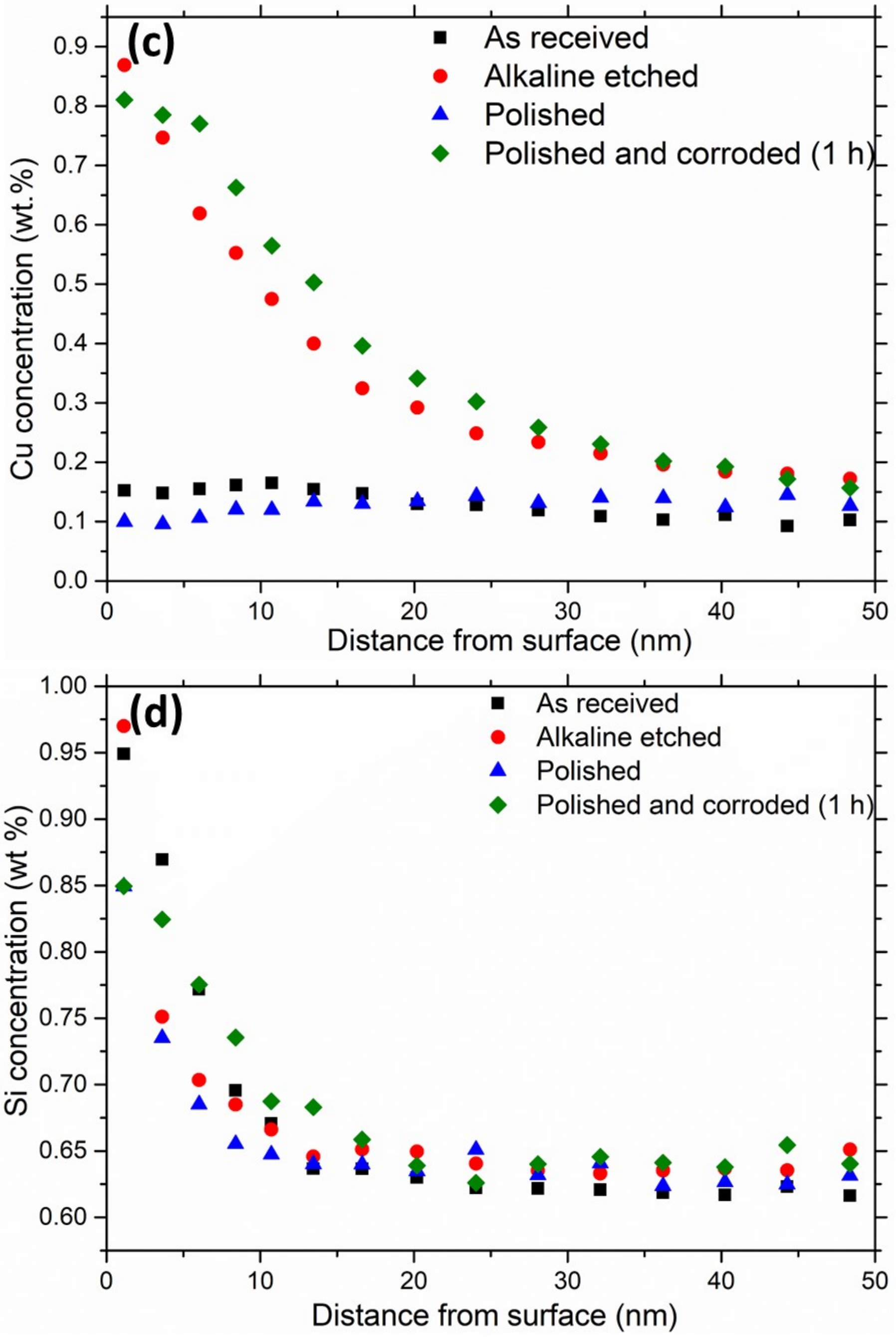
(c)
As received
Alkaline etched
Polished
Polished and corroded (1 h)
Cu concentration (wt.%)
0.0
0.1
0.2
0.3
0.4
0.5
0.6
0.7
0.8
0.9
0
10
20
30
40
50
Distance from surface (nm)
(d)
As received
Alkaline etched
Polished
Polished and corroded (1 h)
Si concentration (wt %)
0.60
0.65
0.70
0.75
0.80
0.85
0.90
0.95
1.00
0
10
20
30
40
50
Distance from surface (nm)

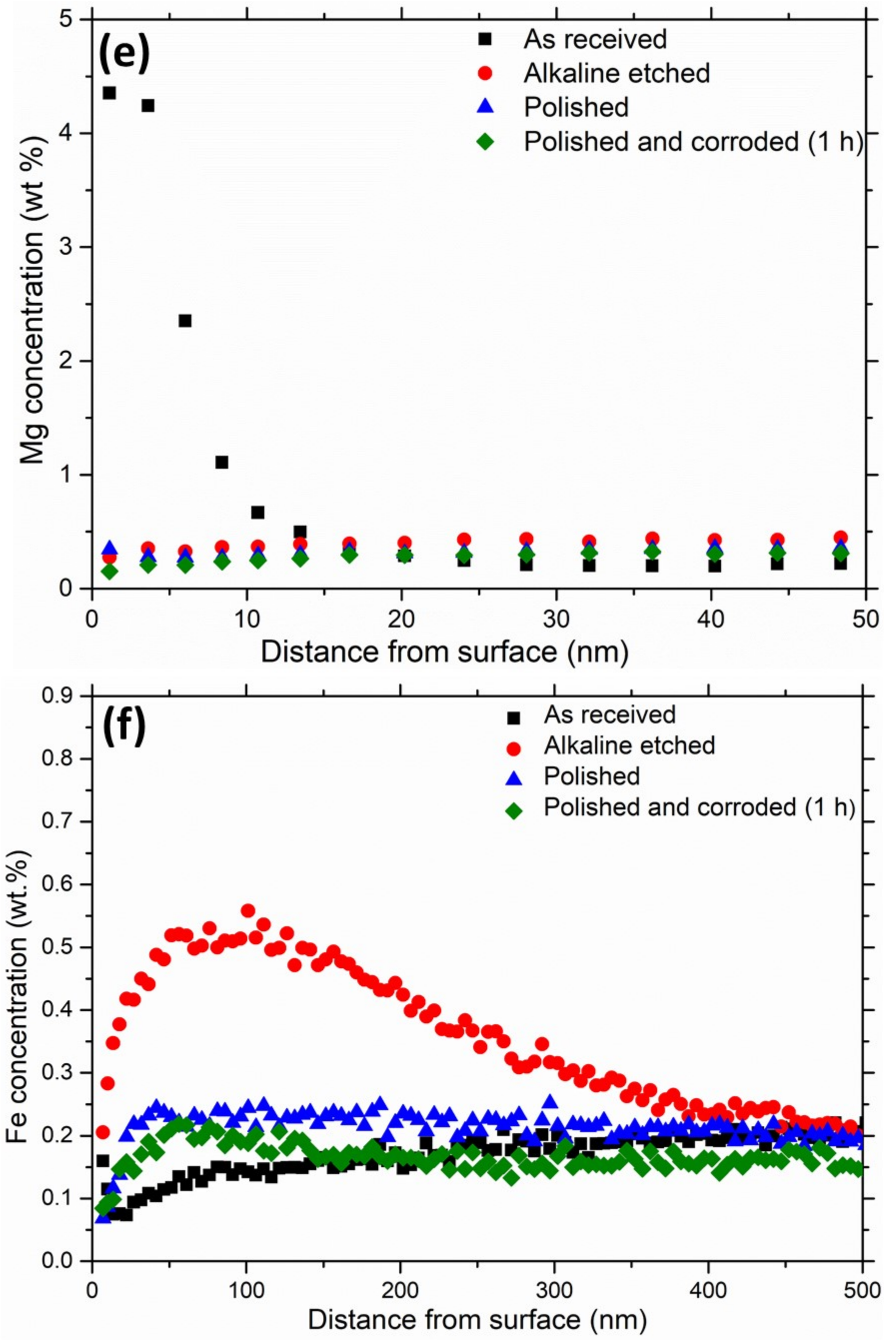
(e)
As received
Alkaline etched
Polished
Polished and corroded (1 h)
Mg concentration (wt %)
0
1
2
3
4
5
0
10
20
30
40
50
Distance from surface (nm)
(f)
As received
Alkaline etched
Polished
Polished and corroded (1 h)
Fe concentration (wt.%)
0.0
0.1
0.2
0.3
0.4
0.5
0.6
0.7
0.8
0.9
0
100
200
300
400
500
Distance from surface (nm)

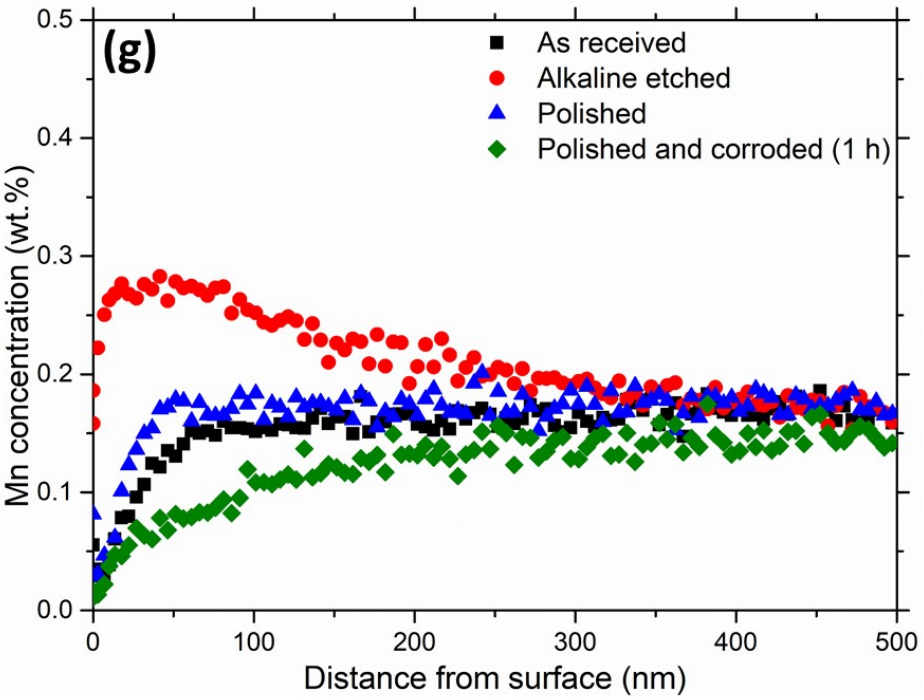

Fig. 3.12 GD-OES elemental depth profiles of (a) Al, (b) O, (c) Cu, (d) Si, (e) Mg, (f) Fe and (g) Mn for different pretreated surfaces

3.3.4 Cathodic polarization

Cathodic polarization curves for different pretreated surfaces indicate that the alkaline etched surface had the highest cathodic activity, followed by the corroded surface, as shown in Fig. 3.13. Increase in the cathodic activity by alkaline etching is attributed to the exposure of a larger number density of α-phases and their further enrichment with the nobler elements of Fe, Mn and Cu, as well as Cu enrichment of the solid-solution Al alloy surface, as discussed above in sections 3.3.1 and 3.3.3. The corroded sample had a higher cathodic activity than the polished surface, also attributable to the enrichment of Cu, as indicated by the GD-OES data in Fig. 3.12c. The polished surface appears to be slightly more cathodic than the as-received surface, possibly due to a larger area of exposed α-phase particles at the outset of the polarization run.

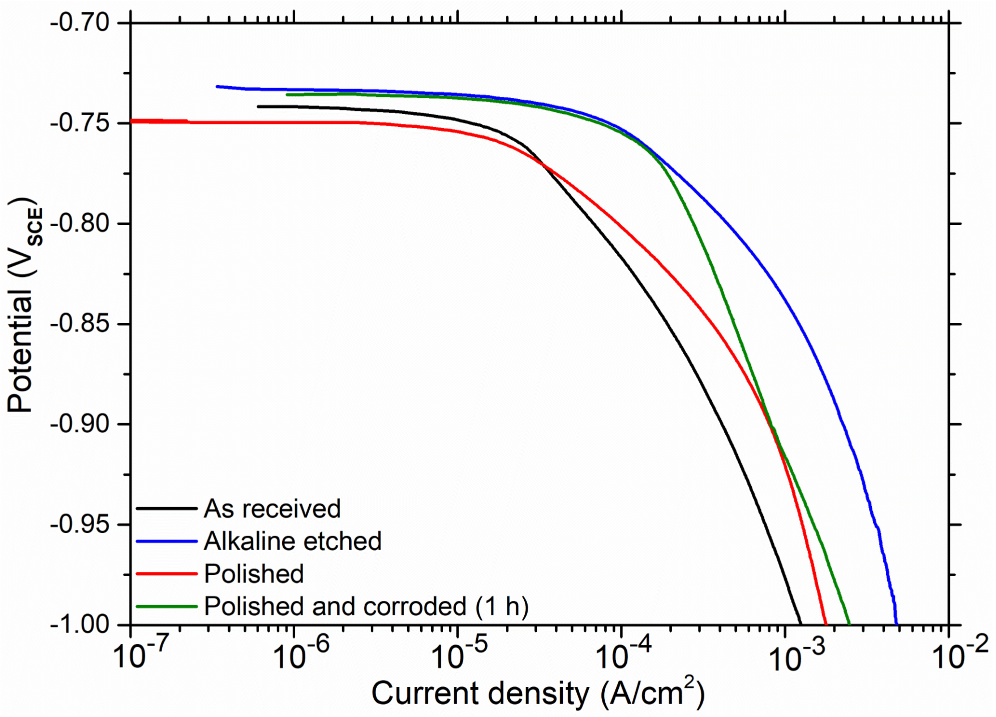

Fig. 3.13 Cathodic polarization curves for different pretreated surfaces of AA6005 in acidified chloride solution.

3.3.5 Corroded samples

Initiation morphology

In order to examine the initiation of intergranular corrosion on as-received and pretreated surfaces, immersion in acidified chloride solution was performed for different time periods. Fig. 3.14a shows typical IGC morphology on the as-received surface after 1 h of exposure. Observation of the marked area in Fig. 3.14a at a higher magnification in Fig. 3.14b suggests that IGC initiated locally at an α-phase particle. A similar conclusion can be drawn for IGC initiation on the pretreated surfaces, metallographically polished (Fig. 3.14c and d), alkaline etched (Fig. 3.14e and f) and Ar sputtered (Fig. 3.14g and h), verifying earlier introductory work [13]. However, IGC initiated faster on the pretreated surfaces than on the as-received surface, i.e., after about 10-15 min of immersion on pretreated surfaces, as opposed to about 1 h on the as-received surface. The area marked with red ellipse in Fig. 3.14e, which shows an unattacked α-phase particle on a grain boundary, indicates that not all α-phase particles on the grain boundary are necessarily initiation sites for IGC, as opposed to the case shown in Fig. 3.14h on the same surface.

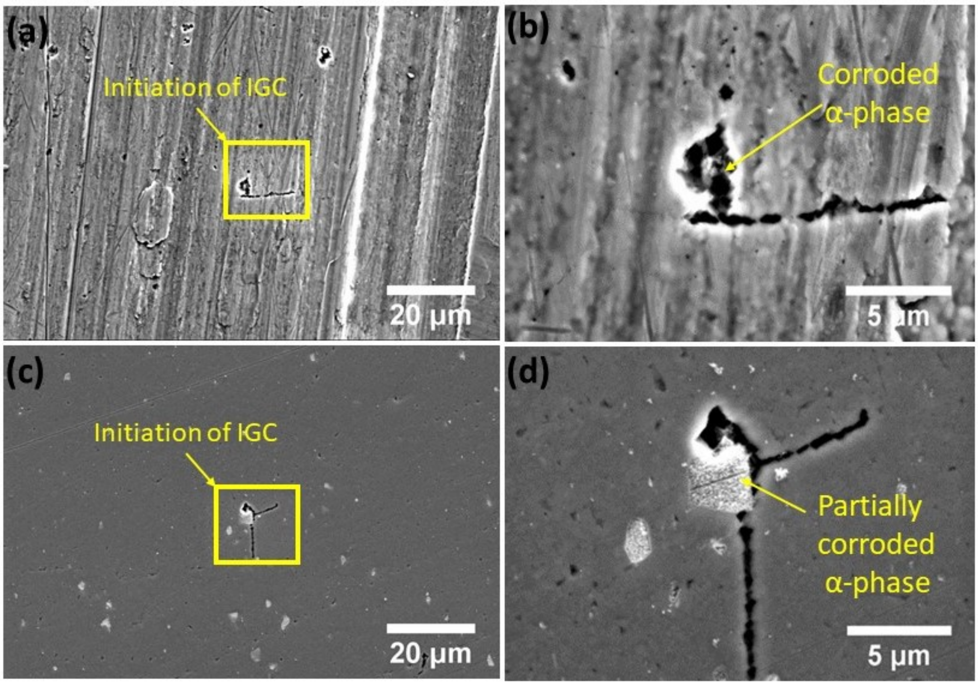

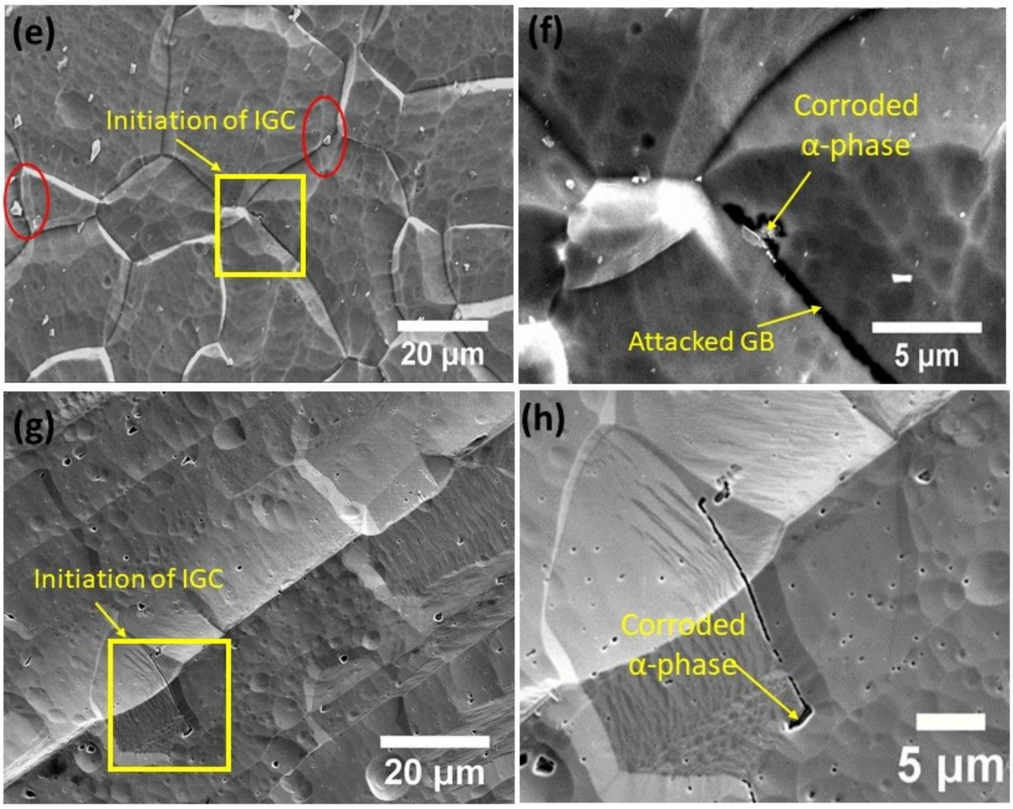

Fig. 3.14 Initiation of IGC on (a) as-received surface. (b) Area marked with a yellow square in (a) at higher magnification. (c) Initiation on the Ar-sputtered surface after. (d) Area marked with a yellow square in (c) at higher magnification. (e) Initiation on the mechanically polished surface. (f) Area marked with a yellow square in (e) at higher magnification (g) Initiation on the alkaline etched surface. (h) Area marked with a yellow square in (g) at higher magnification. Morphologies in (a) and (b) are after 1 h and the rest after 10 min exposure to the test solution.

Corrosion of intermetallic phases

The α-phase itself also corroded during immersion in acidified chloride solution, in agreement with the earlier study [13], as shown in Fig. 3.14f, h and Fig. 3.15a, leaving a residue of its noble components, as indicated by the EDS maps of the phase constituents in Fig. 3.15. The figure indicates that Cu was enriched significantly (Fig. 3.15c) in relation to its initial content (Fig. 3.4f), and some Si remained (Fig. 3.15d) at a smaller concentration in relation to the original (Fig. 3.4c), as a result of selective corrosion (dealloying) of its active components, Al

(Fig. 3.15b), Fe (Fig. 3.15e) and Mn (Fig. 3.15f). No detectable Fe and Mn remained in the α-phase particles after 15 min exposure to the acidified chloride solution.

Fig. 3.16 shows a closer study of different stages of corrosion on selected α-phase particles away from a grain boundary (not affected by IGC) and the surrounding matrix in the acidified chloride solution. Fig. 3.16a shows an uncorroded particle on a polished sample surface. Corrosion of the matrix around the particles at the outset formed a ditch as shown in Fig. 3.16b, indicating that the α-phase behaved as the cathode of the microgalvanic couple, as is well known from earlier studies [20] and as shown in additional micrographs also in appendix B (Fig. B4). However, the α-phase also started to corrode, as discussed above, leaving a porous dealloyed layer, as shown in Fig. 3.16c. Fig. 3.16d shows a later stage of dealloying of the particle and exposure of the Q-phase particles at the bottom of the pit.

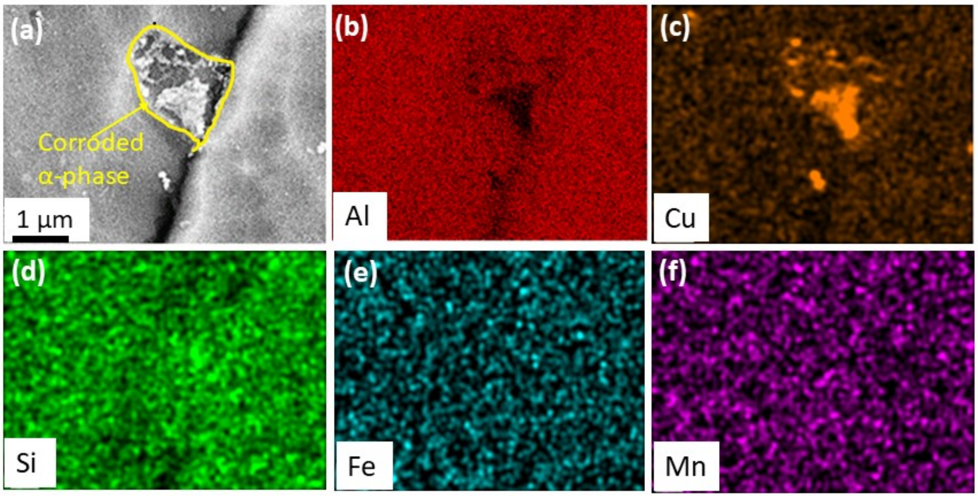

Fig. 3.15 (a) SEM image of α-phase on the alkaline etched surface after 15 min corrosion in the test solution. EDS maps for (b) Al, (c) Cu, (d) Si, (e) Fe and (f) Mn.

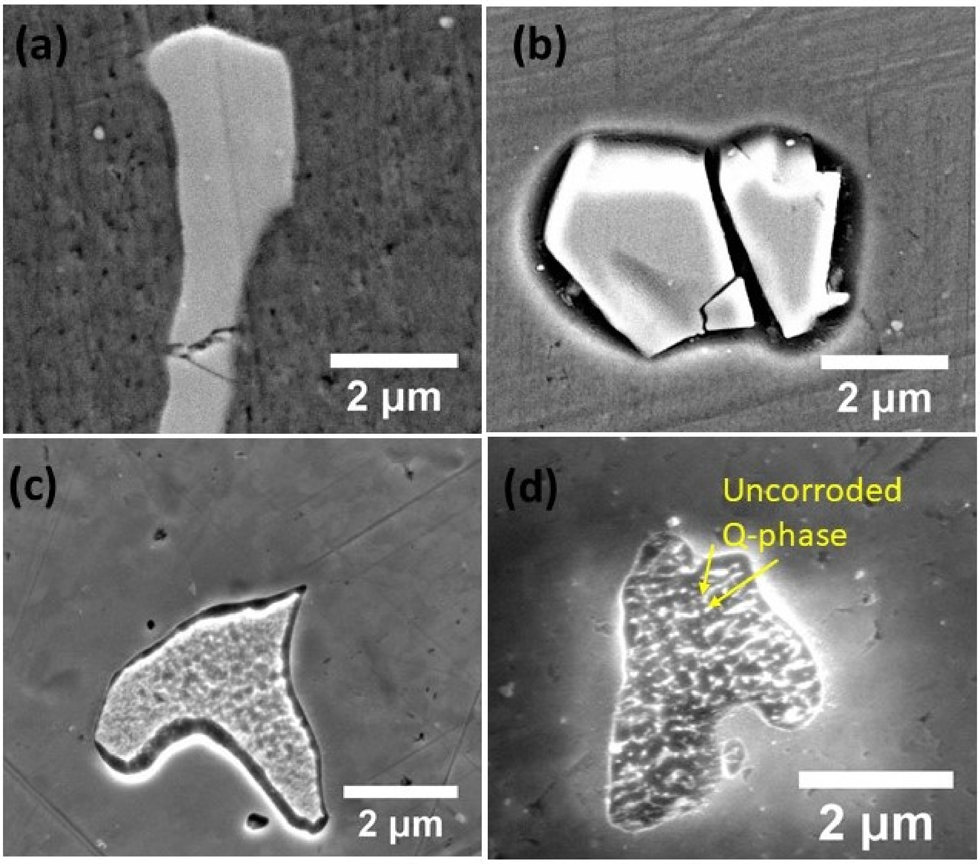

Fig. 3.16 Evolution of α-phase on the polished surface (a) before corrosion, (b) after 5 min immersion in test solution (active as cathode), (c) after 10 min corrosion resulting porous structure (indicating selective dissolution giving enrichment of Fe, Mn and Cu giving higher activity as cathode) and (d) its disappearance after 20 min of corrosion, exposing the Q-phase particles, decorating the interphase between the α-phase and the Al matrix.

The Q-phase was observed to be relatively inert in relation to the α-phase. Fig. 3.17c shows another example of uncorroded Q phase particles at the bottom of a pit formed by corrosion of an α-phase. Moreover, Q-phase acted as a physical barrier against IGC propagation, as shown in Fig. 3.17(b,c). This observation agrees well with the available literature [13, 18].

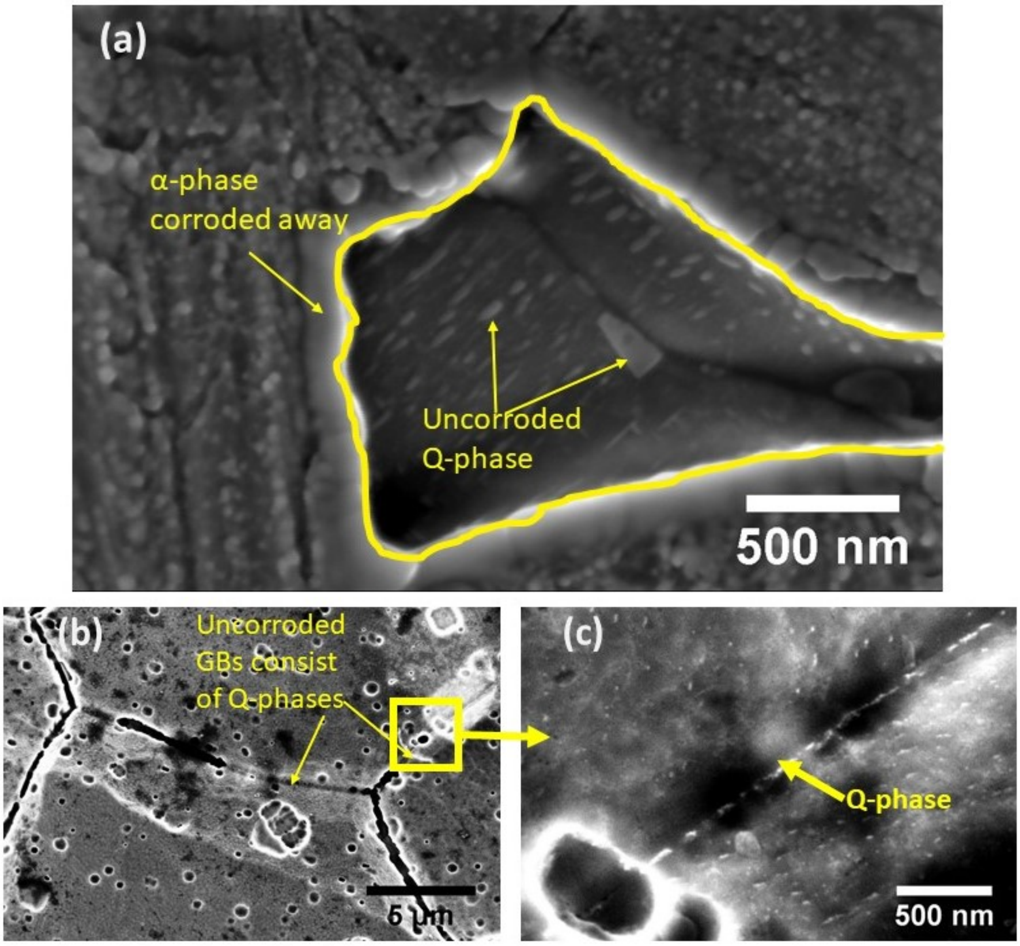

Fig. 3.17 (a) Uncorroded Q-phases at the bottom of the pit formed by corrosion of α-phase. (b) SEM image of a string of Q-phase particles along the grain boundary after 24 h corrosion in the test solution. (c) Area marked with yellow square in (b) at a higher magnification.

3.4 Discussion

The present work confirms earlier results [13] with new evidence that IGC initiates at the α-phase particles precipitated along the grain boundaries on alloy AA6005 in acidified chloride solution, and that the Q-phase is relatively inert. Moreover, the corrosion susceptibility of the α-phase itself to the acidified chloride solution is confirmed, showing in addition that all components of the phase, except Cu and Si, corrode selectively. The initiation morphology (and electrochemical data shown in appendix B for Cu-free synthetic α-phase) indicate further that the α-phase acts as a significant cathode in providing the cathodic current needed for self-corrosion, as well as the current needed for microgalvanic corrosion of the matrix around itself (Fig. 3.16b). The α-phase particles precipitated along the grain boundaries, provide both the initiation site, possibly in the form of a pit, and the cathodic current for the transformation of the attack into IGC when the adjacent grain boundary has the necessary conditions (Cu film as the internal cathode) to support such corrosion. The results demonstrate, moreover, that the α-phase particles, precipitated in the grains, also participate in the process. The remnants in the form of metallic Cu, as long as they remain attached to the surface, are also expected to continue to function as an effective external cathode. The α-phase particles are eventually removed by corrosion. However, fresh particles are exposed as a result of uniform etching of the surface in the acidified chloride solution, and the above process continues during propagation. At the same time, Cu is enriched more uniformly on the matrix as a fresh external cathode, as will be discussed further below. Therefore, the external cathodes appear to have an important role, at least, in the initiation of IGC for the present alloy - environment combination.

Different pretreatments such as metallographic polishing, alkaline etching and Ar-sputtering were selected to explore the difference in initiation of IGC due to change in surface morphology. The difference in the induction time for initiation between the pretreated surfaces, involving mechanical, chemical or physical material removal, was not significant. This is attributed to the presence of the crystalline oxide and smeared metal layer on the as-received sample after extrusion, both providing extra resistance against the initiation of localized corrosion. The smeared matrix layer also seems to cover the cathodic intermetallic phases [21]. All selected pretreatment methods remove both the crystalline oxide layer and smeared metal, leading to less protective air-formed oxide and exposure of the detrimental cathodic intermetallic particles at the surface.

Initiation of IGC was not observed at any other sites, such as the Q-phase, besides the α-phase. However, the results showed that not all α-phase particles along the grain boundaries act as initiation sites for IGC. This may be related to the level of Cu in individual particles. The composition window of the constituent elements Fe, Mn and Cu are quite large for the stability of the phase, allowing significant variations of these elements from one particle to another in a given sample. The size distribution of the α-phase particles is also quite large, as shown in Fig. 3.5. The effectiveness of the cathode behaviour is expected to increase with increasing concentration of Cu in the phase. Initiation is a stochastic process and the sites at which IGC initiates first may cathodically protect from initiation at certain other sites. A Cu-film may not exist adjacent to all α-phase particles to initiate sustained IGC. Relative inertness of the Q-phase as initiation sites for IGC, as a local cathode, and its role as a barrier against IGC precipitation has been demonstrated earlier [13, 18].

GD-OES profiles for Cu (Fig. 3.12c) indicates that Cu, the noblest component in the alloy, is enriched as a result of chemical processing of the surface, in the present case both in alkaline and acid environment. According to the GD-OES results (Fig. 3.12d), the same is the case for Si. Si is enriched also on the as-received samples. This is shown to occur in the oxide (Fig. 3.11e). Fe and Mn are enriched by alkaline etching, as well known from earlier studies [22] and removed by corrosion in the acidified chloride solution [13]. In the case of these two elements, enrichment in alkaline solution occurs locally on the α-phase particles, since nearly all Fe and Mn in the alloy precipitate in the form of α-phase during the homogenization of the billets prior to extrusion. Cu and Si have significant solubility in Al. For the present temper (T5) of the AA6005 specimens, most Cu and Mg is expected to precipitate as much smaller and more uniformly distributed secondary hardening phases [5] (Mg_2Si, Q and their precursors) relative to the coarser and randomly distributed α-phase particles. The critical question is the nature of segregation of these components at the surface as a result of chemical processing as detected by GD-OES elemental depth profiling.

The difference in the depth profiles for Fe and Mn in relation to those of Cu and Si indicates that the latter two segregate much closer to the sample surface. This is verified by the fact that Si is segregated mainly in the oxide on the as-received sample (cf. Fig. 3.11e and 3.12d). The shape of the Fe and Mn profiles, in terms of formation of maxima near the surface in alkaline solution and higher, scatter than the curves for Cu and Si, suggested that the typical form of segregation of these elements was in coarse and randomly distributed particles. Smaller scatter in the profiles for Cu and Si indicates for these elements that the GD-OES data are more representative of segregation in the secondary hardening phases and/or a solid solution in the aluminium matrix rather than in the form of primary particles. This indicates that corrosion of the present alloy of interest causes relatively uniform enrichment of the noble element Cu at the surface, while the elements Fe and Mn, also nobler than Al are depleted at the surface by exposure to the acidified chloride solution. Enrichment of Cu at the surface both locally by dealloying of the α-phase and more uniformly over the entire exposed surface strengthens the role of a dominating external cathode both in the initiation and propagation of IGC.

Relatively uniform segregation of Si from solid solution into the oxide during extrusion and from the hardening phase Mg_2Si during alkaline and possibly acid etching is similarly expected to occur. However, it is expected to be in the form of a Si oxide, shown to be relatively inert as a cathode on Al [12]. The GD-OES data (Fig. 3.12e) also verifies the TEM results (Fig. 3.12d) that Mg is included in the crystalline oxide formed during extrusion. These are factors which are expected to contribute to the resistance and passivity of the oxide on the as-received surface, as observed presently in terms of increased induction time for initiation of IGC. Removal of the oxide layer together with the surface metal smeared over the intermetallic particles by surface pretreatment is thus understood as an important accelerating factor in the standard BS ISO 11846 test for IGC corrosion. Significantly added acceleration is expected by the enrichment of the noble elements as cathodes before exposure to the acidified chloride solution. The extent to which such an accelerated test, which is commonly used both in practice and research, including the present work, is realistic for the purpose deserves more realistic evaluation.

3.5 Conclusions

1. For all surface types (as-received and modified by alkaline etching, Ar-sputtering, and mechanical polishing) of alloy AA6005 investigated, IGC in acidified chloride solution was initiated at the α-Al(Fe,Cu,Mn)Si particles.

2. These particles acted as effective cathodes during the initiation phase. However, they corroded rapidly in the acidified NaCl test solution. The Cu-rich remnants of the alpha phase and Cu enrichment of the surface due to dealloying of the Al matrix alloy became significant as external cathodes.

3. No sign of IGC initiation was detected at the Q-phase particles. Q-phase was passive in relation to the α-phase as the external cathode during the initiation of IGC. Neither was it affected much by exposure to the test solution. The most significant role of the phase in IGC of the AA6005 alloy was as an inert barrier against IGC filament initiation and propagation during the initiation phase.

4. The as-received surface was covered by 8 nm thick mixed oxide consisting of γ-Al_2O_3 the spinel $AlMg_2O_4$ and.SiO_2. Due to this protective crystalline layer, along with a smeared surface layer of deformed aluminium that tended to cover the active surface, the induction time for initiation of IGC was longer (1 h) on the as-received surface than for the pretreated surface (10-15 min).

3.6 References

[1] D.G. Altenpohl, Aluminium viewed from within: an introduction into the metallurgy of aluminium fabrication, *Aluminium-Verlag*, Düsseldorf, Germany (**1982**).

[2] L.F. Mondolfo, Aluminum alloys structure and properties, *Butterworth Inc,* London, UK (**1976**).

[3] J.E. Hatch, Aluminum properties and physical metallurgy, *ASM International,* Metals Park, OH, USA (**1984**).

[4] K. Yamaguchi, K. Tohma, The effect of Cu content on susceptibility to intergranular corrosion of Al-Mg-Si, *Japan Institute of Light Metals,* 47 (**1997**) 285-291.

[5] A.K. Gupta, D.J. Lloyd, Precipitation hardening in Al–Mg–Si alloys with and without excess Si, *Materials Science and Engineering: A,* 316 (**2001**) 11-17.

[6] D.J. Chakrabarti, D.E. Laughlin, Phase relations and precipitation in Al–Mg–Si alloys with Cu additions, *Progress in Materials Science,* 49 (**2004**) 389-410.

[7] G. Svenningsen, M.H. Larsen, J.H. Nordlien, K. Nisancioglu, Effect of high temperature heat treatment on intergranular corrosion of AlMgSi(Cu) model alloy, *Corrosion Science,* 48 (**2006**) 258-272.

[8] G. Svenningsen, M.H. Larsen, J.H. Nordlien, K. Nisancioglu, Effect of thermomechanical history on intergranular corrosion of extruded AlMgSi(Cu) model alloy, *Corrosion Science,* 48 (**2006**) 3969-3987.

[9] G. Svenningsen, M.H. Larsen, J.C. Walmsley, J.H. Nordlien, K. Nisancioglu, Effect of artificial aging on intergranular corrosion of extruded AlMgSi alloy with small Cu content, *Corrosion Science,* 48 (**2006**) 1528-1543.

[10] G. Svenningsen, J.E. Lein, A. Bjørgum, J.H. Nordlien, Y. Yu, K. Nisancioglu, Effect of low copper content and heat treatment on intergranular corrosion of model AlMgSi alloys, *Corrosion Science,* 48 (**2006**) 226-242.

[11] S.K. Kairy, T. Alam, P.A. Rometsch, C.H.J. Davies, R. Banerjee, N. Birbilis, Understanding the origins of intergranular corrosion in copper-containing Al-Mg-Si alloys, *Metallurgical and Materials Transactions A,* 47a (**2016**) 985-989.

[12] M.H. Larsen, J.C. Walmsley, O. Lunder, K. Nisancioglu, Effect of excess silicon and small copper content on intergranular corrosion of 6000-series aluminum alloys, *Journal of the Electrochemical Society,* 157 (**2010**) C61-C68.

[13] K. Shimizu, K. Nisancioglu, High resolution SEM investigation of intercrystalline corrosion on 6000-Series aluminum alloy with low copper content, *ECS Electrochemistry Letters,* 3 (**2014**) C29-C31.

[14] R.M. Langford, C. Clinton, In situ lift-out using a FIB-SEM system, *Micron,* 35 (**2004**) 607-611.

[15] D. Viladot, M. Véron, M. Gemmi, F. Peiró, J. Portillo, S. Estradé, J. Mendoza, N. Llorca-Isern, S. Nicolopoulos, Orientation and phase mapping in the transmission electron microscope using precession-assisted diffraction spot recognition: state-of-the-art results, *Journal of Microscopy,* 252 (**2013**) 23-34.

[16] P. Orozco-Gonzalez, M. Castro-Roman, J. López-Rueda, A. Hernández-Rodríguez, R. Muñiz-Valdez, S. Luna-Álvarez, C. Ortiz-Cuellar, Effect of iron addition on the crystal structure of the α-AlFeMnSi phase formed in the quaternary Al-Fe-Mn-Si system, *Revista de Metalurgia,* 47 (**2011**) 453.

[17] G.E. Thompson, L. Zhang, C.J.E. Smith, P. Skeldon, Boric/sulfuric acid anodizing of aluminum alloys 2024 and 7075: Film growth and corrosion resistance, *Corrosion Science,* 55 (**1999**) 1052-1061.

[18] S.K. Kairy, P.A. Rometsch, C.H.J. Davies, N. Birbilis, On the electrochemical and quasi in situ corrosion response of the Q-Phase (AlxCuyMgzSiw) intermetallic particle in 6xxx series aluminum alloys, *Corrosion Science,* 73 (**2016**) 87-99.

[19] J.H. Nordlien, S. Ono, N. Masuko, K. Nisancioglu, Morphology and structure of oxide-films formed on magnesium by exposure to air and water, *Journal of the Electrochemical Society,* 142 (**1995**) 3320-3322.

[20] O. Lunder, J.C. Walmsley, P. Mack, K. Nisancioglu, Formation and characterisation of a chromate conversion coating on AA6060 aluminium, *Corrosion Science,* 47 (**2005**) 1604-1624.

[21] T. Sheppard, Extrusion of aluminium alloys, *Kluwer Academic Publishers*, Dordrecht, Netherlands (**2013**).

[22] O. Lunder, K. Nisancioglu, The effect of alkaline-etch pretreatment on the pitting corrosion of wrought aluminum, *Corrosion Science,* 44 (**1988**) 414-422.

Chapter 4   Effect of Constituent Copper on IGC

Abstract

Aluminium alloys in the 6xxx series, normally resistant to intergranular corrosion (IGC), may become susceptible in the presence of Cu as low as 0.1 wt.% in the alloy, combined with thermal processing. The purpose of this work is to understand the propagation mechanism of IGC on extruded and artificially aged AA6005-T5 alloy surface. Samples corroded in acidified chloride solution were characterized by electrochemical measurements, glow-discharge optical emission spectroscopy and a combination of electron microscopy techniques. Metallic Cu became enriched by dealloying as a result of acid etching, especially on the external surface, and acted as an effective external cathode in IGC initiation and propagation. Enrichment occurred in the form of a few nm thick patches of film. IGC-attacked grain-boundary (GB) surfaces were exposed by tensile fracture of the corroded samples for further characterization. These surfaces showed extensive crystallographic etch morphology, which is typical for etching of Al alloys in strong HCl acid, indicating the expected low pH of the IGC anolyte. This was in contrast to the micro-pitted morphology of the external surface, indicating a higher pH for the bulk test solution, as required by the classical electrochemical theory of propagation of localized corrosion. Cu films along the grain boundary, as well as the solute depleted zone, were destroyed by IGC filament propagation, while Cu became enriched on the widened GB walls in the tail part of the filaments by the same dealloying mechanism as on the surface grains.

4.1 Introduction

Aluminium alloys in the 6xxx-series are an important class of medium-strength Al alloys, based on the Al-Mg-Si-(Cu) system with the good strength-to-weight ratio, formability, weldability and corrosion resistance [1, 2]. However, unfavourable alloying and thermomechanical processing [2, 3] has been shown to cause IGC susceptibility, especially in the presence of Cu [4] and/or Si in excess of the Mg_2Si stoichiometric ratio [5]. Recent work has shown that Cu content in trace amounts (as low as 0.14 wt.%) can cause susceptibility, depending on the temper and the type and amount of other alloying elements [6]. The susceptibility has been related to segregation of a continuous copper-rich film of around 2 nm along the grain boundaries and a solute depleted zone adjacent to it, giving rise to microgalvanic coupling as the local driving force for IGC [6-11]. It has been claimed also that external cathodes, such as α-Al(Fe,Mn)Si and AlMgSiCu (Q-phase) phases, can be important during the initiation phase, losing their significance as they are corroded away in acidified chloride solution [12, 13].

In chapter 3, the α-phase particles were shown to corrode and Cu to become enriched at the exposed surface of particles due to selective dissolution of the active Al in acidified chloride solution. It was also found that different pretreated surfaces did not have a significant role in the initiation of IGC except for the as-received surface, which initially protected against IGC by an oxide with higher passivity formed during extrusion. However, this film corroded away within 60 min after immersion. Hence, propagation occurred on nearly identical surfaces except for the delay (induction time for initiation) for the as-received surface. It was therefore decided to focus only on IGC propagation of the as-received material in the present work.

The purpose of this chapter is to investigate the significance of small copper content, the importance of internal vs external cathodes and grain boundary structure and composition, in determining the IGC propagation mechanism of alloy AA6005-T5 in acidified chloride solution. Corrosion testing is restricted to the acidified chloride solution in view of its practical significance and relevance to our earlier work.

4.2 Experimental

4.2.1 Materials

The material focus was on extruded Al alloy AA6005-T5 as described in section 3.2.1.

4.2.2 Corrosion test

An accelerated corrosion test was performed by immersion in acidified chloride solution, consisting of 30 g NaCl and 10 ml concentrated HCl per litre adjusted to pH 0.95 at room temperature (~ 22 °C). The test duration varied in the range 1.5 - 24 h in order to investigate the effect of exposure time on the corrosion morphology. The samples were tested in the as-received condition only (section 3.2.1) without any pretreatment other than degreasing.

4.2.3 Electrochemical investigation

Cathodic polarization curves for the as-received and corroded samples were characterized, as described in section 3.2.4.

4.2.4 GD-OES and SEM/TEM characterization

GDOES analysis was performed on as-received and corroded samples as described in section 3.2.1. To gain a full picture of the corrosion morphology at the surface and along the grain boundaries by SEM, three sample preparation methodologies were used:

1. Top-view of corroded surfaces (no preparation required).
2. A cross-sectional view of the IGC path, which was obtained by casting a sample in epoxy, cutting and polishing down to 1 µm it with colloidal silica, and finally breaking off the epoxy to remove the polished sample.
3. Observing the inner surfaces at corroded grain boundaries was accomplished by machining a standard tensile testing sample and stretching it to fracture, upon which the grain walls attacked by IGC became neatly separated.

SEM imaging was performed in the secondary electron mode, using Hitachi SU6600 and Zeiss Ultra (model no 55 VP) field emission microscopes.

For investigating the chemistry of the top surface and corroded grain boundaries, TEM specimens were prepared from 24 h corroded samples given the three treatments above. The specimens were prepared by using the conventional lift-out procedure in a FEI Helios NanoLab DualBeam FIB/SEM. This is elaborated in appendix A. TEM and scanning transmission electron microscope (STEM) observations were recorded on a JEOL JEM ARM200F double corrected cold FEG microscope operating at 200 kV. Beam convergence angle of 34 mrad, a beam current of 170 pA and the expected probe size of 0.1 nm was used. GIF quantum and Centurio SDD detectors were used for simultaneous mapping of EELS and energy-dispersive X-ray spectra (EDS), respectively. The EELS collection angle was 67 mrad, and the dispersion was 0.5 eV/channel, with 2x spectrum binning, allowing fast scans with adequate energy resolution. Spatial mapping was done by power-law background subtraction and integration of the Cu-L, O-K (and C-K) core loss edges [14].

4.3 Results

4.3.1 Microstructure and corrosion morphology

The grain structure of alloy AA6005-T5 is shown in cross-section in Fig. 4.1. The alloy appears to be fully recrystallized, with larger grains at and near the surface. Fig. 4.2 shows a SEM image of the cross-section of a sample corroded for 24 h in the acidified test solution. The horizontal polished surface is the cross-section, while the vertical surface was exposed to the test solution. Significant IGC was observed over the entire exposed surface, attacking all exposed grain boundaries down to an average depth of 150 μm from the surface, with the deepest attacks reaching to a depth of about 500 μm. Some grains, which lost contact with the adjacent grains due to IGC, were removed from the surface during sample preparation.

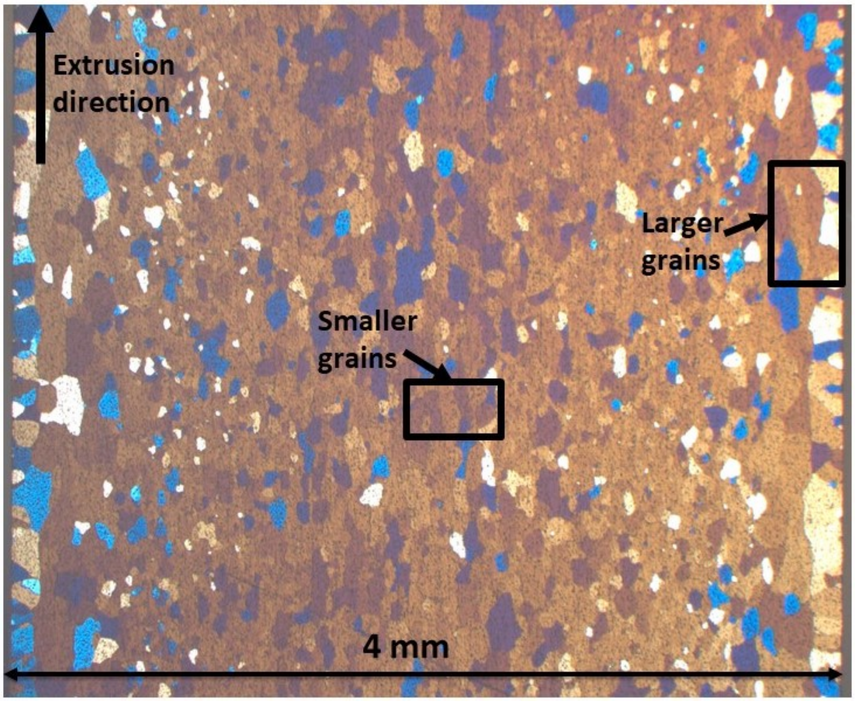

Fig. 4.1 Cross-sectional micrograph of AA6005 extruded alloy.

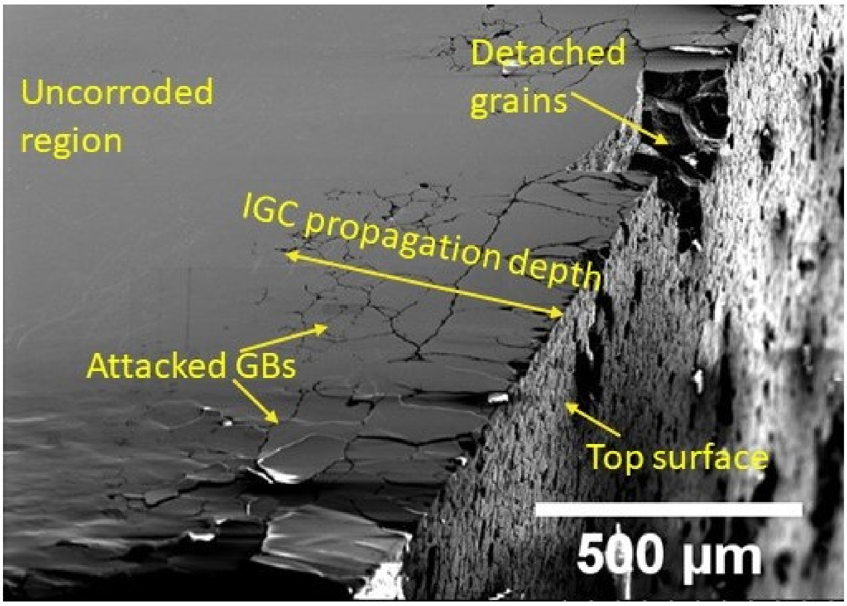

Fig. 4.2 Cross-sectional SEM image of sample corroded for 24 h in acidified chloride solution.

Fig. 4.3 shows the typical plan view images of the corroded surface. The lower magnification image in Fig. 4.3a shows the attacked grains filled with corrosion products and the grain surfaces, which were etched by exposure to the test solution. The magnified area is shown in Fig. 4.3b reveals the micro-pitted morphology of the etched grain surface. Fig. 4.4a shows the attacked grain surface by IGC. The image of the area marked in Fig. 4.4a, shown in Fig. 4.4b, reveals the crystallographic faceted surface commonly observed in localized corrosion forms of aluminium, such as tunnelling and pitting [15-17], due to significant acidification of the anolyte. The difference in the etch morphology between the interior grain walls (Fig. 4.4a and b) and the exterior grain surfaces (Fig. 4.3a and b) indicates that the pH was significantly lower in the anolyte than in the bulk test solution, as expected [18].

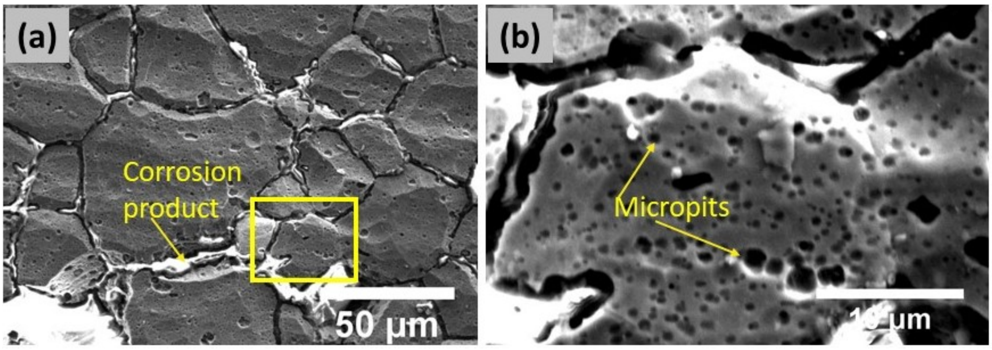

Fig. 4.3 (a) SEM image of 24 h corroded surface decorated with micropits. (b) Area marked with a yellow square in (a) at a higher magnification.

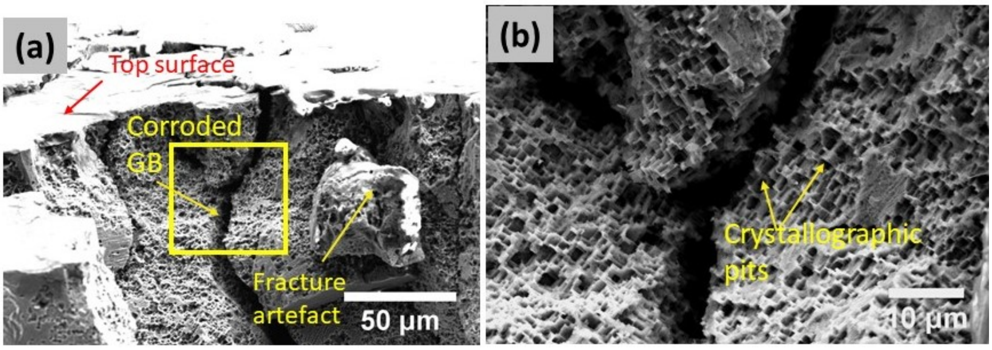

Fig. 4.4 (a) SEM image of IGC-attacked grain walls opened up by applying tensile stress perpendicular to the direction of filament propagation, showing crystallographic faceted attack. (b) Area marked with yellow square in (a) at a higher magnification.

4.3.2 Electrochemistry

Fig. 4.5 shows the corrosion potential of the AA6005 alloy as a function of exposure time in the acidified chloride solution. The decrease in the potential to a minimum at the outset is presumably related to film breakdown [18]. The corrosion potential showed a monotonic increase after 2 h of exposure, indicating an ennobling-type process increasing with the time of exposure.

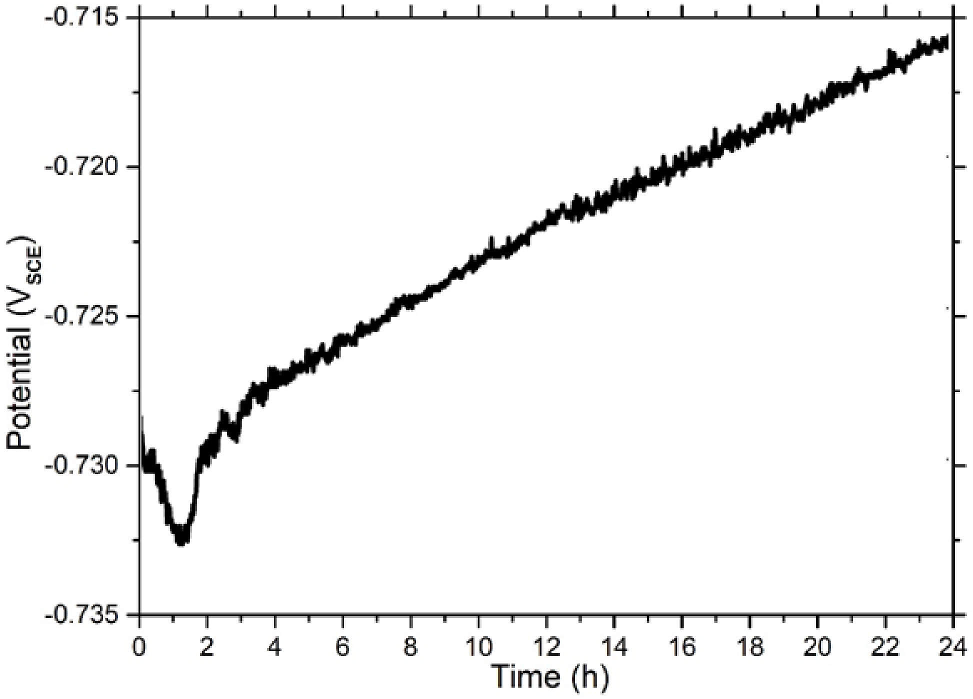

Fig. 4.5 Corrosion potential versus exposure time for the as-received AA6005 alloy in acidified chloride solution.

Fig. 4.6 shows potentiodynamic polarization curves for the as-received surface and surfaces, which were corroded for different periods of time in the acidified chloride solution. Since the cathodic and anodic parts of the curves were measured on different samples, they are presented separately in Fig. 4.6a and b, respectively. Increase in the cathodic activity was observed with increasing time of corrosion. The increase was small after 1.5 h of corrosion, which corresponds to the initiation phase, as can be inferred from the evolution of the corrosion potential in Fig. 4.5. Cathodic current density increases to an order of magnitude for 5 h corroded sample. The increase from 5 to 24 h exposure is again relatively small (although up to 10%). In contrast, the anodic curves cannot be distinguished from one another with respect to time of corrosion. This implies that the increase in the corrosion potential is not due to ennoblement due to a dealloying process. It is due to the increase in the cathodic area with increasing time of exposure to the test solution prior to potentiodynamic polarization.

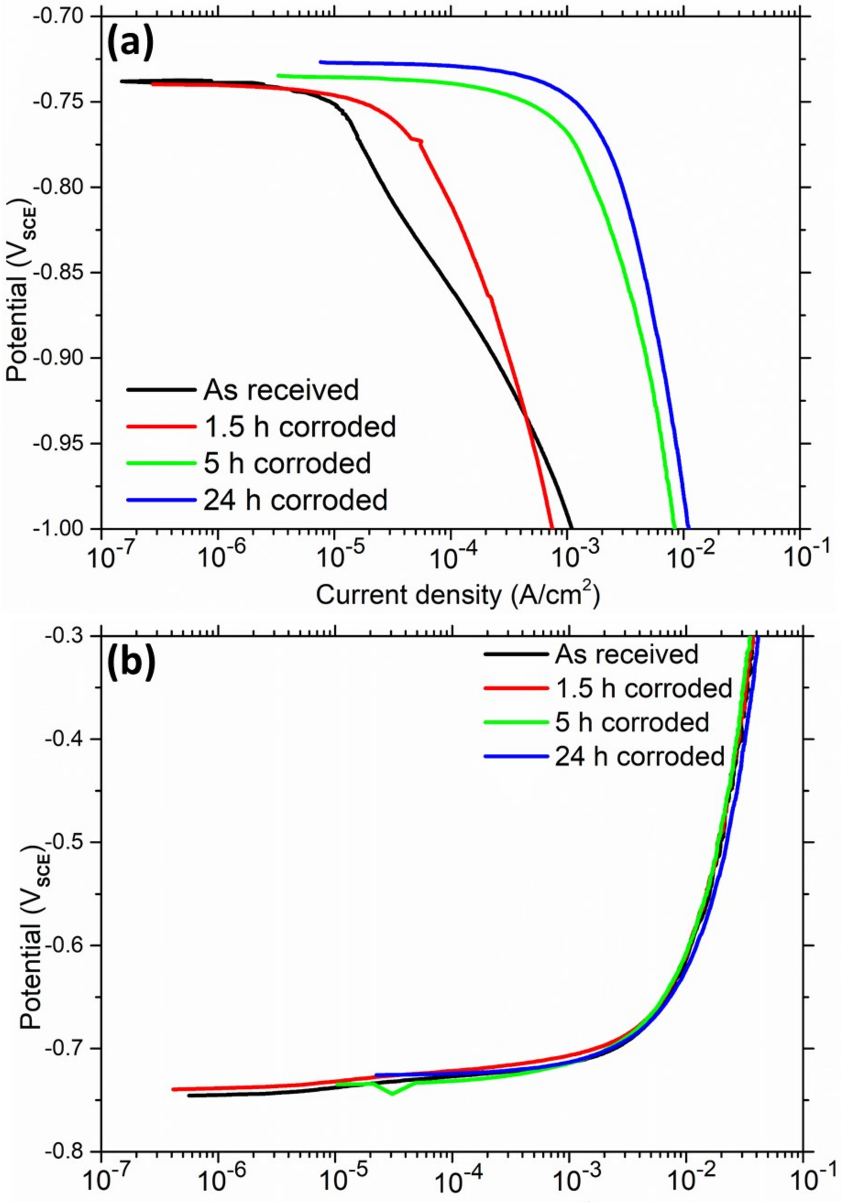

Fig. 4.6 Potentiodynamic polarization data for the AA6005 alloy in acidified chloride solution at 25 °C. (a) Cathodic. (b) Anodic.

4.3.3 GD-OES

GD-OES depth profiles in Fig. 4.7a show an increase in the Cu concentration at the surface with increasing exposure time in acidified chloride solution, indicating that the above-mentioned changes in the cathodic behaviour must be due to the enrichment of Cu on the surface by dealloying of aluminium during exposure to the test solution. The uncorroded (as-received) samples show significant Mg and Si enrichment at the surface. Possible causes for such enrichment were discussed in chapter 3. It is evident from Fig. 4.7b and c that enriched Mg are removed by exposure to the acidified chloride test solution, and Si is significantly reduced. A small enrichment of Si still appears to remain on the corroded surface. The decrease of Fe and Mn toward the as-received surface, observable in Fig. 4.6d and e, respectively, is attributed to smearing of Al metal over the α-phase particles, during extrusion, as discussed in chapter 3. Since these particles corrode in the acidified chloride solution, their profiles flatten out quickly with increasing exposure to the test solution. The slight increment of Fe towards the surface for the 1.5 h corroded sample is due to partly corroded α-phase in which Mn has completely corroded away. Nevertheless, enriched Cu becomes the dominating external cathode.

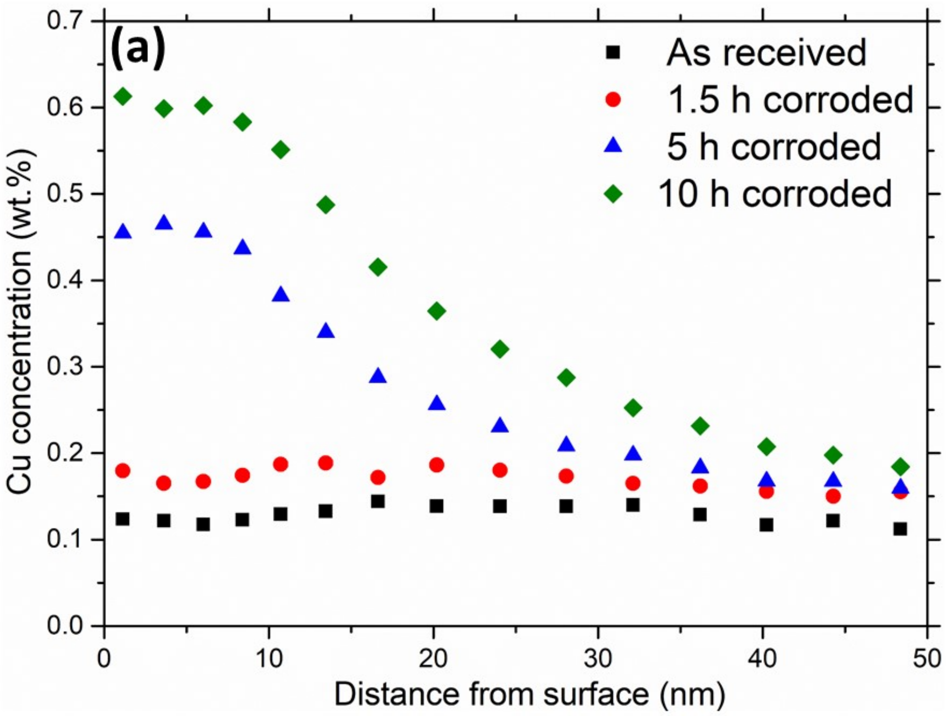

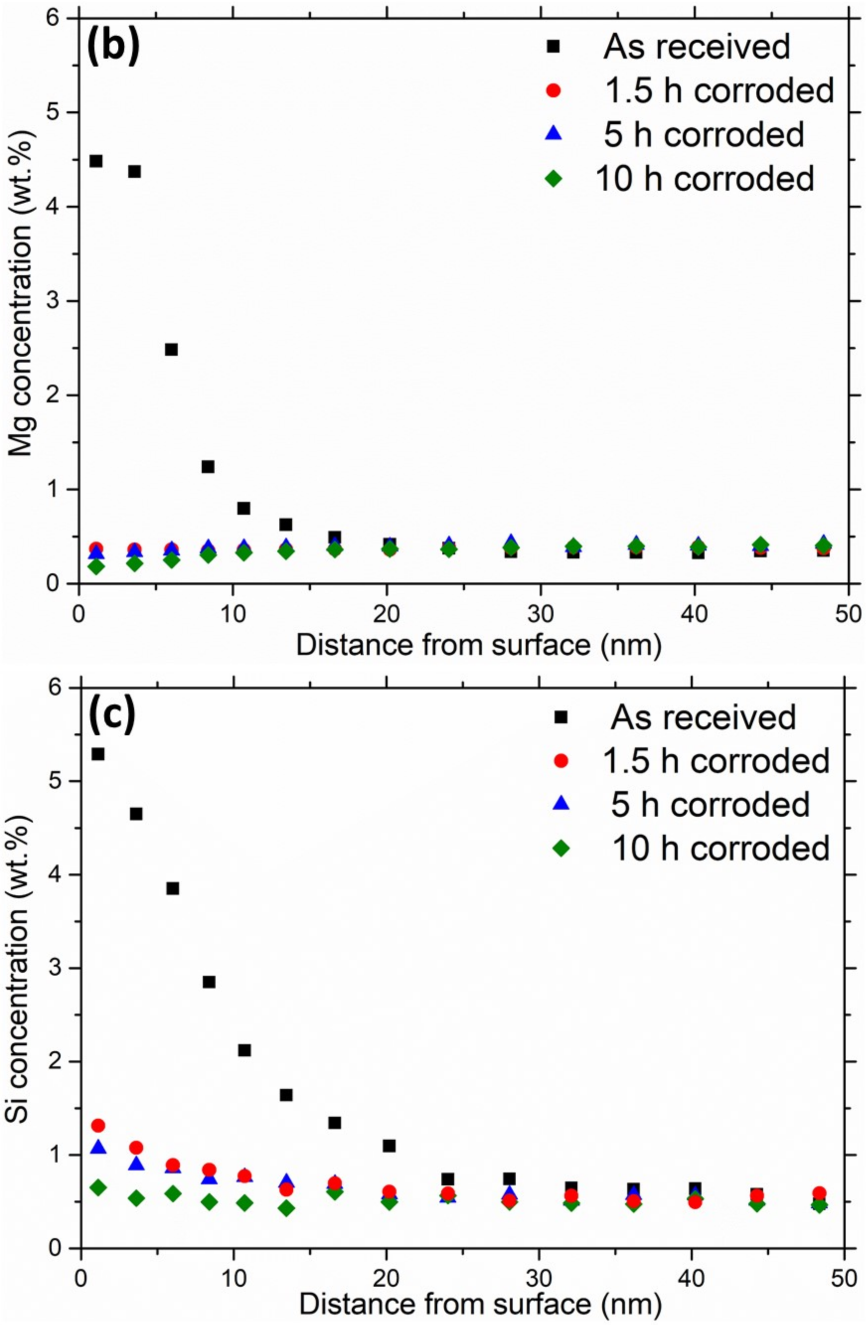
(b)
Mg concentration (wt.%)
Distance from surface (nm)
As received
1.5 h corroded
5 h corroded
10 h corroded
0
1
2
3
4
5
6
0
10
20
30
40
50
(c)
Si concentration (wt.%)
Distance from surface (nm)
As received
1.5 h corroded
5 h corroded
10 h corroded
0
1
2
3
4
5
6
0
10
20
30
40
50

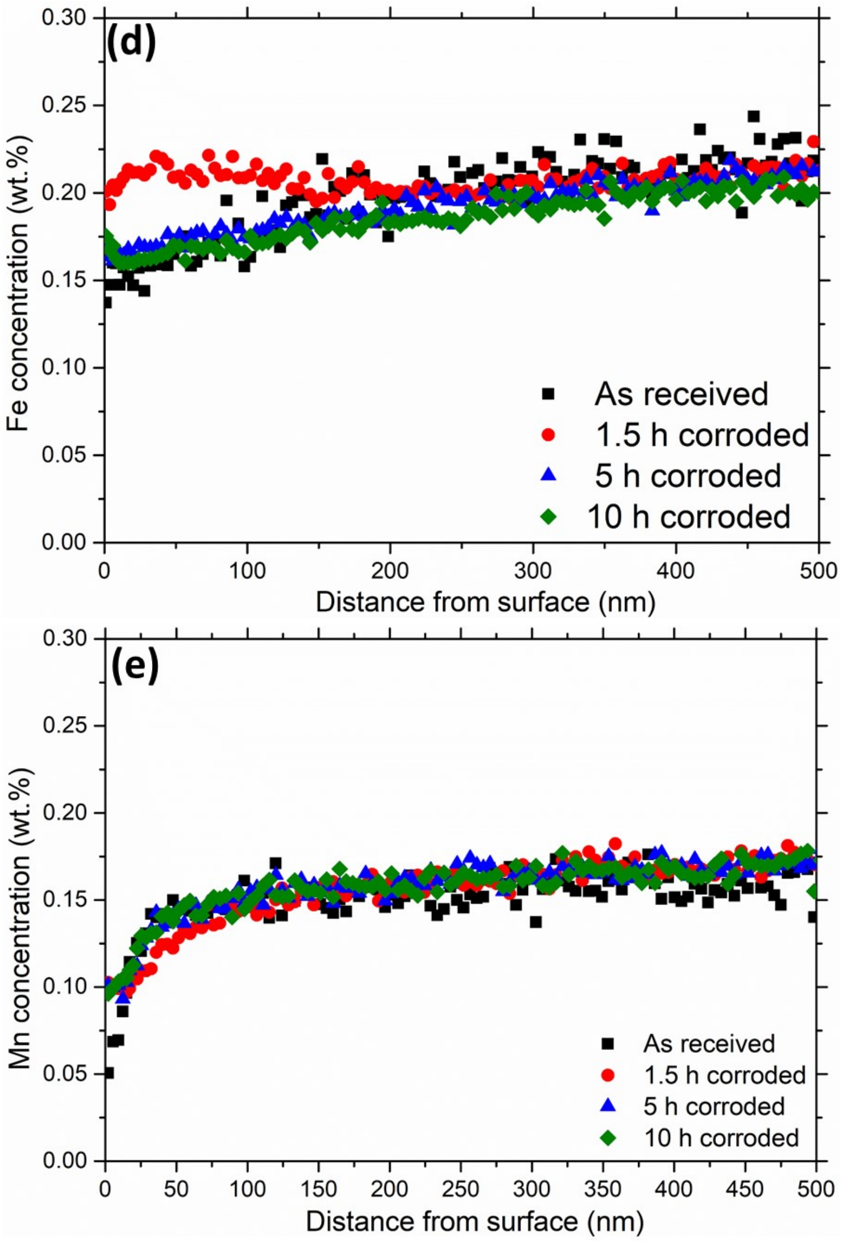

Fig. 4.7 GD-OES elemental depth profiles of (a) Cu, (b) Mg, (c) Si, (d) Fe and (e) Mn for as-received and corroded samples.

4.3.4 TEM analysis

The nature of Cu segregation by dealloying of the exposed surface and the corrosion morphology inside the IGC filaments were investigated further by use of STEM, EDS and EELS analyses of cross-sectional foils of corroded areas near the surface. Fig. 4.8a shows a cross-sectional annular dark-field (ADF) STEM image of a 24 h corroded surface revealing the metal matrix-oxide interface and a corroded grain boundary (GB). The bright particles in the bulk of Fig. 4.8a are α-Al(Fe,Mn)Si phases, as shown in appendix C (Fig. C1) [13].

The areas marked with yellow and red rectangles in Fig. 4.8a are shown at higher magnifications in Fig. 4.8b and e, respectively. Fig. 4.8c and f show EELS elemental maps of Fig. 4.8b and e, respectively, indicating that the bright features in Fig. 4.8b and e correspond to Cu. Cu was segregated as a nanofilm (Fig. 4.8e and f) at the metal-oxide interface and as discrete particles embedded in the oxide (Fig. 4.8b and c). The Cu particles in Fig. 4.8b are about 50 nm in size. Many of these were detached from the underlying Al-alloy matrix, while the Cu nanofilm in Fig. 4.8e was located along the metal matrix-aluminium oxide interface, apparently in contact with the Al matrix. The film occurred in the form of continuous patches, a few hundred nm in the direction along the interface. Results from the investigation of several similar foils are summarized in appendix C. EDS analysis of Si at the same location, as shown in Fig. 4.8d indicates the presence of Si associated with a small fraction of the Cu particles (the top particle in Fig. 4.8b and c), while Fig. 4.8g shows no Si associated with the Cu film.

The corroded GB was filled with corrosion products, as indicated by the corroded GB morphology in Fig. 4.3a and the oxide plug at the GB opening Fig. 4.8a. Some of these products were probably removed mechanically and/or chemically during specimen preparation. As earlier studies indicate, the width of GB attack was much smaller at the tip of the filament, probably confined to the width of the solute depleted zone [9]. The tail of the IGC filament broadened as a result of mechanical stress due to expanding corrosion products [19] and continuing corrosion on the walls, which resulted in the voided morphology as shown in Fig. 4.8a. The corrosion product (plug) was an Al oxide, as determined by EDS.

The cross-sectional oxide morphology on the Cu-film observed in Fig. 4.8(e,f), indicate a composite oxide film, a hydrated outer layer, probably formed during IGC, and an inner layer, probably formed during exposure of the sample to ambient atmosphere after IGC and during the preparation of the TEM foil.

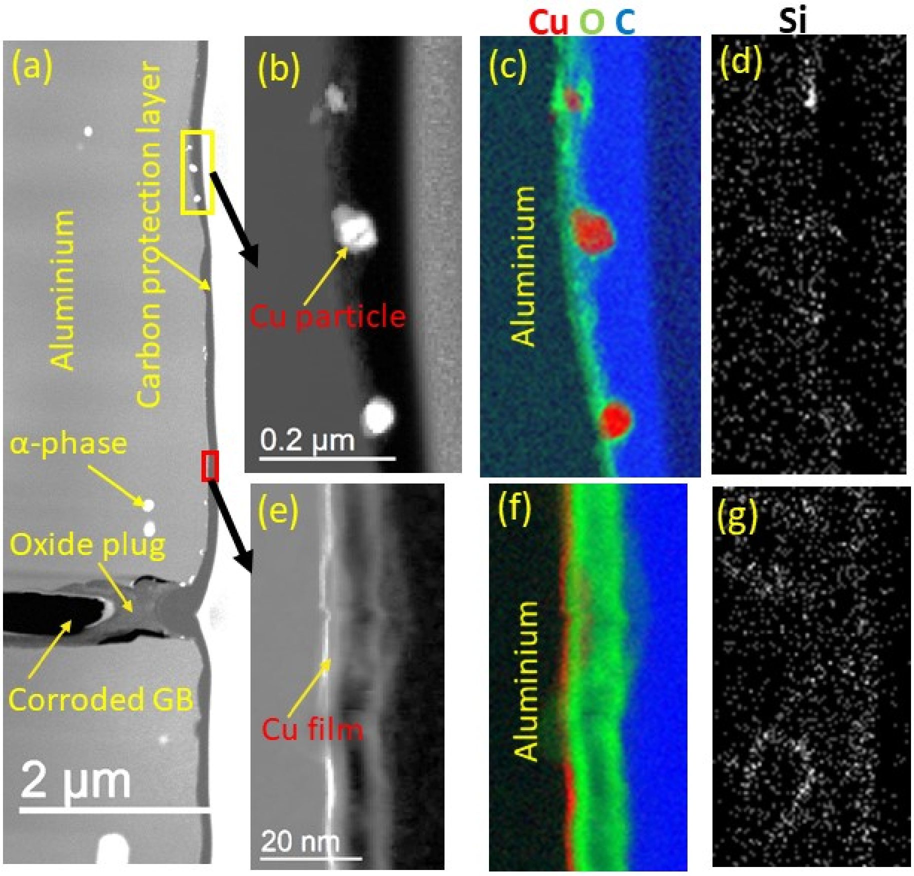

Fig. 4.8 (a) Annular dark field (ADF) STEM image of the top surface of the AA6005 sample after 24 h corrosion in acidified chloride solution. (b) Annular dark-field (ADF) STEM image of yellow box in the image (a) showing Cu particles at the matrix-oxide interface. (c) EELS maps of the image (b) where red colour corresponds to Cu, green colour corresponds to oxygen and blue colour corresponds to carbon. (d) EDS maps of Si of the image (b). (e) BF TEM image of the red box in (a) showing a 1-2 nm thick discontinuous metallic Cu-film. (f) EELS map of the image (e). (g) EDS map of Si of the image (e).

Analysis of the corroded grain surface a bit deeper in the same filament within the area marked by a rectangle in Fig. 4.9a revealed the presence of a Cu film at the metal-oxide interface (Fig. 4.9d), similar to that discussed in connection with Fig. 4.8e. It was probably formed by dealloying during broadening of the IGC filament tail by corrosion.

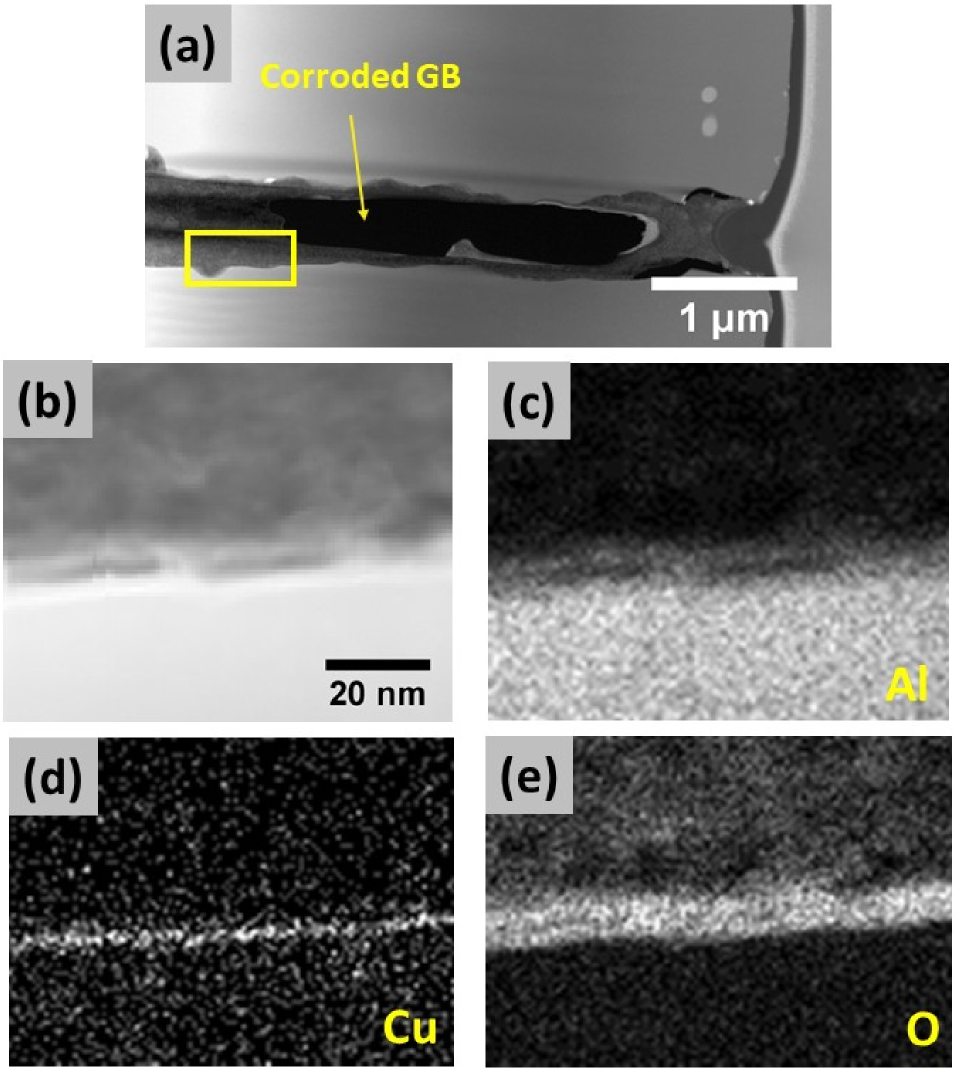

Fig. 4.9 (a) Annular dark-field (ADF) STEM image of the top surface of the AA6005 sample after 24 h corrosion in acidified chloride solution. (b) Annular dark-field (ADF) STEM image of the yellow box in the image. EDS mapping of (c) Al, (d) Cu, (e) O.

A SEM image of the IGC attacked filament surface in a GB, obtained by tensile separation along the GB is shown in Fig. 4.10. The TEM specimen was prepared from about 65 µm below the exposed surface. An ADF STEM image of this specimen is shown in Fig. 4.11a. Fig. 4.11b and e are the magnified images of the two marked areas in Fig. 4.11a, showing bright particles embedded in the aluminium oxide covering the corroded grain boundary. Fig. 4.11c and f show EELS analysis of Fig. 4.11b and e, respectively, indicating that the particles are Cu rich. In contrast to Fig. 4.9, which represents a corroded GB close to the sample surface, no Cu film or its remnants could be detected at the present depth inside the IGC filament. The EDS maps in Fig. 4.11d and g show that Si remnants may be present in the oxide. This is probably analogous to the remnants of Si detected at the surface of corroded samples in chapter 3, which was interpreted as Si formed by dealloying and existing in its stable form SiO_2 in the surface oxide or corrosion products.

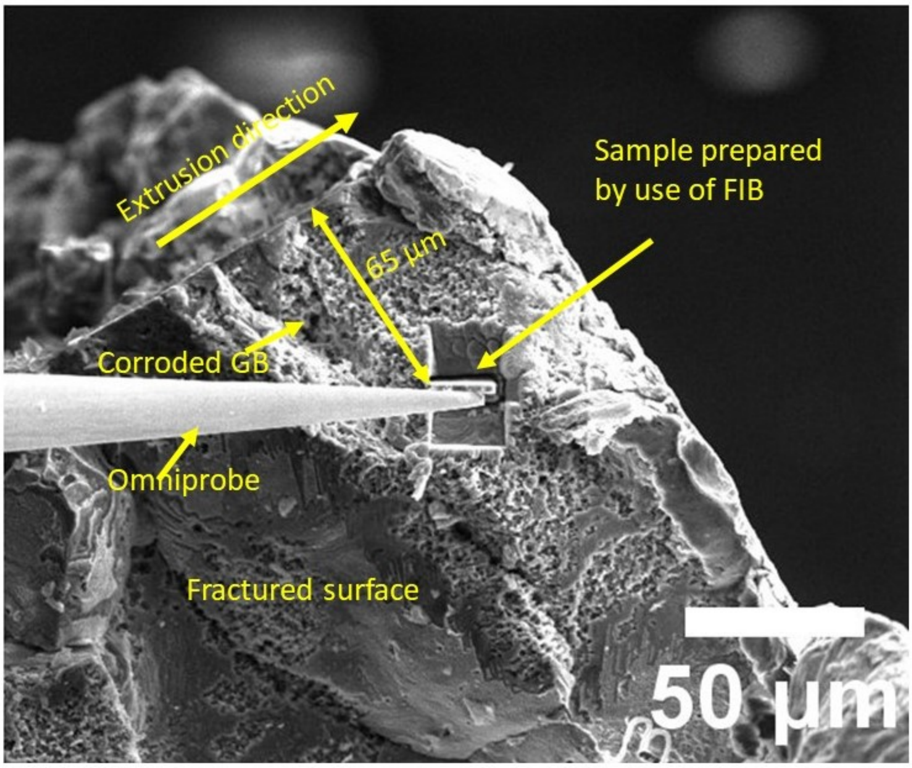

Fig. 4.10 SEM image of the fractured surface showing the location where TEM specimen was prepared by use of the FIB preparation technique described in appendix A. The milled sample is seen to be lifted from the surface by use of an omniprobe. The arrow labelled “Extrusion direction” lies parallel to the top surface exposed to the test solution.

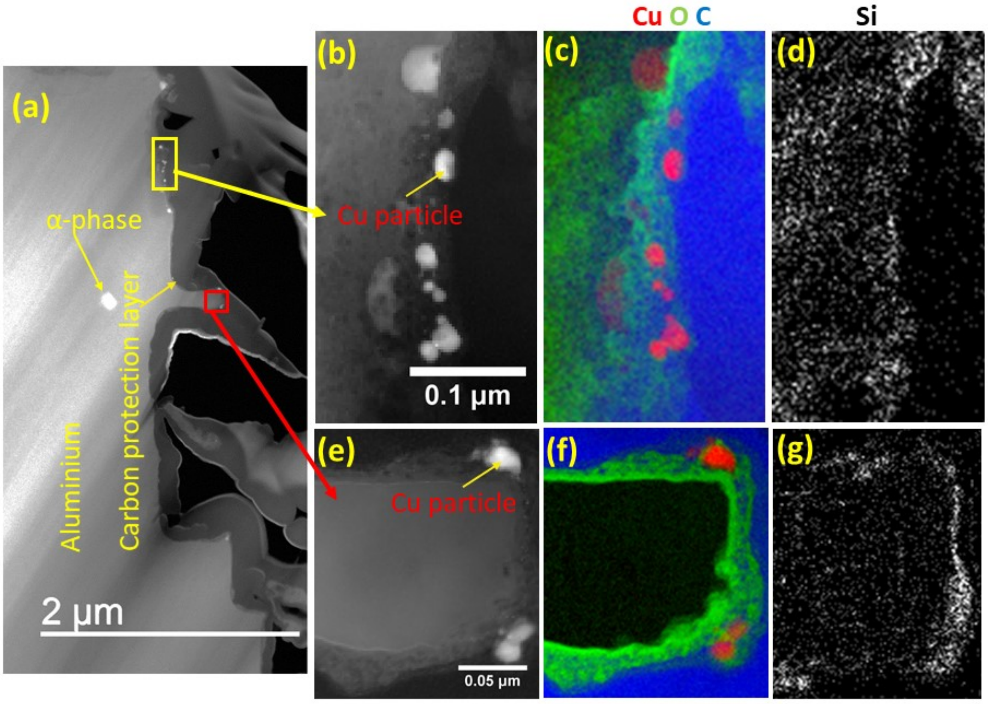

Fig. 4.11 (a) Annular dark-field (ADF) STEM image near a corroded grain boundary on the fractured surface of an AA6005 sample after 24 h corrosion in acidified chloride solution. (b) ADF STEM image of yellow box in the image (a) showing Cu particles at the matrix-oxide interface. (c) EELS map of the image (b). (d) EDS Si map of the image (b). (e) ADF STEM image of the red box in (a). (f) EELS map of the image (e). (g) EDS Si map of the image (e).

4.4 Discussion

The present work gives new evidence about the roles of external and internal cathodes in IGC of aluminium alloy AA6005. Earlier work showed that external cathodes thought to consist mainly of α-phase particles, corroded away in acidified chloride solution. Hence, the dominant cause for IGC corrosion was suggested to be due to internal cathodes in the form of segregated Cu-rich nanofilm along the grain boundaries [13]. The present results suggest that Cu becomes enriched also on the exposed external surface and corroded GB walls in the IGC attacked filaments as a result of dealloying in the presence of the acidified chloride solution. Cu is the only enriched element since it is thermodynamically immune to corrosion at the potentials observed during corrosion, while the other constituents of the material, Fe, Mn, Mg and Si, are active [20]. Although fresh α-phase particles become exposed, this process is a bit delayed since a certain thickness, commensurate with the distance between the particles, of the alloy matrix has to corrode both in the IGC filaments and the outer surface, while Cu is continuously refreshed at both locations at a faster rate by dealloying.

The present work shows that Cu is enriched in the form of a few nm thick patches of the film at the metal-oxide interface along the exterior and interior surfaces. Cu-rich films were also observed, although seldom, along with the corroded grain boundaries. These could be the remnants of the originally segregated GB film. 30-50 nm size Cu-rich particles were more common deeper in the filaments. Cu particles were observed also on the external surface, mostly embedded in the oxide layer and, therefore, detached from the metal matrix. These particles are believed to be mainly the remnants of dealloyed α-phase particles. They can also form by coarsening of the Cu film, formed by dealloying during exposure to the test solution, as the film becomes detached from the metal surface during corrosion.

The morphological dissimilarities indicate that the chemistry of the corroding external and internal surfaces are different. Dense crystallographic faceted etching internally, as opposed to the formation of the smaller density of micropits externally, indicate the formation of a considerably more acidic chloride environment internally in relation to the already acidic (pH 0.95) external environment. This is possible only with the significant participation of the external cathodes in the corrosion process. The fundamental electrochemical principle of separation of the catholyte and anolyte in localized metal corrosion is thus satisfied. With the foregoing information at hand, the earlier sketch [9] for the mechanism of IGC on 6xxx Al alloy with small Cu content can be modified to that shown in Fig. 4.12.

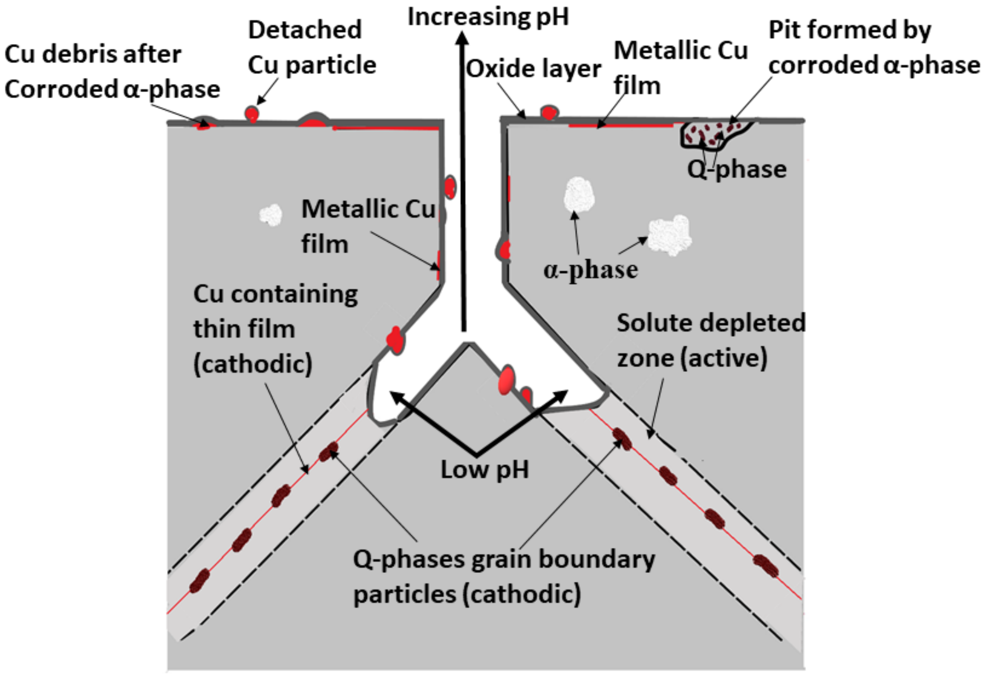

Fig. 4.12 Conceptual sketch of IGC mechanism on the AA6005 alloy.

The present study lacks chemical and morphological data for the IGC filament tip, where the rate of propagation is determined. The grain boundary film as the internal cathode and the solute depleted zone is still believed to be the dominating factors determining the propagation mechanism, probably to increasing extent, as the IGC attack propagates deeper. The role of the continuous Cu nanofilm along the grain boundaries is still deemed crucial in the propagation mechanism because breaking of the continuity by coarsening of the film into precursors of the Q-phase by aging increases the IGC resistance [8, 9]. However, the present characterization results are limited to the morphology of the tail, where the corrosion mechanism must be very similar to that of acid etching of bulk aluminium in acidified chloride solution, forming the observed crystallographic etch morphology at a later stage in the propagation process [15]. In situ investigation of propagation at the tip is not possible yet.

4.5 Conclusions

1. The cathodic activity during IGC propagation on an AA6005 alloy with small Cu content in acidified chloride solution increases with increase in the time of immersion in acidified chloride solution. This is caused by the enrichment of Cu in the propagating IGC filaments and on the outer surface as a result of dealloying.

2. Initially, the α-phase and the Cu nanofilm along the GB's are the external and internal cathodes, respectively, in driving the IGC process. As the α-phase corrodes and its replenishment is delayed because of the distance between the particles in the alloy, Cu enriches continuously at the corroding sites and becomes the dominating cathode externally and internally.

3. The difference in the etching morphology between the external surface and the IGC filaments suggests indirectly that pH is lower in the filaments than that in the bulk solution. This can occur through the participation of the external cathodes in the propagation phase. Thus, the principle of separation of the anode and cathodes in localized corrosion is satisfied.

4.6 References

[1] J.R. Davis, Corrosion of aluminum and aluminum alloys, *ASM International*, Metals Park, OH, USA (**1999**).

[2] L.F. Mondolfo, Aluminum alloys structure and properties, *Butterworth Inc,* London, UK (**1976**).

[3] J.E. Hatch, Aluminum properties and physical metallurgy, *ASM International,* Metals Park, OH, USA (**1984**).

[4] K. Yamaguchi, K. Tohma, The effect of Cu content on susceptibility to intergranular corrosion of Al-Mg-Si, *Japan Institute of Light Metals,* 47 (**1997**) 285-291.

[5] A.K. Gupta, D.J. Lloyd, Precipitation hardening in Al–Mg–Si alloys with and without excess Si, *Materials Science and Engineering: A,* 316 (**2001**) 11-17.

[6] G. Svenningsen, J.E. Lein, A. Bjørgum, J.H. Nordlien, Y. Yu, K. Nisancioglu, Effect of low copper content and heat treatment on intergranular corrosion of model AlMgSi alloys, *Corrosion Science,* 48 (**2006**) 226-242.

[7] G. Svenningsen, M.H. Larsen, J.H. Nordlien, K. Nisancioglu, Effect of high temperature heat treatment on intergranular corrosion of AlMgSi(Cu) model alloy, *Corrosion Science,* 48 (**2006**) 258-272.

[8] G. Svenningsen, M.H. Larsen, J.H. Nordlien, K. Nisancioglu, Effect of thermomechanical history on intergranular corrosion of extruded AlMgSi(Cu) model alloy, *Corrosion Science,* 48 (**2006**) 3969-3987.

[9] G. Svenningsen, M.H. Larsen, J.C. Walmsley, J.H. Nordlien, K. Nisancioglu, Effect of artificial aging on intergranular corrosion of extruded AlMgSi alloy with small Cu content, *Corrosion Science,* 48 (**2006**) 1528-1543.

[10] S.K. Kairy, T. Alam, P.A. Rometsch, C.H.J. Davies, R. Banerjee, N. Birbilis, Understanding the origins of intergranular corrosion in copper-containing Al-Mg-Si alloys, *Metallurgical and Materials Transactions A,* 47a (**2016**) 985-989.

[11] N. Birbilis, Y.M. Zhu, S.K. Kairy, M.A. Glenn, J.F. Nie, A.J. Morton, Y. Gonzalez-Garcia, H. Terryn, J.M.C. Mol, A.E. Hughes, A closer look at constituent induced localised corrosion in Al-Cu-Mg alloys, *Corrosion Science,* 113 (**2016**) 160-171.

[12] M.H. Larsen, J.C. Walmsley, O. Lunder, K. Nisancioglu, Effect of excess silicon and small copper content on intergranular corrosion of 6000-series aluminum alloys, *Journal of the Electrochemical Society,* 157 (**2010**) C61-C68.

[13] K. Shimizu, K. Nisancioglu, High resolution SEM investigation of intercrystalline corrosion on 6000-Series aluminum alloy with low copper content, *ECS Electrochemistry Letters,* 3 (**2014**) C29-C31.

[14] V.C. Angadi, C. Abhayaratne, T. Walther, Automated background subtraction technique for electron energy-loss spectroscopy and application to semiconductor heterostructures, *Journal of Microscopy,* 262 (**2016**) 157-166.

[15] M. Baumgartner, H. Kaesche, Microtunnelling during localized attack of passive aluminum - the case of salt films vs oxide-films, *Corrosion Science,* 29 (**1989**) 363-378.

[16] V. Guillaumin, G. Mankowski, Localized corrosion of 6056 T6 aluminium alloy in chloride media, *Corrosion Science,* 42 (**2000**) 105-125.

[17] I.L. Muller, J.R. Galvele, Pitting potential of high purity binary aluminium alloys Al-Cu alloys. pitting and intergranular corrosion, *Corrosion Science,* 17 (**1977**) 179-193.

[18] Z. Szklarska-Smialowska, Pitting corrosion of aluminum, *Corrosion Science,* 41 (**1999**) 1743-1767.

[19] F. Eckermann, T. Suter, P.J. Uggowitzer, A. Afseth, A.J. Davenport, B.J. Connolly, M.H. Larsen, F. De Carlo, P. Schmutz, In situ monitoring of corrosion processes within the bulk of AlMgSi alloys using X-ray microtomography, *Corrosion Science,* 50 (**2008**) 3455-3466.

[20] R. Parsons, Atlas of electrochemical equilibria in aqueous solutions, *Elsevier*, London, UK, (**1967**).

Chapter 5 Propagation of intergranular corrosion

Abstract

The purpose of this chapter is to understand the role of the properties of surface and bulk grains of extruded aluminium alloy AA 6005-T5, with small Cu content, on the rate of IGC. As-received and alkaline etched specimens were corroded for different periods to determine the rate of IGC propagation for each case. 400 μm milled surface was also used to study IGC propagation rate in the bulk structure. Propagation of IGC fissures was faster along the larger grains near the surface than along the tortuous boundaries in the bulk of the metal. Grains elongated along the direction of fissure growth enhanced, while grains elongated perpendicular to the direction of growth restricted IGC propagation. Both the corrosion depth and volume increased with time, but there was evidence for limited depth of thickness at about 250 μm, corresponding to the boundary between the large grains elongated in the direction of extrusion and underlying smaller bulk grains.

5.1 Introduction

6xxx series of aluminium alloys are generally resistant to corrosion [1]. However, unfavourable alloying and thermomechanical treatment may introduce susceptibility to IGC [2, 3]. IGC is a result of micro-galvanic cell formation at the GB, related to segregation of a Cu-rich film along the GB and a solute depleted zone adjacent to it [4-8]. We have discussed the roles played by external cathodes, such as the α-phase and Cu enrichment by dealloying of the corroding matrix in chapters 3 and 4.

Earlier studies of IGC propagation of 6xxx series have been focused mainly on the effect of alloying (in particular the role of excess Cu and Si in the alloy) and thermomechanical processing. Based on these studies it is widely agreed that, in order to avoid IGC, correct thermomechanical treatment and low Cu content must be used [4-7, 9-12]. Otherwise, there is little work on the IGC propagation mechanism emphasizing the significance of microstructural details in the 6xxx series alloys. Minoda et al. showed that less IGC occurred at the centre plane, as compared to the surface layer, of extruded material in 6061 alloys [13]. Recent work on alloy AA6005 showed that propagation of IGC fissures stopped after corrosion reached an average depth of 200-300 µm from the sample surface [14]. This depth actually corresponds to the size of larger grains at the surface in a transition to a finer grain structure in the bulk of the material, as shown in Fig. 4.1. It is not clear if this region functions as some sort of a barrier for further propagation of IGC. Hence, there is a need for further investigation of the correlation of grain structure and IGC in the 6xxx series.

In contrast to the 6xxx alloys, propagation of IGC has been studied extensively on rolled sheets of 2xxx, 5xxx and 7xxx series alloys. It occurs fastest in the long transverse direction and slowest in the short transverse direction [15-18]. IGC on alloy AA 2024-T3 spreads laterally in the beginning, as observed in the plan view of the surface [19]. The grains themselves exhibit limited etching. With extended exposure, however, more extensive intergranular attack and grain etching are observed. IGC in 5xxx alloy is related to the presence of the anodically active β-phase (Al_3Mg_2) precipitates along the GB. The IGC rate depends on the degree of sensitization (DoS), exposure time to the corrosive environment and applied potential [17, 20, 21].

It is shown in chapter 3 that the induction time for IGC initiation on the pretreated surfaces (alkaline etched, metallographically polished and Ar-sputtered) of alloy AA6005 was similar, at about 15 min, in acidified chloride solution. The as-received surface differed by having a longer initiation time (around 60 min), as a result of higher passivity provided by the oxide layer formed during extrusion. The objective of the present chapter is to investigate the effect of surface and bulk microstructures of alloy AA6005 on the propagation of IGC.

5.2 Experimental

5.2.1 Materials and pretreatment

The material focus was on AA6005 extruded Al alloy. Detailed information about the properties of this alloy is given in section 3.2.1. The procedure for alkaline etching is described in section 3.2.2. The standard alkaline etching process removes about a 15 µm layer from the surface. In addition to the 1) as-received and 2) standard alkaline-etched conditions, specimens from which a 400 µm thick surface layer was removed by 3) milling and 4) extensively deep alkaline etching, in order to expose the finer grain bulk structure, were included as the third and fourth pretreatment conditions. The milled surface was gently polished to remove the deformed layer formed during milling [22].

5.2.2 Corrosion test

Accelerated corrosion testing was performed in acidified chloride solution at room temperature (~22 °C), consisting of 30 g NaCl and 10 ml concentrated HCl per litre, whose pH was adjusted to 0.95, according to the standard BS ISO 11846B. The corrosion test duration was varied in the range 1 to 120 h in order to investigate the rate of propagation of IGC. The test solution was renewed every 24 h. The corrosion products were removed by 10 min immersion in a hot chromic-phosphoric acid solution maintained at 80 °C. The exposed weight and size of the samples were measured before and after corrosion to calculate the weight loss per area. Three replicate samples were tested for a given set of experimental parameters.

5.2.3 Profilometer measurement

A diamond tip stylus profilometer was used to measure the thickness removed due to uniform acid etching of the external surface. The measurement was done with respect to the uncorroded surface, which was obtained by coating part of the sample surface by beeswax.

5.2.4 Characterization

Cross-sectional samples of the corroded region near the surface were prepared by mounting sectioned samples in Epofix resin and metallographically grinding and polishing through successively finer grade SiC paper and diamond paste to a final 1 µm finish. A Leica MeF4 optical microscope equipped with Jentik Optic System camera and ProgRes capture v2.8.8 was used for microstructure examination. Electron Backscatter Diffraction (EBSD) images were obtained on a FESEM, Zeiss Ultra, 55 limited edition and Hitachi SU6600 FESEM operated at 20 kV with a working distance of 21 mm. The TSL OIM Analysis 7 software was used to perform data analysis. Samples for EBSD analysis were prepared by metallographically polishing further to a 0.05 µm finish with colloidal silica, followed by electro-polishing in 70 vol% methanol and 30 vol% nitric acid solution for 5 s at −30°C.

5.3 Results

5.3.1 Microstructure

Fig. 5.1 shows the cross-sectional EBSD maps of a) light alkaline-etched (15 µm removed) and b) milled samples of alloy AA6005, the latter after removing 400 µm from the surface. Light alkaline etched surface showed four layers of the different grain structure. The first layer grains (about 10 µm in size) were the smallest. The first and much larger second layer grains (Fig. 5.1a) were elongated perpendicular to the extrusion direction. The third layer grains, also large, were parallel to the extrusion direction. The smaller fourth layer (bulk) grains were randomly oriented with respect to the extrusion direction. The second and third layers of large grains together were about 400 µm thick on both surfaces of the specimens. The milled surface with 400 µm removed a layer, shown in Fig. 5.1b consisted of only smaller bulk grains. Since the relatively small thickness of metal is removed by the standard alkaline etching relative to the size of the surface grains, the in-depth microstructures of the light-etched and as-received samples were similar. The microstructures of 400 µm etched and 400 µm milled samples were also similar to one another.

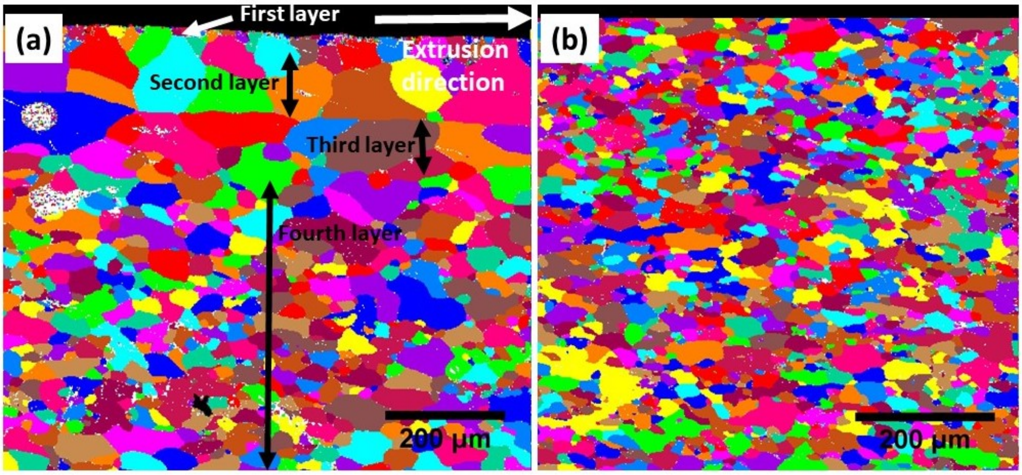

Fig. 5.1 Maps of EBSD showing grain structure in (a) alkaline etched (15 µm removed layer) surface (b) 400 µm removed layer surface.

5.3.2 Short-time IGC

Localized IGC, with one or two attacks on the overall exposed surface, occurred on the alkaline etched surface (15 µm removed layer) after 1 h exposure, as shown in Fig. 5.2a and b, while the as-received surface, shown in appendix D (Fig. D1a) did not show any IGC at all. These results are in accordance with the induction times for IGC initiation reported in section 3.3.5. The maximum depth of IGC fissures was about 150 µm on the etched surface after 1 h exposure (Fig. 5.2a and b). About 3 to 4 localized IGC attacks occurred after 5 h exposure (Fig. 5.2b and c), and a maximum depth of corrosion was around 200 µm (Fig. 5.2c and d). After 10 h, the number of localized IGC increased significantly (Fig. 5.2e) and the maximum depth of corrosion was around 300 µm (Fig. 5.2f). IGC attack spread over the entire surface with increasing time of exposure (15, 20 and 24 h in Fig. 5.2g, i and k, respectively). Maximum depth of corrosion for 15 and 20 h (Fig. 5.2f and h) exposure times was about the same as that for 10 h exposure (300 µm). At this stage, the in-depth growing fissures reached the boundary between the second (perpendicular to the extrusion direction) and third (parallel to the extrusion direction) layers of the coarse, near-surface, grains, discussed above in relation to Fig. 5.1. In-depth propagation appears to become arrested by the third layer grains, which act as temporary barriers. However, the third layer enhances the increased lateral growth of the IGC fissures. After 20 h of exposure, the propagation rate increases again (Fig. 5.3). As can be inferred from Fig. 5.2l, the fissures probably penetrate through the barrier structure (layer 3), entering the bulk structure with the smaller grains, whose grain boundaries are not as active as those of the coarser, laterally elongated layer 3 grains. Deepest attack measured after 24 h exposure was around 510 µm, as shown in Fig. 5.2l appreciably propagated into the bulk structure.

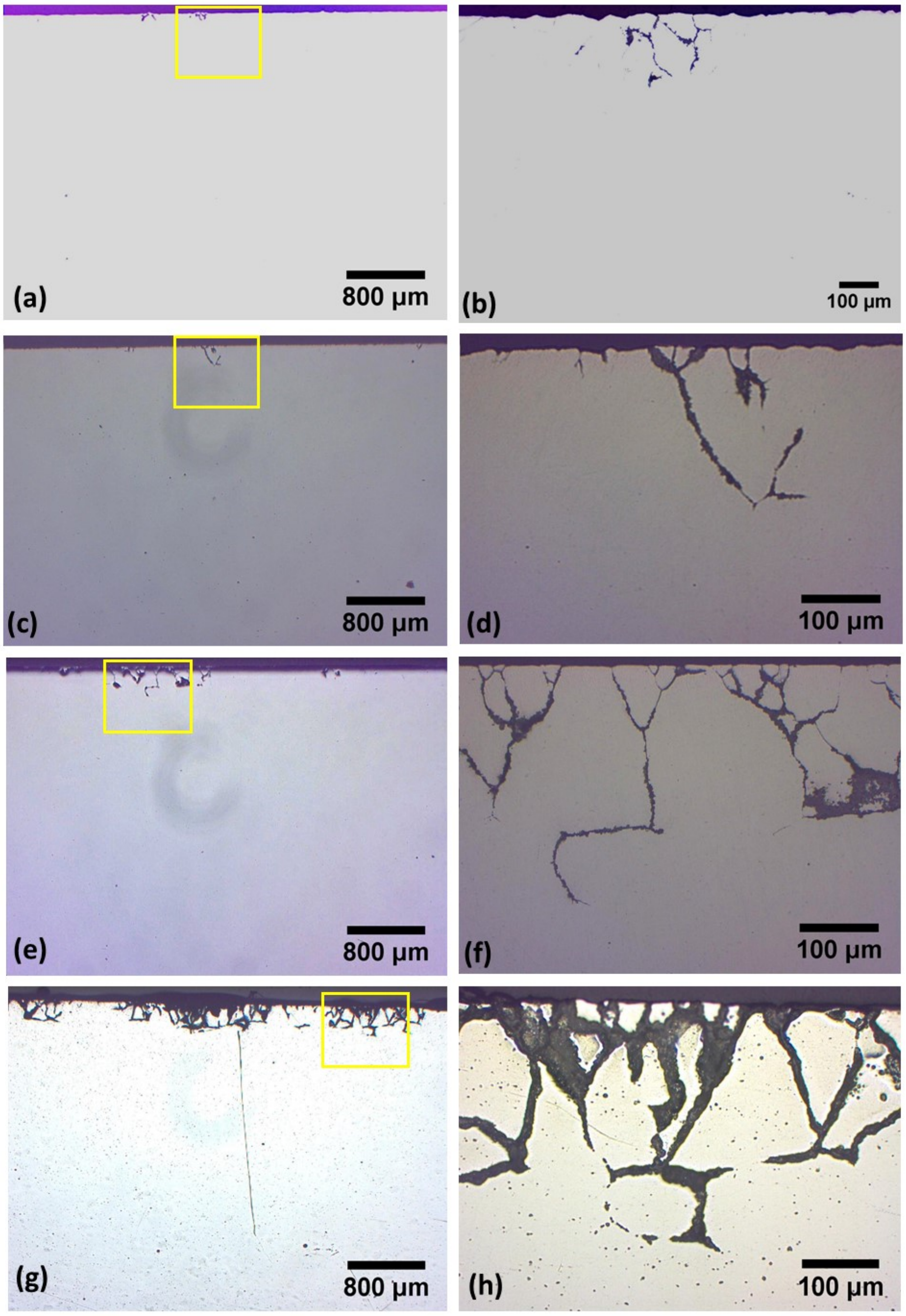
(a)
800 µm
(b)
100 µm
(c)
800 µm
(d)
100 µm
(e)
800 µm
(f)
100 µm
(g)
800 µm
(h)
100 µm

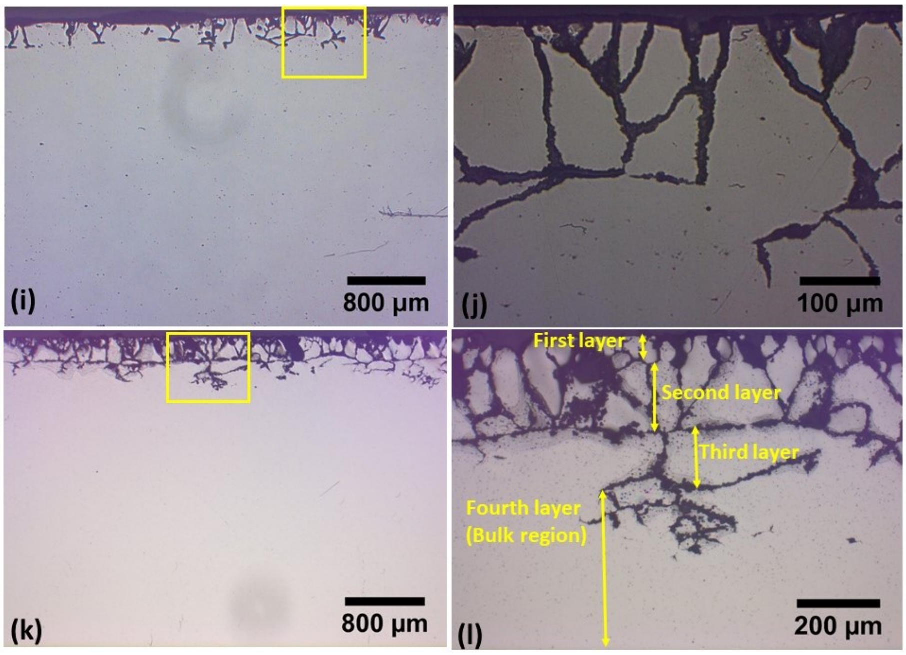

Fig. 5.2 Cross-sectional optical micrographs of alkaline etched surface after different exposure times to the test solution: (a) Exposed for 1 h. (b) Magnified image of area marked with yellow box in (a). (c) Exposed for 5 h. (d) Magnified image of area marked with yellow box in (c). (e) Exposed for 10 h. (f) Magnified image of area marked with yellow box in (e). (g) Exposed for 15 h. (h) Magnified image of area marked with yellow box in (g). (i) Exposed for 20 h. (j) Magnified image of area marked with yellow box in (i). (k) Exposed for 24 h. (l) Magnified image of area marked with yellow box in (k).

The results for the as-received sample, shown in appendix D (Fig. D1), were quite similar to those described for the etched with a slight delay at the outset due to the difference in the induction times. This delay loses its significance after about 5 h of exposure to the test solution. Fig. 5.3 shows the summary of maximum depth of attack as a function of time for both as-received and alkaline etched surfaces. It reveals also the effect of different induction times on propagation for the first few hours. After that, the rate of penetration is very similar for the two surfaces within the limits of scatter. The penetration depth is characterized by a rapid increase after initiation of the IGC fissures to a plateau, which indicates arrest of growth in depth for about 10 h, after which IGC continues to grow in depth again. These results regarding propagation in-depth agree with the visualization of the fissure growth on cross-sectional samples, as presented above (Fig. 5.2).

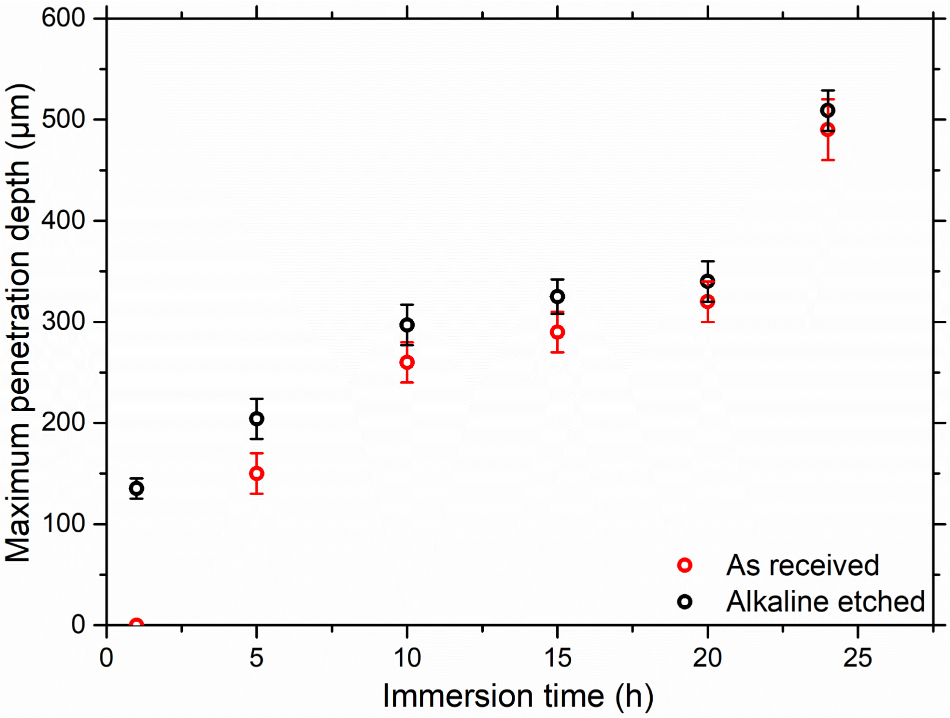

Fig. 5.3 Maximum depth of IGC attack as a function of immersion time for alkaline etched and as-received surfaces.

Measured total weight loss as a function of time for the two initial surface conditions are shown in Fig. 5.4a. The figure includes also the average reduction in thickness calculated from the weight loss by use of Faraday's law. In contrast to the penetration depth (Fig. 5.3), weight loss shows a monotonic increase over the same period of time. A temporary arrest is not observed. The factors contributing to the result in Fig. 5.4a, which are not included in the penetration-depth results reported in Fig. 5.3, can be

- the increase in the lateral growth of the fissures as suggested by Fig. 5.2g,
- removal of grains from the surface by excavation as indicated by Fig. 5.2k, and
- uniform etching of the grain surfaces at the very top (layer 1 and layer 2) and in the IGC fissures, which results in widening of the tails.

In order to determine the contribution to weight loss by etching of the outermost surface, profilometry was used to estimate the reduction of thickness between the uncorroded surface and the outermost surface of the coarse grains by uniform etching, as described in section 5.2.3. Reduction in thickness could not be reliably estimated for the samples corroded for the short-time period because the measured values were of the same order as the experimental error (around 1 µm). For the 24 h corroded samples, the etched thickness was 3 ± 2 µm, where the estimated error limit was due to local variations. The profilometer data can, therefore, be considered to provide at best a qualitative idea about the magnitude of thickness reduction by uniform etching of the outermost crystal surfaces. Its contribution to total weight loss is negligible compared to the other factors cited above.

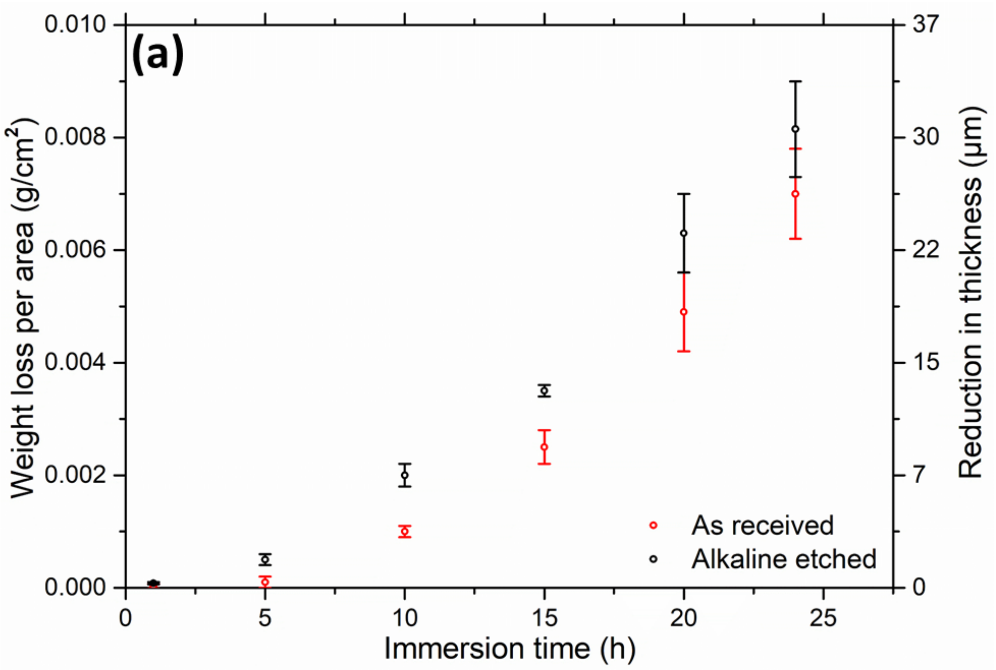

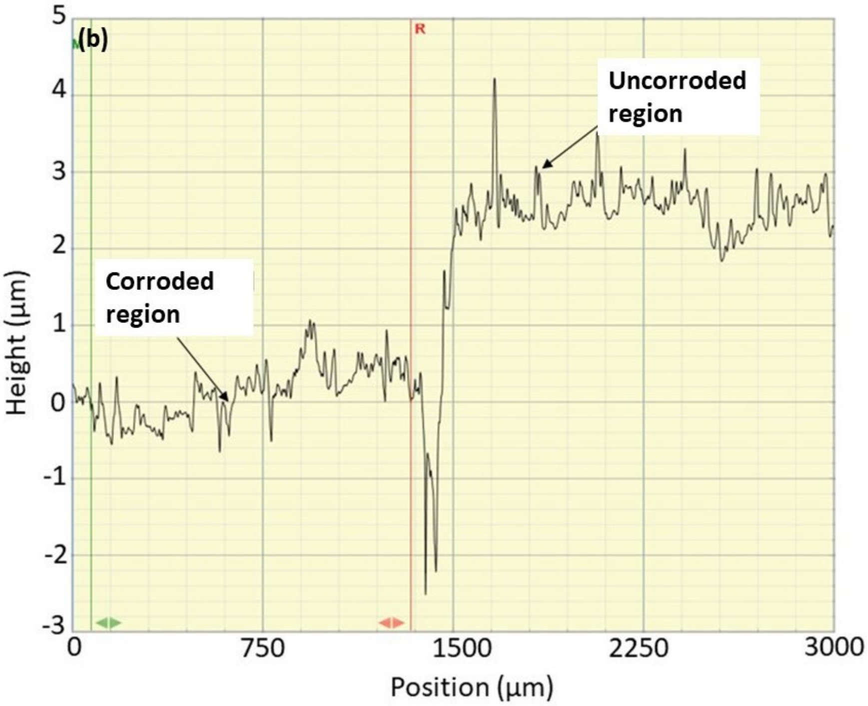

Fig. 5.4 (a) Weight loss and the average reduction in thickness, calculated from weight loss, for as-received and alkaline-etched samples as a function of immersion time in acidified chloride solution. (b) Profilometer profile of 24 h corroded sample adjacent to the surface protected against corrosion by beeswax.

5.3.3 Long-time IGC

Fig. 5.5 shows IGC attack morphologies after extended periods (48, 72, 96 and 120 h) of immersion of alkaline etched surface (15 µm removed) in acidified chloride solution. Fig. 5.5a and b show that most of the surface grains in the first and second layer were corroded or physically removed after 48 h of testing. Penetration into the next layer (third layer) appears to be delayed and localized. After longer exposure times (72, 96 and 120 h), IGC propagation continues into the smaller-grain bulk structure, as shown in Fig. 5.5c and d, Fig. 5.5e and f and Fig. 5.5g and h, respectively.

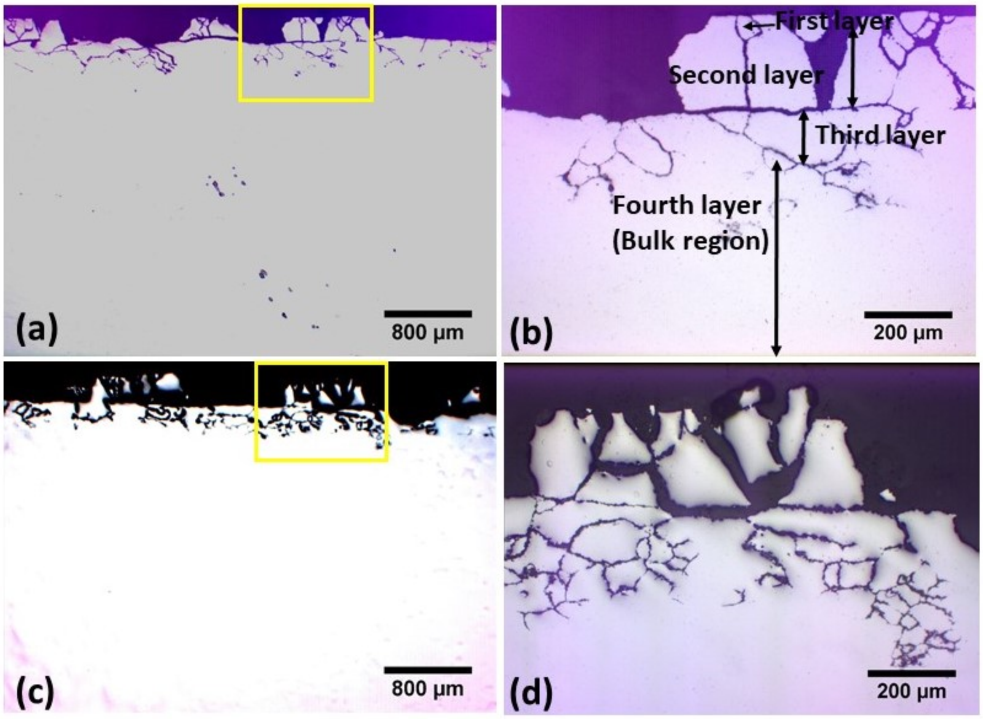
(a)
800 µm
First layer
Second layer
Third layer
Fourth layer
(Bulk region)
(b)
200 µm
(c)
800 µm
(d)
200 µm

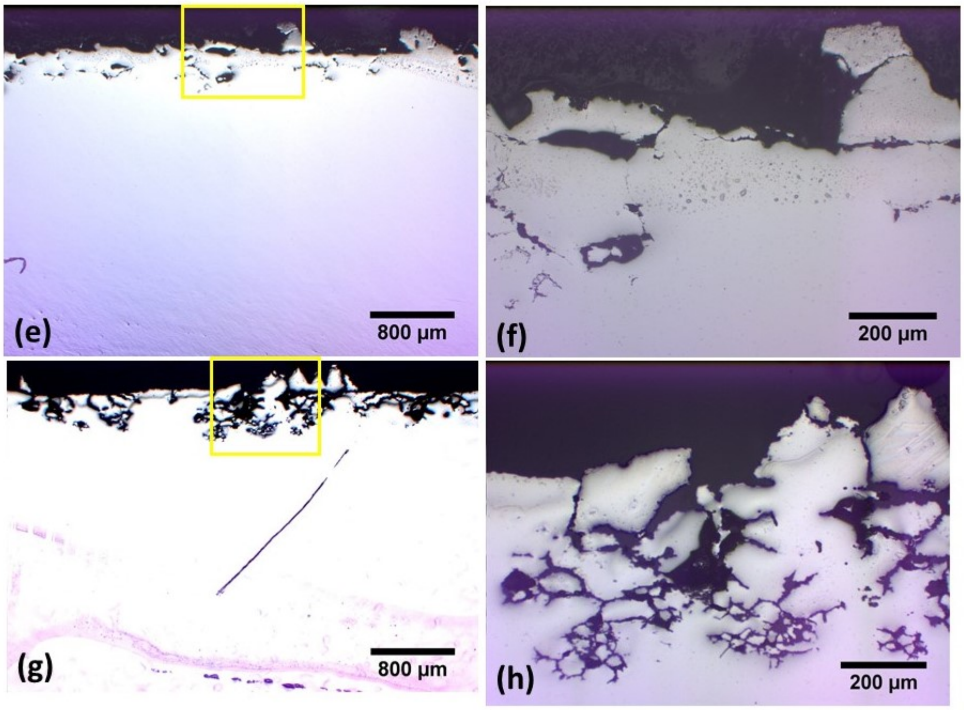

Fig. 5.5 Cross-sectional optical micrographs of alkaline etched surface (15 µm removed layer) after longer times of exposure to acidified test solution: (a) After 48 h. (b) Magnified image of area marked with yellow box in (a). (c) After 72 h. (d) Magnified image of area marked with yellow box in (c). (e) After 96 h. (f) Magnified image of area marked with yellow box in (e). (g) After 120 h. (h) Magnified image of area marked with yellow box in (g).

5.3.4 IGC on 400 µm milled surface

The first three layers of coarse grain structure were removed mechanically by milling or chemically by extended alkaline etching of the surface to a thickness of 400 µm, thus exposing the finer bulk grain structure, as shown above in Fig. 5.1. Initiation and propagation of IGC directly on the bulk structure was investigated for a better understanding of the IGC propagation mechanism from the coarse-grained layers into the finer grained bulk layer. Corrosion results for 400 µm milled surface and 400 µm alkaline etched surfaces were identical. Therefore, only the results for 400 µm milled sample are shown in this section. The results for 400 µm alkaline etched surface are summarized in appendix D (Fig. D4 and Fig.

D5). Contrary to the surface variants with the coarse-grained layers, IGC did not initiate for 24 h on the surface with the bulk grains exposed [shown in appendix D (Fig. D2)]. Fig. 5.6 shows IGC propagation on milled-surface cross sections obtained after longer immersion times in the range 48 to 120 h. Since it was sometimes difficult to conclude from the cross-sectional images whether the attack was IGC, pitting corrosion or both, SEM plan view images of some of the selected samples, shown in appendix D (Fig. D5), were examined with the conclusion that IGC dominated. Localized IGC with 410 µm propagation depth (Fig. 5.7a,b) was observed on the milled sample after 48 h immersion time. IGC attack spread mostly laterally after larger times of immersion, as shown for 72 h, 96 h and 120 h immersion times in Fig. 5.7(c,d,e,f,g,h).

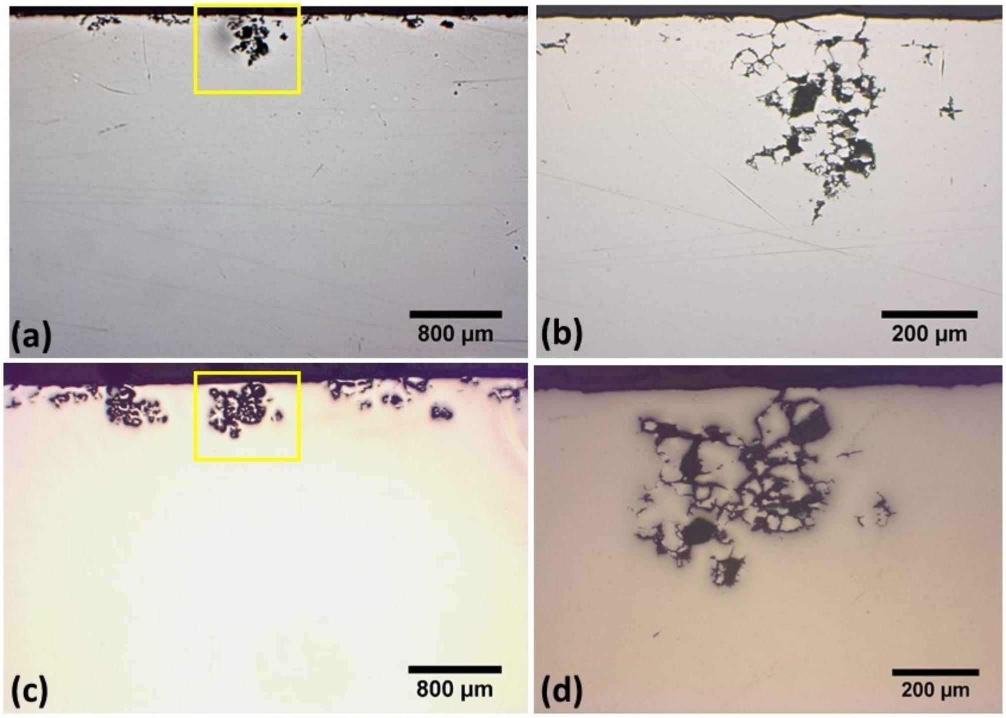

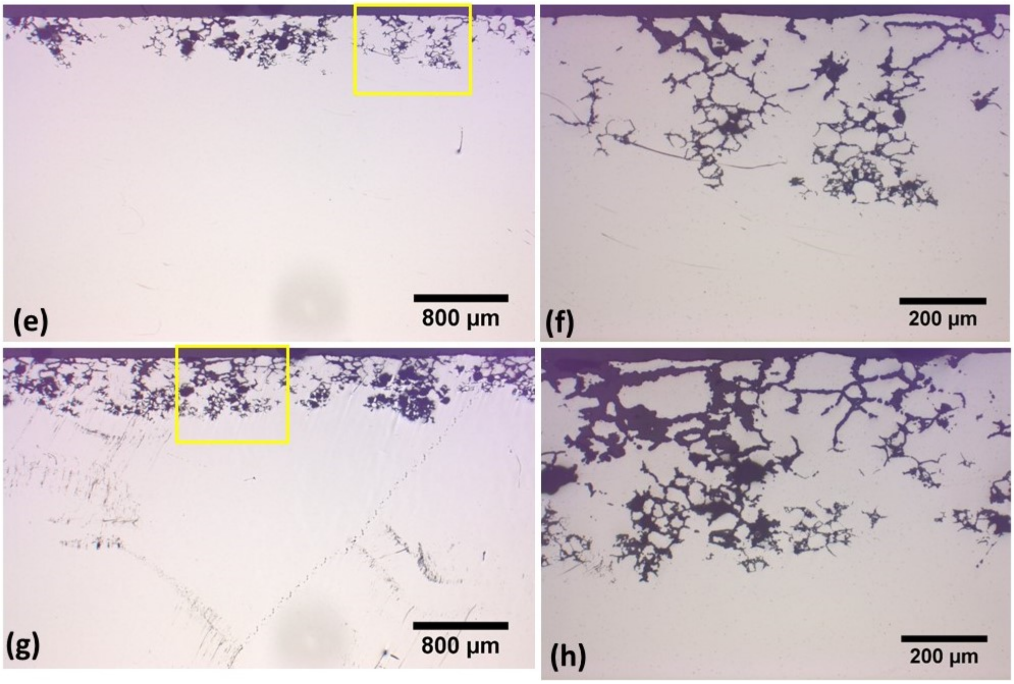

Fig. 5.6 Cross-sectional optical micrographs of 400 µm milled surface after different immersion times: (a) After 48 h. (b) Magnified image of area marked with yellow box in (a). (c) After 72 h. (d) Magnified image of area marked with yellow box in (c). (e) After 96 h. (f) Magnified image of area marked with yellow box in (e). (g) After 120 h. (h) Magnified image of area marked with yellow box in (g).

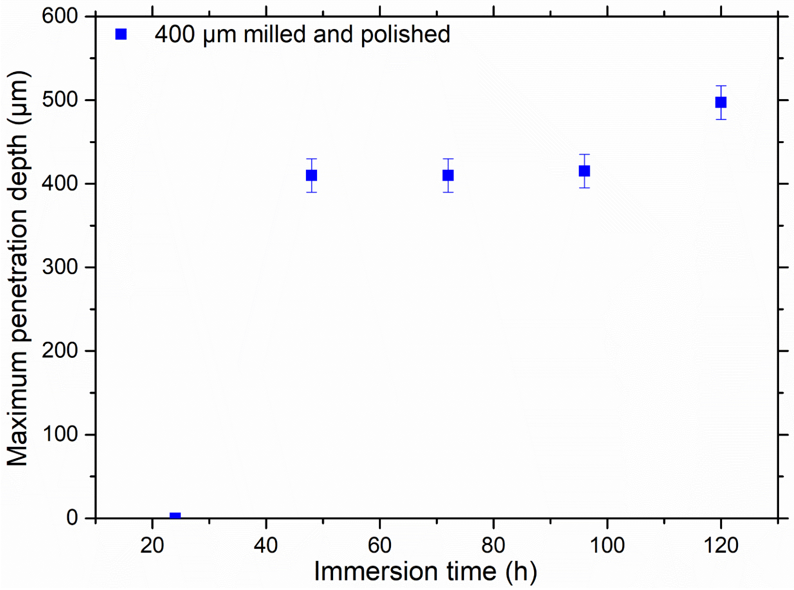

Fig. 5.7 Maximum depth of IGC attack as a function of immersion time for 400 µm milled and polished surface.

Fig. 5.7 shows that IGC penetration rate on the milled surface after the 24 h induction time discussed above is fast at the outset. After about 48 h of immersion, penetration nearly stops, in agreement with the cross-sectional images above. The attack occurred mostly laterally at longer times, as indicated by the cross-sectional images in Fig. 5.6. IGC propagation was on the average slower in the bulk grains as compared to the coarse grains (Fig. 5.2). Summary of weight loss data for the samples with different surface treatments is shown in Fig. 5.8. It can be seen that the IGC propagation rate on the milled surfaces was significantly lower than surfaces, which were only lightly etched (15 µm removed and therefore initially covered by the first, second and third layers).

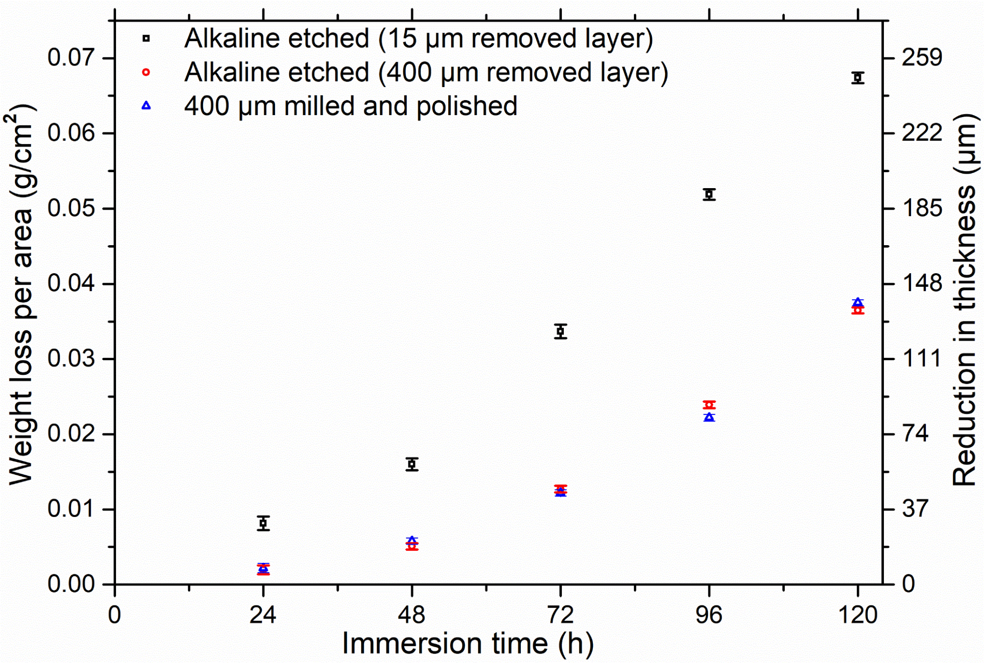

Fig. 5.8 Measured weight loss and calculated weight loss results obtained from immersion corrosion testing in acidified chloride solution for alkaline-etched and milled surfaces.

5.4 Discussion

The results in this chapter demonstrate that the geometrical structure of the grain boundaries, such as size and elongation with respect to the direction of propagation, is an important factor in determining the rate of IGC propagation. As also shown by earlier theoretical calculations on a simple geometrical model [23], the fissures are expected to propagate faster if the grains are elongated in the direction of propagation than along that elongated perpendicular to the direction of propagation because of the difference in the distance to traverse for the two cases. Since the latter orientation acts as a barrier layer, fissures change direction from in-depth to the unblocked lateral propagation once the third layer of grains is reached. This favours more rapid lateral spreading of the fissures than in-depth propagation until penetration into the finer grained bulk of the material occurs. This description agrees with the penetration depth data in Fig. 5.3, which show a significant reduction in in-depth penetration once the fissures reach the boundary between the two types of layers.

Similar geometrical arguments as for the surface layers may be used to explain the slower propagation rate of IGC in the bulk of the material, characterized by smaller and randomly shaped grains, in relation to the coarser size and geometrically more ordered structure of the grains near the surface. The former structure gives a more tortuous and longer path for the IGC fissures to propagate.

The present results show a new example for the surface dependence of the initiation mechanism of IGC for initiation simulated for the bulk structure of the AA6005 samples by removing the surface layers altered by the extrusion process. While initiation was fast on the light, 15 µm etched samples (Fig. 5.2k), initiation was delayed significantly by about 24 h on the bulk structure exposed by removal of 400 µm thick surface layer by deep milling or etching. Increased resistance to IGC is attributed simply to the removal of the top layers with grain boundaries sensitized by the thermomechanical processing, including extrusion and subsequent heat treatment. The higher IGC resistance of the bulk grain boundaries is attributed to the discrete, rather than continuous, precipitation of Cu along the grain boundaries, which in turn is related to the smaller misorientation of the bulk grain boundaries in relation to the surface layers, as will be discussed in more detail in the next chapter.

The foregoing mechanism of delay in the initiation of IGC on the surface representing the bulk microstructure obtained by milling or deep alkaline etching suggests that microstructural factors besides geometry also contribute to the propagation rate of the IGC fissures. The delay in the passage of fissures from layer 2 to the bulk can be explained by a mechanism similar to that, which delays initiation of IGC on the milled and 400 µm etched surfaces, i.e., the delay is not purely geometrical. In contrast, the delay in the passage between the coarse surface grain layers 2 and 3, which is a more geometrical type of barrier, appears to be smaller than penetration through the grain layer 3. These barrier effects between different layers cause enhancement of lateral growth of the fissures rather than in depth, which is also a purely geometrical and intuitively expected phenomenon.

In contrast to the above, propagation of fissures also appears to become arrested after reaching a depth of about 400 µm. The cause of this observation is not clear since any barriers of the types discussed above were not detectable. However, enhancement of lateral propagation instead of in-depth propagation similar to the above cases was still observed. The possible causes of this type of barrier effect must then be quite different from purely geometrical or microstructural. We tentatively suggest restrictions related to electrochemical phenomena to be discussed also in the next chapter together with additional data reported there.

As shown in chapter 3, initiation of IGC is delayed on the as-received surface as compared to the alkaline etched surface, due to the presence of the protective crystalline oxide formed during extrusion. This delay also affects the propagation rate during the first few hours of immersion in the test solution. After the protective layer is corroded away, the rate of propagation increases to about the same level as the alkaline etched surface.

5.5 Conclusions

1. Coarse surface grains on extruded AA6005 alloy are more susceptible to IGC than the bulk grains.

2. The grain size and geometry affect the IGC rate. Propagation of IGC fissures along longer and straighter grain boundaries around larger grains is faster than that along tortuous boundaries around smaller grains. Grains elongated along the direction of fissure growth enhance, while grains elongated perpendicular to direction of growth restrict net IGC penetration in depth.

3. Propagation of IGC is perpendicular to the extruded surface in the beginning, following grain boundaries of coarse surface grains elongated perpendicular to the exposed surface (extrusion direction). When the fissures reach the underlying grains elongated along the extrusion direction, they start spreading laterally.

4. Propagation from the large grained structure of the surface into the smaller grain structure of the bulk is restricted, dropping the growth rate to a limiting value. This is probably due to preferential lateral growth of the fissures along the boundary between the surface and bulk grains and restricted growth into the tortuous structure of the bulk metal.

5.6 References

[1] L.F. Mondolfo, Aluminum alloys structure and properties, *Butterworth Inc,* London, UK (**1976**).

[2] K. Yamaguchi, K. Tohma, The effect of Cu content on susceptibility to intergranular corrosion of Al-Mg-Si, *Japan Institute of Light Metals,* 47 (**1997**) 285-291.

[3] A.K. Gupta, D.J. Lloyd, Precipitation hardening in Al–Mg–Si alloys with and without excess Si, *Materials Science and Engineering: A,* 316 (**2001**) 11-17.

[4] G. Svenningsen, M.H. Larsen, J.H. Nordlien, K. Nisancioglu, Effect of high temperature heat treatment on intergranular corrosion of AlMgSi(Cu) model alloy, *Corrosion Science,* 48 (**2006**) 258-272.

[5] G. Svenningsen, M.H. Larsen, J.H. Nordlien, K. Nisancioglu, Effect of thermomechanical history on intergranular corrosion of extruded AlMgSi(Cu) model alloy, *Corrosion Science,* 48 (**2006**) 3969-3987.

[6] G. Svenningsen, M.H. Larsen, J.C. Walmsley, J.H. Nordlien, K. Nisancioglu, Effect of artificial aging on intergranular corrosion of extruded AlMgSi alloy with small Cu content, *Corrosion Science,* 48 (**2006**) 1528-1543.

[7] G. Svenningsen, J.E. Lein, A. Bjørgum, J.H. Nordlien, Y. Yu, K. Nisancioglu, Effect of low copper content and heat treatment on intergranular corrosion of model AlMgSi alloys, *Corrosion Science,* 48 (**2006**) 226-242.

[8] S.K. Kairy, T. Alam, P.A. Rometsch, C.H.J. Davies, R. Banerjee, N. Birbilis, Understanding the origins of intergranular corrosion in copper-containing Al-Mg-Si alloys, *Metallurgical and Materials Transactions A,* 47a (**2016**) 985-989.

[9] M.H. Larsen, J.C. Walmsley, O. Lunder, R.H. Mathiesen, K. Nisancioglu, Intergranular Corrosion of Copper-Containing AA6x xx AlMgSi Aluminum Alloys, *Journal of the Electrochemical Society,* 155 (**2008**) C550-C556.

[10] M.H. Larsen, J.C. Walmsley, O. Lunder, K. Nisancioglu, Effect of excess silicon and small copper content on intergranular corrosion of 6000-series aluminum alloys, *Journal of the Electrochemical Society,* 157 (**2010**) C61-C68.

[11] S.K. Kairy, P.A. Rometsch, C.H.J. Davies, N. Birbilis, On the intergranular corrosion and hardness evolution of 6xxx series Al alloys as a function of Si:Mg ratio, Cu content, and aging condition, *Corrosion Science,* 73 (**2017**) 1280-1295.

[12] W.J. Liang, P.A. Rometsch, L.F. Cao, N. Birbilis, General aspects related to the corrosion of 6xxx series aluminium alloys: Exploring the influence of Mg/Si ratio and Cu, *Corrosion Science,* 76 (**2013**) 119-128.

[13] T. Minoda, H. Yoshida, Effect of grain boundary characteristics on intergranular corrosion resistance of 6061 aluminum alloy extrusion, *Metallurgical and Materials Transactions A,* 33 (**2002**) 2891-2898.

[14] M.H. Larsen, Effect of composition and thermomechanical processing on the Intergranular corrosion of AA6000 aluminium alloys, *NTNU PhD Thesis,* (**2010**).

[15] S.P. Knight, M. Salagaras, A.M. Wythe, F. De Carlo, A.J. Davenport, A.R. Trueman, In situ X-ray tomography of intergranular corrosion of 2024 and 7050 aluminium alloys, *Corrosion Science,* 52 (**2010**) 3855-3860.

[16] S.P. Knight, M. Salagaras, A.R. Trueman, The study of intergranular corrosion in aircraft aluminium alloys using X-ray tomography, *Corrosion Science,* 53 (**2011**) 727-734.

[17] M.L.C. Lim, J.R. Scully, R.G. Kelly, Intergranular corrosion penetration in an Al-Mg alloy as a function of electrochemical and metallurgical conditions, *Corrosion Science,* 69 (**2012**) 35-47.

[18] W.L. Zhang, G.S. Frankel, Localized corrosion growth kinetics in AA2024 alloys, *Journal of the Electrochemical Society,* 149 (**2002**) B510-B519.

[19] A.M. Glenn, T.H. Muster, C. Luo, X. Zhou, G.E. Thompson, A. Boag, A.E. Hughes, Corrosion of AA2024-T3 part III: propagation, *Corrosion Science,* 53 (**2011**) 40-50.

[20] S. Jain, J.L. Hudson, J.R. Scully, Effects of constituent particles and sensitization on surface spreading of intergranular corrosion on a sensitized AA5083 alloy, *Electrochimica Acta,* 108 (**2013**) 253-264.

[21] S. Jain, M.L.C. Lim, J.L. Hudson, J.R. Scully, Spreading of intergranular corrosion on the surface of sensitized Al-4.4 Mg alloys: A general finding, *Corrosion Science,* 59 (**2012**) 136-147.

[22] A.M. Khorasani, I. Gibson, M. Goldberg, E.H. Doeven, G. Littlefair, Investigation on the effect of cutting fluid pressure on surface quality measurement in high speed thread milling of brass alloy (C3600) and aluminium alloy (5083), *Measurement,* 82 (**2016**) 55-63.

[23] S. Zhao, D.A. Wolfe, T.S. Huang, G.S. Frankel, Generalized model for IGC growth in aluminum alloys, *Journal of Statistical Planning and Inference,* 137 (**2007**) 2405-2412.

Chapter 6 Effect of GB microstructure on IGC

Abstract

The cause of higher susceptibility of the surface grains to IGC compared to the bulk grains, as reported in the previous chapter, was related to higher misorientation of the surface GBs than the bulk GBs. This gave higher and more continuous precipitation of Cu along the high angle (HAGB) than the low angle boundaries (LAGB), resulting in a higher resistance of the bulk LAGBs to IGC than the HAGBs near the surface.

6.1 Introduction

As reviewed in earlier chapters, alloy AA6005 can become susceptible to IGC when a nearly continuous Cu-rich film of nanometric thickness is formed along the GB in the underaged temper T4 [1]. It becomes resistant to IGC when the film is coarsened due to artificial aging to the maximum hardness T6 temper [1]. This behaviour is very much dependent on the details of the thermomechanical processing. While the earlier samples were treated according to the regulation for the T6 standard (i.e., including the steps of solution heat treatment (homogenization) of the extruded samples followed by the specified procedure of artificial aging), the samples in this work are artificially aged to the maximum hardness obtainable (T5 condition), without the solution heat treatment step. This temper coincided with the susceptible condition (as shown in chapter 4) requiring precipitation of the nearly continuous Cu film along the grain boundaries.

In other Al alloys (such as the 5xxx series alloy Al-7.14% Mg and 7xxx series alloy Al - 5.9% Zn - 2.9% Mg by weight), nucleation and growth of grain-boundary precipitates are shown to be strongly affected by the misorientation degree of the boundary [2, 3]. Furthermore, low angle boundaries (LAGBs) (<15°) are more resistant to IGC than high angle grain boundaries (HAGBs) in alloys, such as AA5182 (Al - 4.5% Mg), AA5083 (Al - 4.4% Mg - 0.5% Mn), AA6061 (Al - 0.54% Si - 0.23% Fe - 0.33% Cu - 1.03% Mg), AA7021 (5.0 to 6.0% Zn - 1.2 to 1.8% Mg - 0.4% Fe - 0.25% Cu - 0.25% Si), and AA7046 (6.6 to 7.6% Zn - 1.0 to 1.6% Mg, 0.4% Fe - 0.25% Cu - 0.20% Si)], depending on the degree of misorientation and the type and morphology of precipitate formation [4-9].

The GB misorientation is claimed to affect the formation of GB precipitates and PFZs [9]. The precipitates along the low angle grain boundaries of alloy (Al - 0.65% Mg - 0.93% Si - 0.40% Cu - 0.20% Fe - 0.56% Mn) were shown to be finer and denser than the precipitates along the high angle grain boundaries [10]. Recently, however, Kairy et al. claimed that the microchemistry change along GBs is more important for IGC than the GB misorientation. It was shown that the behaviour of GB precipitates is the dominant factor in determining the susceptibility to IGC [11].

In earlier work the extent of IGC attack on alloy 6005-T5 was restricted to a depth of about 200-300 μm from the surface [12]. We showed in chapter 5 that, after removing 400 μm thick of metal from the surface (corresponding to the layer with larger grains) samples of similar alloy became less susceptible to IGC as compared to the samples retaining their larger grain layers. The result indicates that GB properties at the surface and bulk of the alloy are different. Therefore, the objective of this chapter is to investigate the differences in the grain microstructure and microchemistry between near the surface and the bulk further and see how this factor correlates with IGC behaviour.

6.2 Experimental

6.2.1 Materials

The material focus was on AA6005 extruded Al alloy, and a detailed description of this is given chapter 3 section 3.2.1. Details about surface preparation, type of pretreatments used and corrosion testing are given in section 5.2.1 and 5.2.2.

6.2.2 SEM, EBSD and TEM characterization

Experimental details for SEM and EBSD characterization are discussed in sections 4.2.4. and 5.2.4, respectively. EBSD grain orientation maps and misorientation profiles were obtained by use of OIM analysis 7 software. The details for TEM characterization are given in section 3.2.3.

6.3 Results

6.3.1 SEM analysis

Plan view SEM images of the as pretreated surfaces (15 µm, 400 µm alkaline etched and 400 µm milled) are shown in Fig. 6.1a, c and e, respectively, to complement the cross-sectional images (Fig. 5.2, Fig. D4 and Fig. 5.6, respectively) in chapter 5 and appendix D. Distribution of the α-phase on the three surfaces are identical. However, the grain size is smaller on the 15 µm etched surface (about 20-60 µm; Fig. 6.1a) than the 400 µm etched surface (about 100 µm; Fig. 6.1c). Fig. 6.1b indicates significant IGC attack on the 15 µm etched surface after 24 h immersion in the test solution. However, the 400 µm etched (Fig. 6.1d) and milled (Fig. 6.1f) surfaces show that only the intermetallic α-phases were corroded away in 400 µm milled surface, and slight IGC attack occurred on 400 µm etched surface.

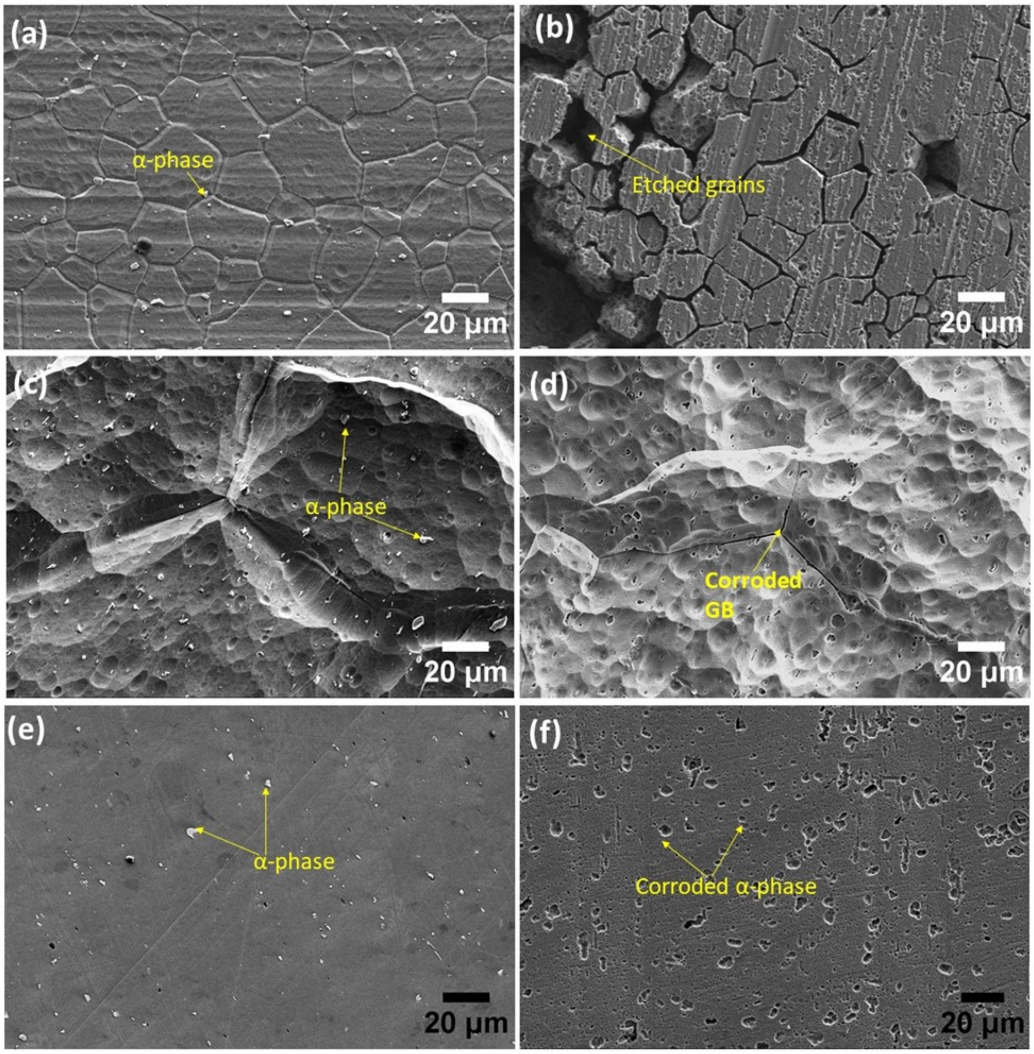

Fig. 6.1 Secondary electron image of (a) Alkaline etched surface (15 µm removed layer). (b) 24 h corroded surface on alkaline etched surface. (c) 400 µm alkaline etched surface (d) 24 h corroded alkaline etched surface. (e) 400 µm milled surface (f) 24 h corroded on 400 µm milled surface.

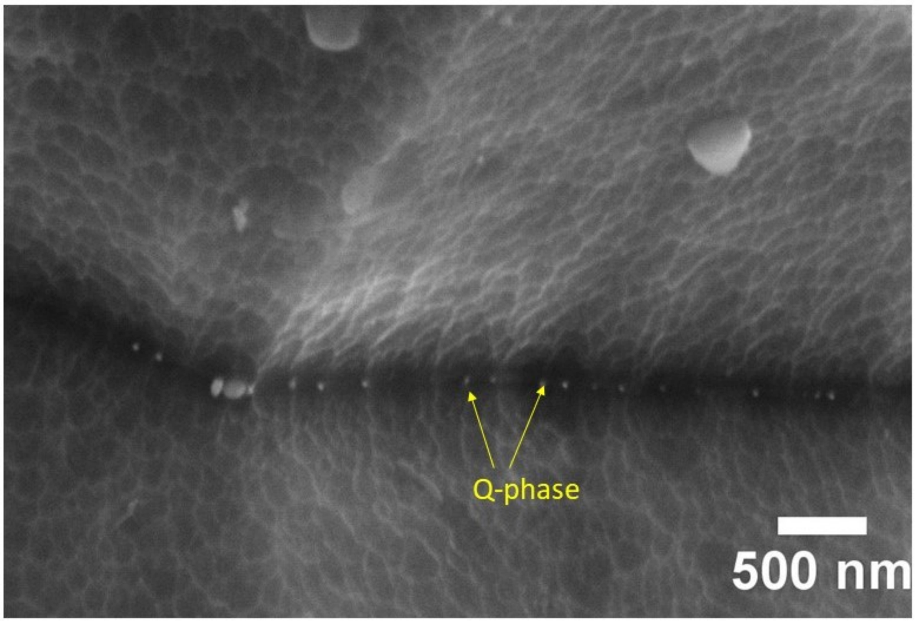

Fig. 6.2 Q-phase distribution on 400 µm alkaline etched surface.

Fig. 6.2 shows the typical distribution of the Q-phase along a grain boundary on 400 µm alkaline etched surface, representing the bulk morphology. In comparison to the 15 µm etched surface shown in Fig. 3.6, which represents the surface morphology, the Q-phase particles in the bulk are smaller and more closely spaced.

6.3.2 EBSD analysis

Fig. 6.3 shows cross-sectional EBSD analyses of 15 µm etched sample. It shows that the top layers of about 200-300 µm are dominated by high angle boundaries. It also shows that a very top layer consisting of small grains of size about 20-60 µm exists, verifying the smaller grain size of 15 µm etched surface in Fig. 6.1a is smaller than that for 400 µm etched surface in Fig. 6.1c. Coarse grains (around 100-200 µm), which are perpendicular to the extrusion direction; mostly have grain orientation either {101} or {111} plane while the grains which are parallel to the extrusion direction mostly have grain orientation of {001} plane.

Fig. 6.4 shows plan view of as-received surface (sample preparation for EBSD analysis is discussed in section 5.2.4). Fig. 6.4a also confirms that the top layer consists of very small grains and mostly dominated by high angle grain boundaries. Fig. 6.4b confirms that grains that are perpendicular to extrusion direction have either {101} or {111} plane grain orientation.

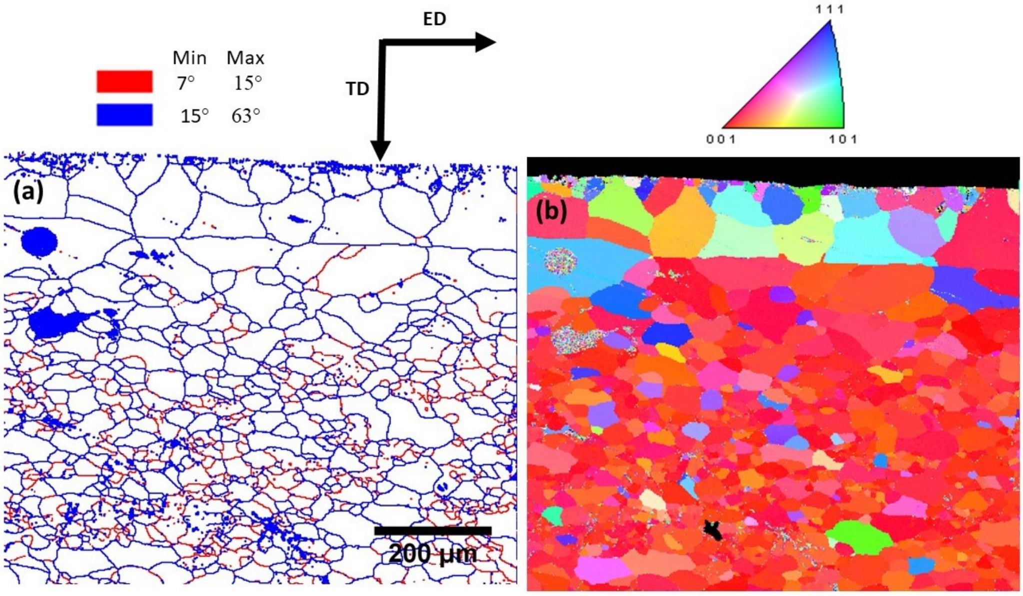

Fig. 6.3 EBSD maps of cross-section sample of alkaline etched sample (15 µm etched layer) (a) Misorientation distribution map along with colour coded misorientation angles. (b) Grain orientation map of the image (a) along with the colour key.

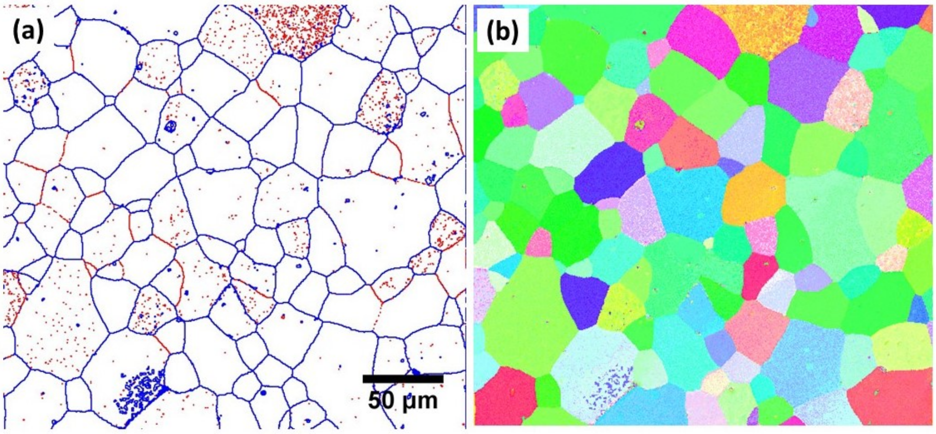

Fig. 6.4 EBSD maps of a plan view of the as-received sample (polished for EBSD analysis) (a) Misorientation distribution map (b) Grain orientation map of the image (a), colour codes are similar to Fig. 6.3.

6.3.3 STEM analysis

The bulk grain boundaries were decorated by discrete Q-phase particles, as shown in the STEM-EDS map in Fig. 6.5. This result is similar to that shown by the SEM results reported above in Fig. 6.2. Contrary to the grain boundary analysis of the large-grain layers near the surface (Fig. 3.8), discussed in chapter 3, no continuous Cu film could be detected in the bulk. The width of PFZs adjacent to LAGBs (at the bulk) is smaller (around 50 nm) as compared to HAGBs [around 100 nm (Fig. 3.8)] that is at the surface.

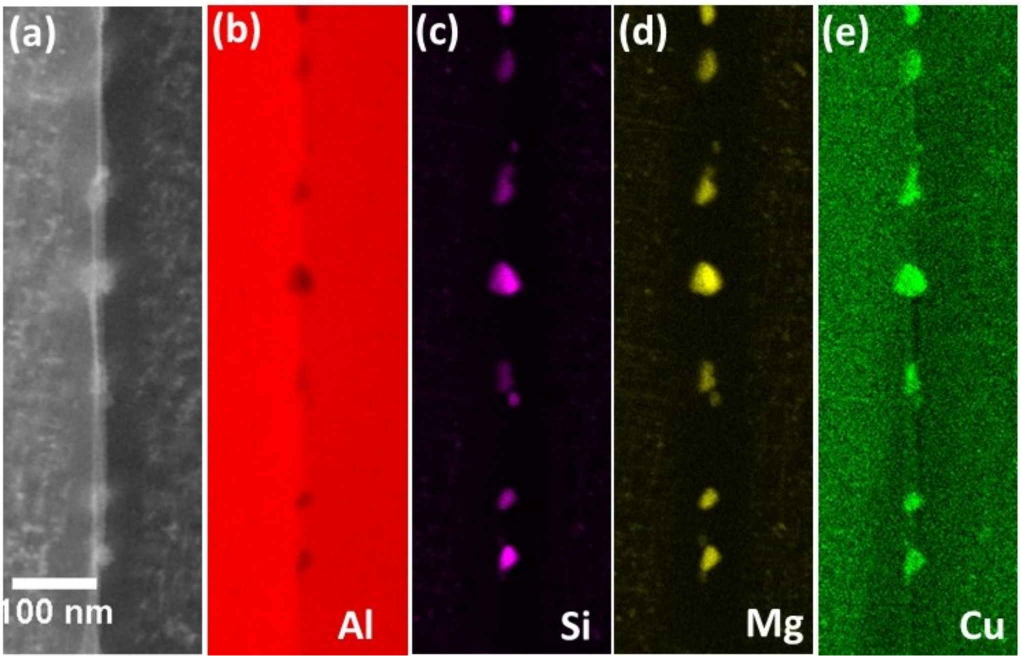

Fig. 6.5 (a) STEM image showing Q-phase along grain boundary in 400 µm milled sample. EDS maps of the elements (b) Al, (c) Si, (d) Mg, (e) Cu.

6.4 Discussion

The analytical results in this chapter complement the results about the grain and GB geometry in chapter 5, in which the larger grain geometry with certain order (elongated perpendicular to the extrusion direction) was shown to enhance faster IGC propagation than the smaller bulk grains giving longer and more tortuous propagation paths. The GBs between larger surface grains were shown in this chapter to have higher misorientation than the smaller bulk grains, which is supposed to favour easier solute precipitation and formation of wider PFZs along the larger grains than that for the smaller bulk grains. As documented further by STEM, this favours, in turn, precipitation of more continuous Cu film and wider PFZ along the film along the near-surface HAGB than for the bulk LAGB. The additional factor of Cu enrichment by dealloying both in the IGC fissure tails and the outer surface exposed to the acidified chloride solution, described in detail in chapter 4, the geometrical factors described in chapter 5, along with the GB nanostructure and composition described in the present chapter thus give a more complete physicochemical model for IGC propagation. The model will be summarized in more detail in chapter 7.

6.5 Conclusions

1. High angle GBs near the surface were more susceptible to IGC than the low angle GBs in the bulk.

2. Segregation of Cu film was more favoured along the near surface GBs than the bulk GBs.

3. The width of PFZs along LAGBs (in the bulk) was smaller than HAGBs near the surface.

4. As a result of the above findings, the large grains near the surface were more susceptible to IGC than the smaller grains in the bulk.

6.6 References

[1] G. Svenningsen, M.H. Larsen, J.C. Walmsley, J.H. Nordlien, K. Nisancioglu, Effect of artificial aging on intergranular corrosion of extruded AlMgSi alloy with small Cu content, *Corrosion Science,* 48 (**2006**) 1528-1543.

[2] P.N.T. Unwin, R.B. Nicholson, The nucleation and initial stages of growth of grain boundary precipitates in Al-Zn-Mg and Al-Mg alloys, *Acta metallurgica,* 17 (**1969**) 1379-1393.

[3] L.I. Kaigorodova, The effect of grain-boundary structure formation on β-precipitation in aged Al-Mg alloys, *Materials Science Forum,* 294 (**1999**) 477-480.

[4] A.J. Davenport, Y. Yuan, R. Ambat, B.J. Connolly, M. Strangwood, A. Afseth, G.M. Scamans, Intergranular corrosion and stress corrosion cracking of sensitised AA5182, *Materials Science Forum,* 519-521 (**2006**) 641-646.

[5] R. Zhang, R.K. Gupta, C.H.J. Davies, A.M. Hodge, M. Tort, K. Xia, N. Birbilis, The influence of grain size and grain orientation on sensitization in AA5083, *Corrosion Science,* 72 (**2015**) 160-168.

[6] H. Yukawa, Y. Murata, M. Morinaga, Y. Takahashi, H. Yoshida, Heterogeneous distributions of magnesium atoms near the precipitate in Al-Mg based alloys, *Acta Metallurgica et Materialia,* 43 (**1995**) 681-688.

[7] J. Yan, N.M. Heckman, L. Velasco, A.M. Hodge, Improve sensitization and corrosion resistance of an Al-Mg alloy by optimization of grain boundaries, *Scientific Reports,* 6 (**2016**) 26870.

[8] A. Cassell, G.E. Thompson, X.R. Zhou, T. Hashimoto, G. Scamans, Relating grain misorientation to the corrosion behaviour of low copper 7xxx aluminium alloys, *Materials Science Forum,* 765 (**2013**) 623-628.

[9] T. Minoda, H. Yoshida, Effect of grain boundary characteristics on intergranular corrosion resistance of 6061 aluminum alloy extrusion, *Metallurgical and Materials Transactions A,* 33 (**2002**) 2891-2898.

[10] J. Holmestad, M. Ervik, C.D. Marioara, J.C. Walmsley, Investigation of grain boundaries in an Al-Mg-Si-Cu alloy, *Materials Science Forum,* 794 (**2014**) 951-956.

[11] S.K. Kairy, S. Turk, N. Birbilis, A. Shekhter, The role of microstructure and microchemistry on intergranular corrosion of aluminium alloy AA7085-T7452, *Corrosion Science,* (**2018**).

[12] M.H. Larsen, Effect of composition and thermomechanical processing on the Intergranular corrosion of AA6000 aluminium alloys, *NTNU PhD Thesis,* (**2010**).

Chapter 7 Discussion

This chapter aims to discuss significance of the results, mechanism for initiation and propagation of IGC in AA6005 alloys and some suggestions for future work for further improvement of the experimental approach and understanding of the mechanisms.

7.1 Electrochemical mechanism

As discussed in section 2.5, both the initiation and propagation mechanisms of IGC in alloy AA6005 were uncertain. The first uncertainty was related to the nature of the cathodes, since the α-phase was shown in earlier work [1] to become attacked by the acidified chloride solution. Furthermore, the removal of these phases by chemical treatment of the surface reduced the width of the IGC fissures in a separate study [2], but it did not reduce the depth of attack. As a result of such findings, the initiation of IGC was attributed to the α-phase particles at the GBs, before they were consumed by the aggressive test solution. However, the propagation stage was suggested to occur with the internal cathodes as the driving force, represented mainly by the Cu-rich nanofilm along the susceptible GBs, while the adjacent solute depleted zone or PFZ was the active anode [2-8].

The present study showed for the first time that the as-extruded surface was protected by an oxide layer, consisting of a mixture of γ-Al_2O_3, $MgAl_2O_4$ and SiO_2, which was formed during the extrusion process. In addition, the Al matrix appeared to be smeared over the surface, covering a significant cathodic area provided by the intermetallic phases. Such a layer is expected to be quite stable when exposed to normal atmospheric exposure. Under the severe conditions provided by the acidified chloride solution in this work, this layer delayed corrosion initiation for a limited period. This period is expected to last much longer under more benign atmospheric conditions. Removal of the layer by etching, mechanical polishing, or Ar-sputtering reduced the induction time for IGC initiation significantly.

The present work questioned the adequacy of the internal cathode as the driving force since the nanofilm appearing at the fissure tip is probably immediately detached by the propagating fissure, thereby becoming ineffective as the local cathode as it lost contact with the metal at the GB. With reference to the literature [3-5], the Q-phase alone did not appear to act as an effective cathode. Moreover, if both the oxidation (of aluminium followed by hydration) and reduction (mainly hydrogen evolution) reactions occur at the same location (fissure tip), they would not be able to maintain the low pH required because of neutralization of the solution by the two simultaneous reactions. The results of section 4.3.1 based on the differences in the internal and external corrosion morphology, indicated that the pH at the reaction site was likely more acidic than the test solution in the bulk. This would require in turn an increase in the Cl^- concentration in the fissure to satisfy the electro neutrality condition, according to the well-accepted electrochemical theory of localized corrosion in chloride media [9-11].

The discovery of Cu segregation along the corroded fissure walls and the external surface exposed to the acidified chloride solution was thus an important result, indicating the continual creation of internal and external cathodic areas by dealloying during the propagation phase. It is believed that the new cathodes will be able to sustain the IGC attack. These results showed, moreover, that the rules of geometrical separation of the anodes (fissure tip) and cathodes (fissure tail and an external surface with increasing Cu enrichment) in order to maintain the necessary difference of anolyte and catholyte chemistry (lower pH and higher Cl^- concentration for the anolyte) were satisfied. Fig. 7.1 shows schematically the IGC mechanism discussed above and as modified from the earlier studies [5].

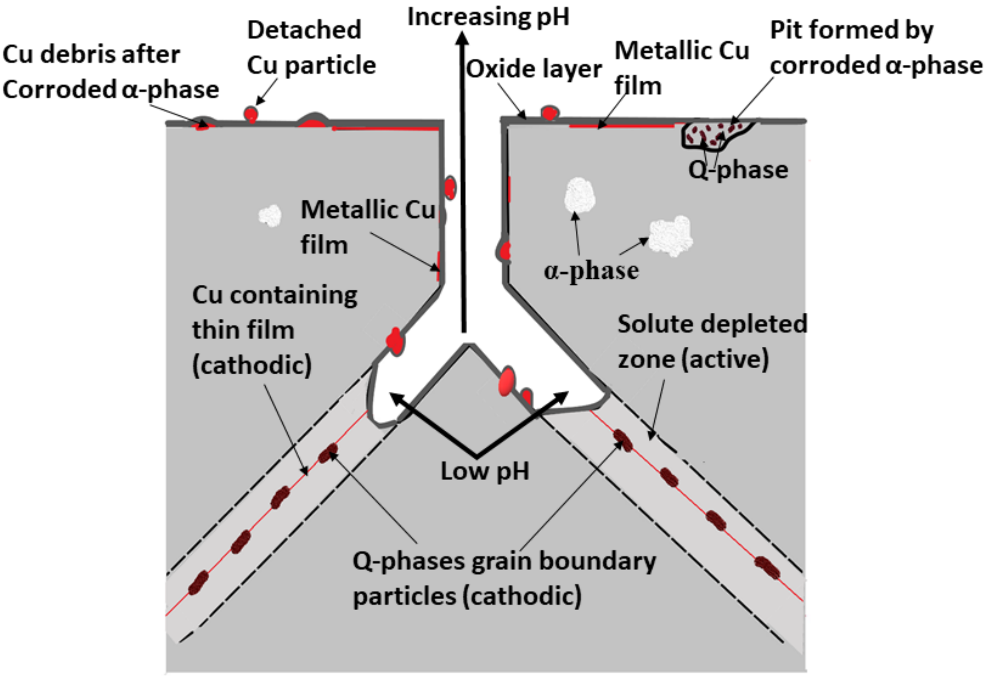

Fig. 7.1 Conceptual sketch of IGC mechanism on the AA6005 alloy. The dimensions shown are not representative of the actual IGC process. They are exaggerated for illustrating the discussion in the text.

7.2 Effect of grain structure and grain boundary characteristics

As discussed in chapter 5, IGC on alloy AA6005 was related to grain size and structure and concluded that the surface microstructure is susceptible, while the bulk microstructure slows down the rate of propagation significantly. The near surface structure was classified into three layers, as shown in Fig. 7.2. A discussion of how these layers may have formed during extrusion is outside the present scope. The first layer, which consists of small grains of about 10 µm in average, was probably highly deformed and smeared over the surface, as discussed in section 3.3.1. partly covering the cathodic primary particles on the surface. It also supported the protective crystalline mixed-oxide film at the outermost surface, as discussed in section 3.3.2. The layer was responsible for the initiation and early propagation of the IGC at the surface. Its presence delayed initiation on the as-received surface because of the protective factors mentioned. Its removal reduced the induction time for propagation independent of the removal methods used (alkaline etching, mechanical polishing and Ar-sputtering). Layers 2 and 3 consisted of large recrystallized grains elongated perpendicular and parallel to the extrusion direction, respectively. IGC propagated along relatively straight GBs of these two layers quite rapidly in their respective favoured directions of elongation. Thus, the fissures propagated in depth relative to the exposed surface in layer 2. They were arrested by GBs of layer 3, which blocked the GBs of layer 2, however, at the same time enhancing their rapid growth laterally with respect to the surface in layer 3. While IGC spread along the surface in this manner, its propagation into the bulk layer (layer 4) was restricted. The propagation rate was furthermore slower in the bulk layer because of the smaller size and irregular shape of the grains in relation to the surface layers, which increased the tortuosity of the GBs.

In addition to the foregoing factors, the IGC-susceptible surface grains were dominated by high angle grain boundaries, which is supposed to facilitate segregation of Cu film, while the bulk grains were dominated by low angle grain boundaries, which did not allow the formation of the Cu-film (as shown in Fig. 6.5). This is another factor to consider in explaining the difference in the susceptibility of the surface layers to IGC. While IGC fissures seem to propagate with relative ease along the film-like Cu segregation along the GB, their propagation was hindered in the absence of the Cu film [7]. The coarsened Cu particles act as temporary barriers to fissure propagation. However, the fissures appear to be able to continue propagating by going around or corroding the particles on their path [12].

Another factor slowing IGC propagation must be ohmic potential drop developing in the fissures with increasing depth of penetration, decreasing conductivity of the electrolyte with increasing concentration of salt due to ionic association, precipitation of aluminium oxides and salt-film formation, and increasing density of hydrogen bubbles becoming trapped in an increasingly jelly-like electrolyte. These may become important factors slowing the rate of fissure growth and limiting the propagation depth to about 400 µm in the present test solution, combined with the factors discussed above. Existence of such factors may further be supported by the fact that 400 µm limit applied to all types of surfaces investigated, including the one with the 400 µm – milled surface (see, Fig. 5.6 and related text) if the corrosion test were continued long enough to reach the limiting penetration depth. This is an unexpected finding, which requires further investigation.

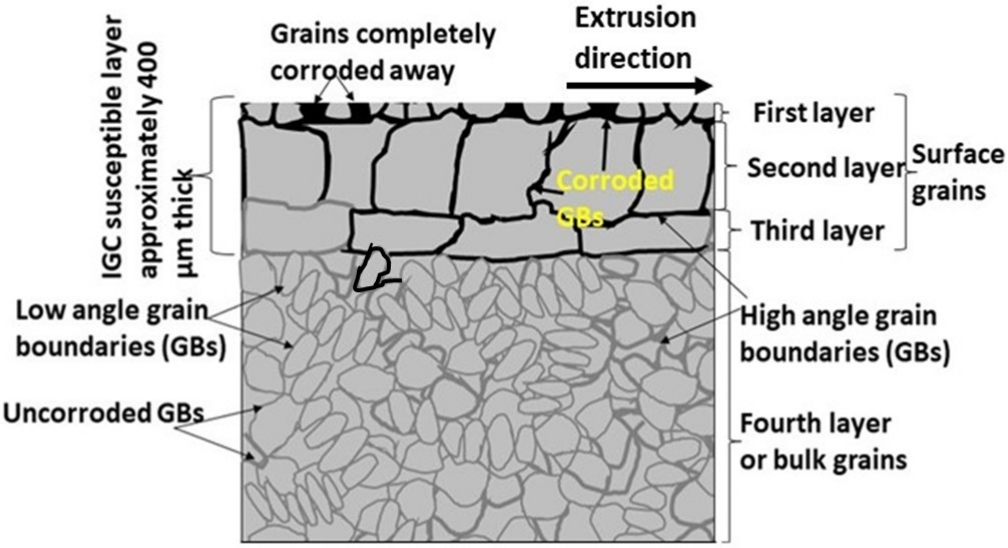

Fig. 7.2 Schematic illustration of the cross-section microstructure of extruded AA6005 alloy corroded for 24 h.

7.3 Practical significance

The present corrosion results apply to an extremely accelerated test for qualifying Al alloys for automotive applications. However, the as-received surface has a quite protective thermally formed oxide, which is required to be removed by alkaline etching in the standard, which this work has shown to accelerate the corrosion process even further. The material may thus be sufficiently resistant to IGC under realistic atmospheric exposure. Furthermore, the results indicate that propagation of IGC beyond 400 µm on alloy AA6005 is a result of the aggressiveness of the test solution rather than susceptibility to IGC. If the construction component of the alloy is significantly thicker than this limit, its failure due to IGC should not be likely in more benign atmospheric environments in practice [6]. As has been shown in earlier work [5], the susceptible surface layers can also be made resistant to IGC by modifying the heat treatment as long as it does not significantly reduce the mechanical properties of the material.

7.4 Suggestions for future work

The availability of information about the electrochemical properties of α and Q phases in the literature is limited to solutions of neutral and alkaline pH [13-15]. The absence of information for acidic chloride solutions has been an important drawback throughout this work. It should be investigated more extensively in a dedicated study to understand the anodic and cathodic behaviour of these phases and the effect of time-dependent changes in the behaviour, due to their self-corrosion, for a more complete understanding of the IGC mechanism in chloride media. Procedures for synthesizing these phases from their pure components are available [14, 15]. Similarly, the electrochemical behaviour of relevant Al solid-solution phase of the AA6005 alloy should also be investigated. The electrochemical study has to be combined with advanced surface-analytical techniques for characterizing the modification of the surface structure and composition as a function of time of immersion. It has been shown elsewhere [16] how the solid-solution alloy, clean from the more noble primary precipitates, can be prepared.

The present and previous studies [3-6] have indicated how the GB structure and composition can be altered by thermomechanical processing to obtain GBs, which are immune to IGC. The work so far has not been able to cover a sufficient number of thermomechanical parameters to understand how different steps of heat treatment and mechanical processing and their combinations modify the GB properties. Such investigations, organized to develop methods for synthesizing tailor-made GB nanostructures and chemistry, are needed to obtain a more complete picture of the mechanism of IGC and the conditions, which give the GBs immunity to IGC in different Al alloys.

7.5 References

[1] K. Shimizu, K. Nisancioglu, High resolution SEM investigation of intercrystalline corrosion on 6000-Series aluminum alloy with low copper content, *ECS Electrochemistry Letters,* 3 (**2014**) C29-C31.

[2] M.H. Larsen, J.C. Walmsley, O. Lunder, K. Nisancioglu, Effect of excess silicon and small copper content on intergranular corrosion of 6000-series aluminum alloys, *Journal of the Electrochemical Society,* 157 (**2010**) C61-C68.

[3] G. Svenningsen, M.H. Larsen, J.H. Nordlien, K. Nisancioglu, Effect of high temperature heat treatment on intergranular corrosion of AlMgSi(Cu) model alloy, *Corrosion Science,* 48 (**2006**) 258-272.

[4] G. Svenningsen, M.H. Larsen, J.H. Nordlien, K. Nisancioglu, Effect of thermomechanical history on intergranular corrosion of extruded AlMgSi(Cu) model alloy, *Corrosion Science,* 48 (**2006**) 3969-3987.

[5] G. Svenningsen, M.H. Larsen, J.C. Walmsley, J.H. Nordlien, K. Nisancioglu, Effect of artificial aging on intergranular corrosion of extruded AlMgSi alloy with small Cu content, *Corrosion Science,* 48 (**2006**) 1528-1543.

[6] G. Svenningsen, J.E. Lein, A. Bjørgum, J.H. Nordlien, Y. Yu, K. Nisancioglu, Effect of low copper content and heat treatment on intergranular corrosion of model AlMgSi alloys, *Corrosion Science,* 48 (**2006**) 226-242.

[7] M.H. Larsen, J.C. Walmsley, O. Lunder, R.H. Mathiesen, K. Nisancioglu, Intergranular corrosion of copper-containing AA6xxx AlMgSi aluminum alloys, *Journal of the Electrochemical Society,* 155 (**2008**) C550-C556.

[8] S.K. Kairy, T. Alam, P.A. Rometsch, C.H.J. Davies, R. Banerjee, N. Birbilis, Understanding the origins of intergranular corrosion in copper-containing Al-Mg-Si alloys, *Metallurgical and Materials Transactions A,* 47a (**2016**) 985-989.

[9] K. Nisancioglu, Understanding Corrosion Mechanisms of Impure Aluminum and Related Phenomena, *Corrosion Science: Proceedings of the International Symposium,The Electrochemical Society*, 2002 (**2002**) 299.

[10] G.S. Frankel, Pitting corrosion of metals a review of the critical factors, *Journal of the Electrochemical Society,* 145 (**1998**) 2186-2198.

[11] G.S. Frankel, N. Sridhar, Understanding localized corrosion, *Materials Today,* 11 (**2008**) 38-44.

[12] M.H. Larsen, Effect of composition and thermomechanical processing on the Intergranular corrosion of AA6000 aluminium alloys, *NTNU PhD Thesis,* (**2010**).

[13] O. Lunder, C. Simensen, Y. Yu, K. Nisancioglu, Formation and characterisation of Ti–Zr based conversion layers on AA6060 aluminium, *Surface and Coatings Technology,* 184 (**2004**) 278-290.

[14] S.K. Kairy, P.A. Rometsch, C.H.J. Davies, N. Birbilis, On the electrochemical and quasi in situ corrosion response of the Q-Phase (AlxCuyMgzSiw) intermetallic particle in 6xxx series aluminum alloys, *Corrosion Science,* 73 (**2016**) 87-99.

[15] K. Nisancioglu, Electrochemical behavior of aluminum-base intermetallics containing iron, *Journal of the Electrochemical Society,* 137 (**1990**) 69-77.

[16] K.N. O. Lunder, Electrochemical and surface-structural aspects of the corrosion of aluminum alloys, *Proceedings of 8th International Light Metals Congress,* Leoben, Austria (**1987**) 710.

Chapter 8 Conclusions

Initiation and propagation mechanism of AA6005 alloy in various surface conditions has been studied using an accelerated corrosion test, and various characterization methods. After an overall discussion of the results, the following conclusions are reached.

- IGC initiated adjacent to the α-Al(Fe,Cu,Mn)Si particles for all types of surfaces (as-received, alkaline etching, polishing, and Ar-sputtering) and acted as external cathodes during initiation phase. However, these phases corrode rapidly in the acidified NaCl test solution. The Cu-rich remnants of the α-phase and Cu enrichment of the surface due to dealloying of the Al matrix alloy became significant as external cathodes after α-phase particles corroded away in the acidified NaCl test solution. In contrast, Q phase was inert during initiation of IGC, not affected by exposure to test solution. In addition, no sign of IGC was detected at the Q-phase particles. They rather acted as inert barriers against IGC filament initiation and propagation.

- The induction time of IGC initiation on the as-received surface was longer as compared to the pretreated surface and, this was related to the presence of the protective crystalline layer of around 8 nm thick mixed oxide consisting of γ-Al_2O_3, the spinel $AlMg_2O_4$ and SiO_2 on the as-received surface. Such a layer is expected to last much longer under normal atmospheric environment than in the accelerated test environment.

- At the outset, IGC propagation depended on the coupling between a few nm thick nearly continuous Cu film segregated along the GB and the solute depleted zone adjacent to it, as well as the α-phase particles as the external cathodes. Corrosion of these particles in the acid chloride test solution and dealloying at the surface and along the walls of the IGC fissures caused enrichment of fresh Cu in the form of patches of nanofilm and nanoparticles. These acted as cathodes during the propagation phase, more than making up for the cathode area lost by corrosion of the α-phase. Separation of the anodes at the tip of fissures and cathodic sites formed by Cu enrichment at the surface and fissure tails thus satisfied one of the basic requirement of the electrochemical theory of localized corrosion.

- The difference in the morphology of the corroding external surface (uniform etching and formation of micropits) exposed to the bulk solution and crystallographically etched morphology of the fissure walls suggested indirectly that pH was lower in the filaments than that on the surface, satisfying another requirement of the electrochemical theory of localized corrosion.

- Coarse surface grains were mostly dominated by high-angle grain boundaries (HAGBs), which were more susceptible to IGC than the bulk grains, which were dominated by low-angle grain boundaries (LAGBs). HAGB appear to be more susceptible to segregation of a nearly continuous Cu film than LAGB. This contributed to the higher IGC resistance of the bulk GBs (LAGBs) in relation to the surface GBs (HAGBs).

- Propagation of IGC fissures along longer and straighter grain boundaries around larger grains was faster than that along tortuous boundaries around smaller irregularly-shaped grains. Grains elongated along the direction of fissure growth enhanced, while grains elongated perpendicular to the direction of growth restricted IGC propagation. Propagation of IGC was perpendicular to the extruded surface in the beginning, following GBs of coarse surface grains elongated perpendicular to the exposed surface (extrusion direction). In the next layer, the grain boundaries were elongated parallel to the extruded surface, which caused lateral spreading of the IGC. This phenomenon contributed to delaying the in-depth penetration of the fissures into the bulk of the material.

- This work has shown that IGC resistance of alloy AA6005, and possibly also other 6xxx series alloys can be optimized by slight changes in the thermomechanical properties to obtain the desirable changes in the GB nanostructure and chemistry, GB size, geometry, the surface microstructure and also maintaining the protective oxide formed during extrusion.

Appendix A FIB sample preparation for TEM

This appendix describes the method of preparing TEM samples for the study of surface oxide and oxide/alloy interface by the FIB lift-out technique.

TEM samples were prepared by FEI Helios G4 UX dual beam (electron and ion beam) FIB/SEM system, equipped with a gallium ion source operating in the accelerating voltage range 0.5-30 keV and an omniprobe micromanipulator. This appendix summarizes the FIB sample preparation steps used in this work. More detailed information can be found in reference [1].

The area of interest was first coated by a C shield for protection against ion-beam milling. Gaseous carbon (C) was introduced into the vacuum chamber through a thin needle brought very close to the sample surface and coated by use of both electron and ion beam, in the present case Ga. Either ion or electron beam can be used for deposition in FIB. Ions or electrons collide with the gas molecules and sputter out the target atoms, which are then deposited to the sample surface. When using ions, Ga may be deposited together with C, contaminating the surface of the sample. To avoid this, C layer of around 0.05-0.1 μm was deposited first by using electron beam, and the rest of the desired thickness was deposited by ion beam [1], as shown in Fig. A1a. By using a large beam current for fast ion milling, two trenches were milled on either side of the carbon coating as shown in Fig. A1b. The sample was then lifted by omniprobe (not shown here) and mounted (with the help C) on a molybdenum grid (TEM sample holder shown in Fig. A1c). The layer was then polished using successive lower beam currents. Finally, the sample was thinned to 100 nm or less using 2 keV ion beam to minimize the artefacts from sample preparation. Cross-section of the final prepared sample is shown in Fig. A1d.

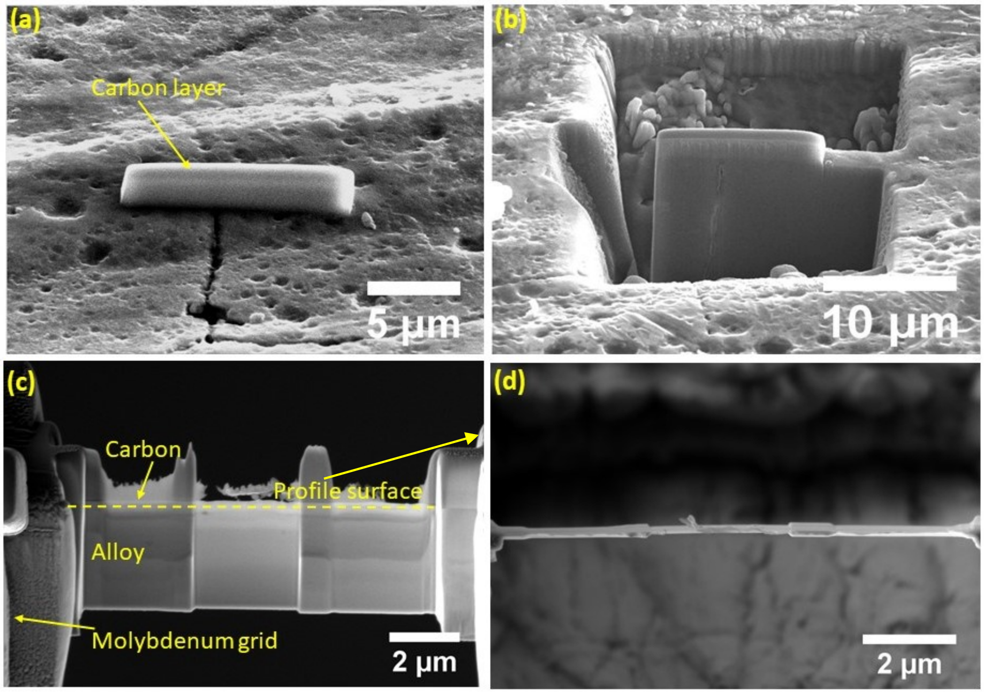

Fig. A1 FIB preparation of specimens for TEM. (a) Carbon mask deposited on 24 h corroded surface for protection against Ga ions. (b) Milling around the C mask to obtain the cross-sectional sample for liftout. (c) Specimen attached to a molybdenum grid for thinning to 100 nm. (d) Top view of the final cross-section which is about 100 nm thick.

Reference

[1] L. A. Giannuzzi, Introduction to focused ion beams: instrumentation, theory, technique and practice, *Springer*, New York, USA **(2004)**.

Appendix B Characterization of synthetic α-phase

Artificially grown α-phases available from earlier work [1] were tested for corrosion and electrochemical properties, in view of the absence of such data for this phase in acidified chloride solution. However, these samples did not contain any Cu and possibly not directly comparable to Cu-containing α-phase relevant to the present thesis.

The α-Al(Mn,Fe)Si phase crystals were prepared from the pure components by controlled solidification. A detailed description of preparation method is discussed in Ref. [1]. EDS analysis of the crystal marked as 1 in Fig. B1a is shown in Fig. B1b. The grown crystals were embedded in an Al matrix, as shown in Fig. B1a, which had to be masked in preparing the α-phase electrode for the electrochemical work, as described in Ref. [1].

B.1 Results

B.1.1 Corrosion

The morphology of the α-phase surface after 24 h corrosion in the acidified chloride test solution is shown in Fig. B2a and at a higher magnification in Fig. B2b. The phase is locally attacked in contrast to a uniform etching of the Cu-containing phase discussed in chapter 3. Fig. B2c shows the EDS analysis of corroded α-phase (Fig. B2a). No significant compositional difference was observed between the uncorroded (Fig. B1b) and corroded (Fig. B2c) α-phase by EDS analysis. The Mn concentration was slightly reduced in the corroded phase as compared to the uncorroded one.

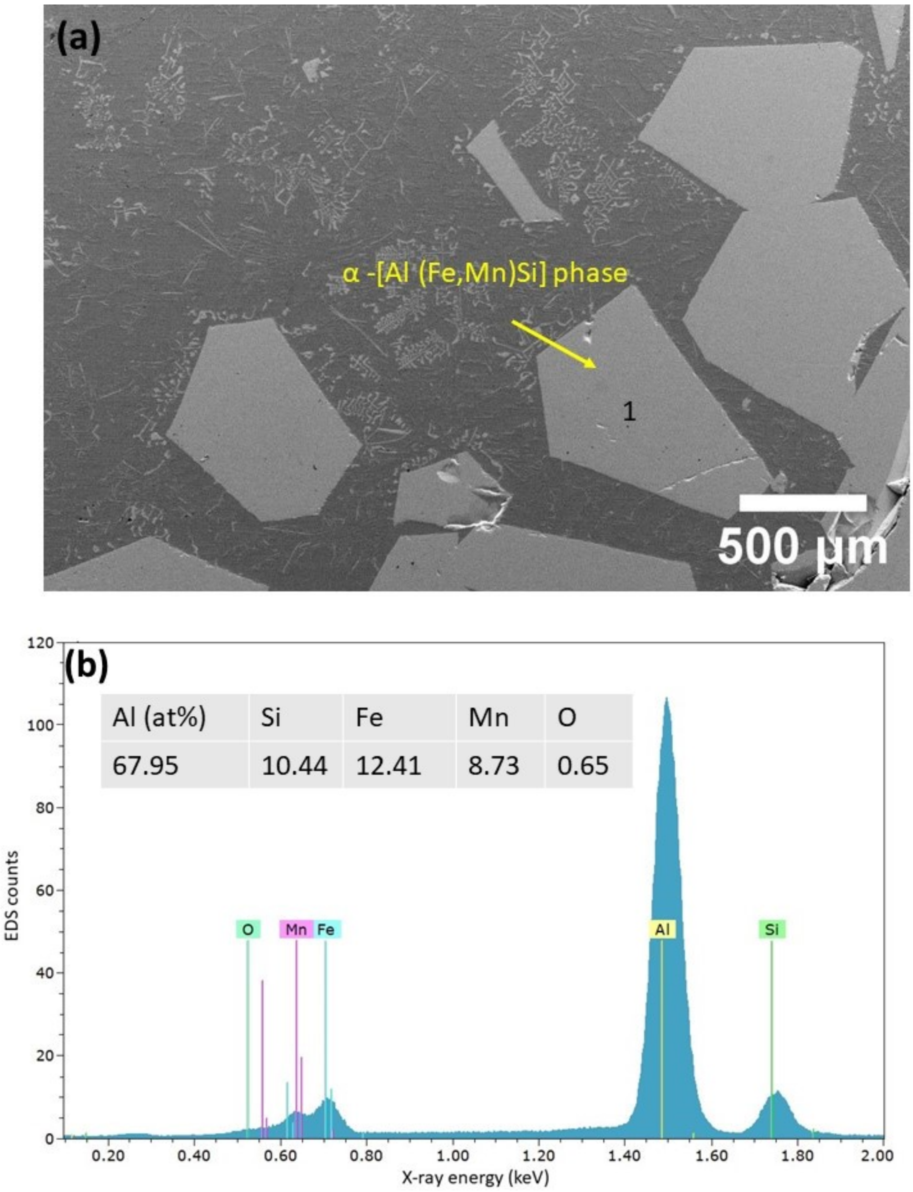

Al (at%)	Si	Fe	Mn	O
67.95	10.44	12.41	8.73	0.65

Fig. B1 (a) SEM image of synthesized α-Al(Fe,Mn)Si phase. (b) EDS analysis of α-Al(Fe,Mn)Si crystal marked as 1 in the image (a).

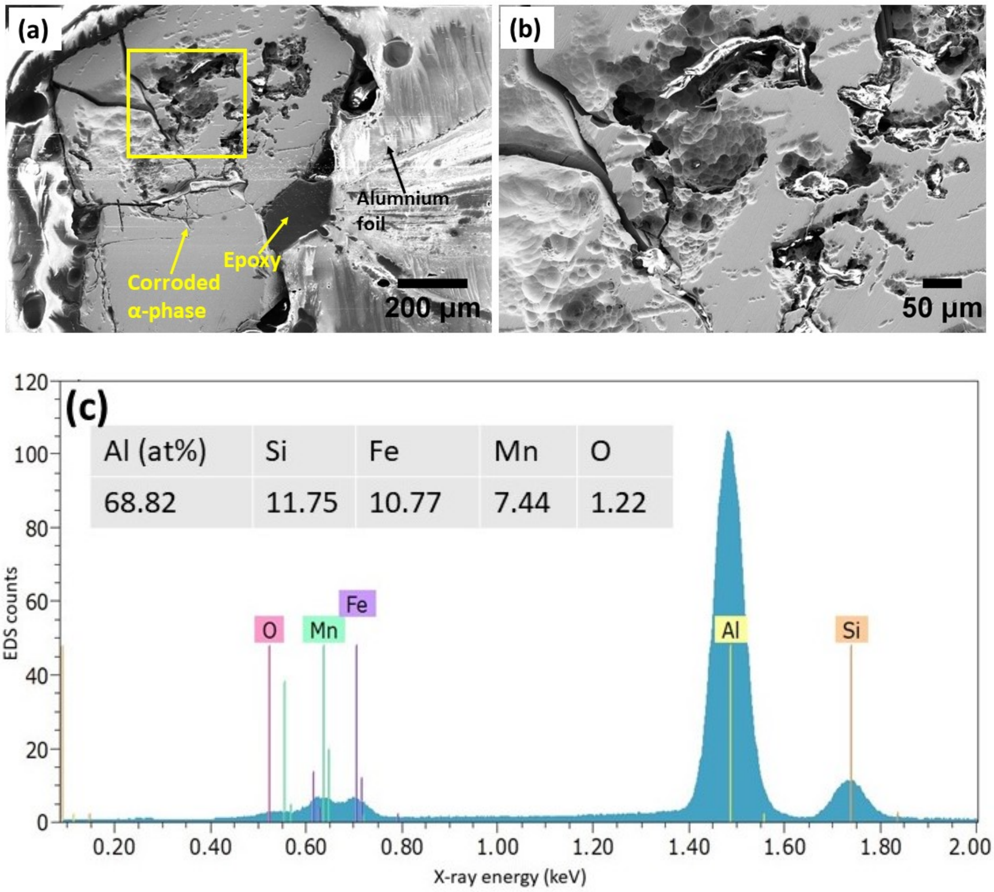

Al (at%)	Si	Fe	Mn	O
68.82	11.75	10.77	7.44	1.22

Fig. B2 (a) SEM image of 24 h corroded α-Al(Fe,Mn)Si phase. (b) Image of area marked with a yellow square in (a) at a higher magnification. (c) EDS analysis of α-Al(Fe,Mn)Si phase shown in image (a).

B.1.2 Electrochemical measurements

Fig. B3 shows the corrosion potential of α-Al(Fe,Mn)Si phase as a function of exposure time in acidified chloride solution. Potential decreased from -0.53 V to -0.63 V during the first 500 s of exposure, and then it stabilized at -0.635 V.

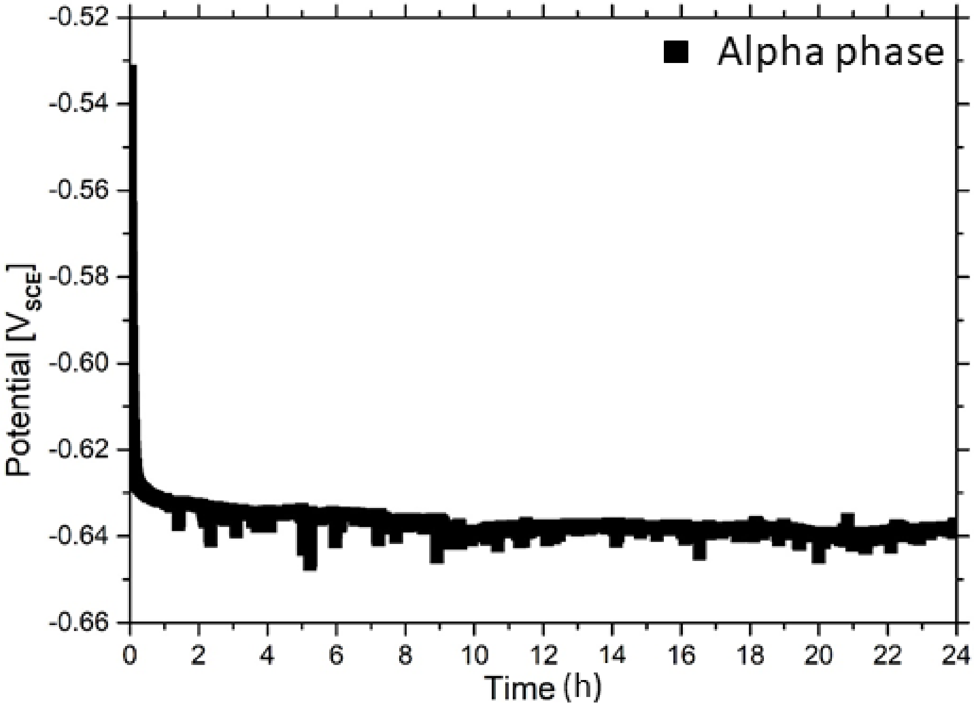

Fig. B3 Corrosion potential of synthetic α-Al(Fe,Mn)Si phase as a function of exposure time in acidified chloride solution.

Potentiodynamic polarization testing was performed in the negative potential direction starting from the open circuit potential in the acidified chloride solution as shown in Fig. B4. Comparison of the cathodic curve of the α-phase and AA6005 alloy indicates that the synthetic α-phase is significantly more noble than the AA6005 alloy.

It was shown in chapter 3 that the α-phase particles in AA6005 alloy corroded away after a certain time period in acidified chloride solution. In order to check the anodic behaviour of α-phase, potentiostatic polarization was performed at -0.735 V as shown in Fig. B5. The applied potential of -0.735 V was selected because it corresponds to the corrosion potential of AA6005 in acidified chloride solution. The current measured during potentiostatic polarization, as shown in Fig. B5 was cathodic.

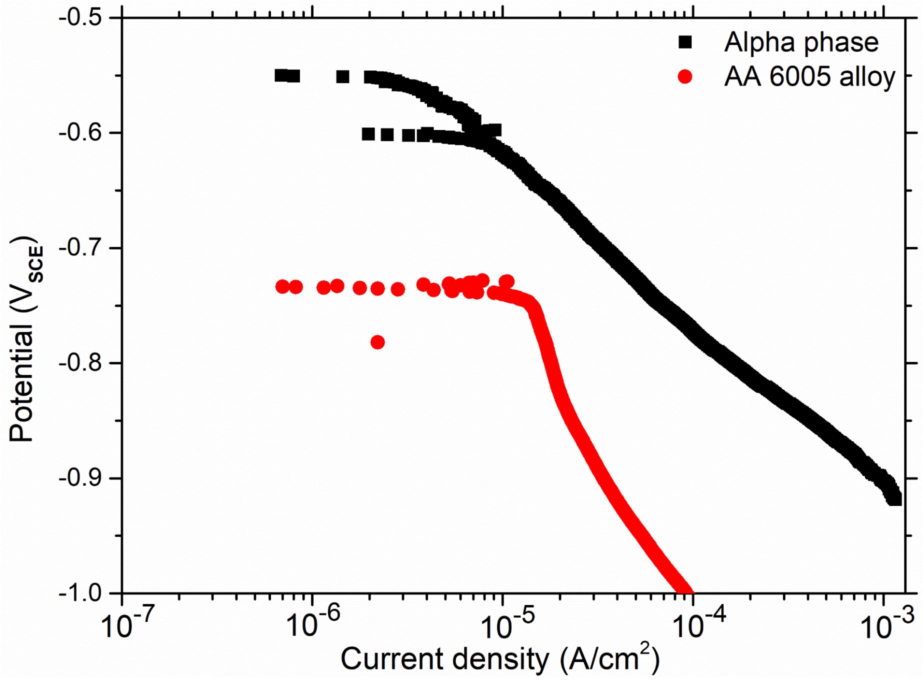

Fig. B4 Cathodic polarization curve of synthesized α-Al(Fe,Mn)Si phase in acidified chloride solution. Cathodic polarization curve for AA6005 alloy is included for comparison.

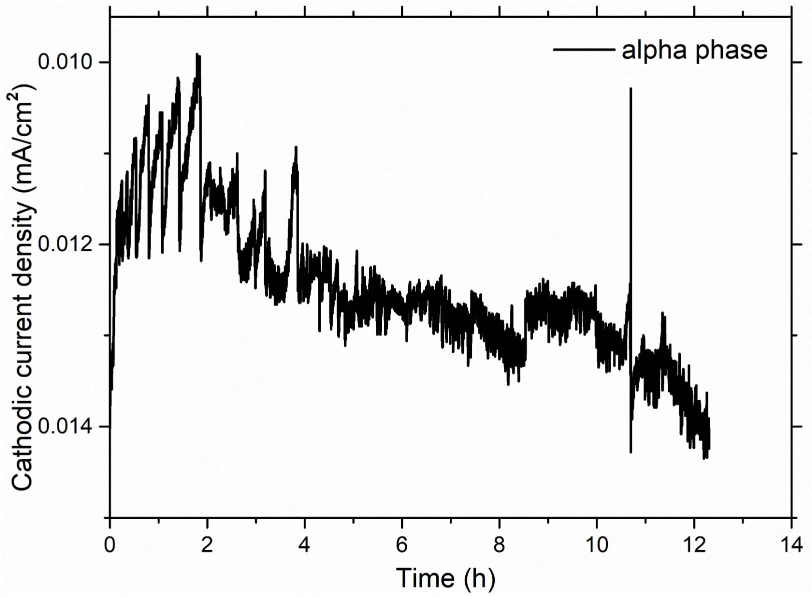

Fig. B5 Cathodic current density due to the potentiostatic polarization of α-Al(Fe,Mn)Si phase at -0.735 V in acidified chloride solution.

B.2 Conclusions

It was observed that the synthetic α-phase without Cu is significantly more noble than the AA6005 alloy. The corrosion rate of synthetic α-phase (without Cu), which was isolated from its matrix, which was formed during its synthesis, was very low as compared to the α-phase with Cu embedded in the AA6005 alloy. Since synthetic α-phase was isolated from the matrix in the above tests, it is difficult to compare it with the α-phase embedded in its 6005 solid-solution matrix. However, it can be concluded from the present study that the α-phase containing Cu in the AA6005 alloy must be more noble than the AA6005 solid-solution matrix when exposed to acidified chloride solution.

B.3 Reference

[1] K. Nisancioglu, Electrochemical behavior of aluminum-base intermetallics containing iron, *Journal of the Electrochemical Society,* 137 (**1990**) 69-77.

Appendix C Additional results on TEM analysis

This appendix presents results from TEM analysis of corroded samples, which are not included in chapter 4, but provide additional evidence for the results shown in chapter 4.

Intermetallic particle analysis

Fig. C1 shows EDS and EELS map of cross-sectional STEM image of a corroded fissure after 24 h corrosion near the surface of a AA6005 sample (see Fig. 4.8). Bright particles in the bulk are uncorroded α-phases as indicated by EDS maps of Al, Fe, Mn, and Si, shown in Fig. C1b, c, d and e, respectively. The elements Fe, Mn and Si were enriched in the particles in contrast to Al, which was depleted. The opening of the corroded grain boundary was filled with oxide (Fig. C1f). Bright particles between the metal and oxide layer are Cu as can be seen both from EDS and EELs analysis in Fig. C1g and h, respectively.

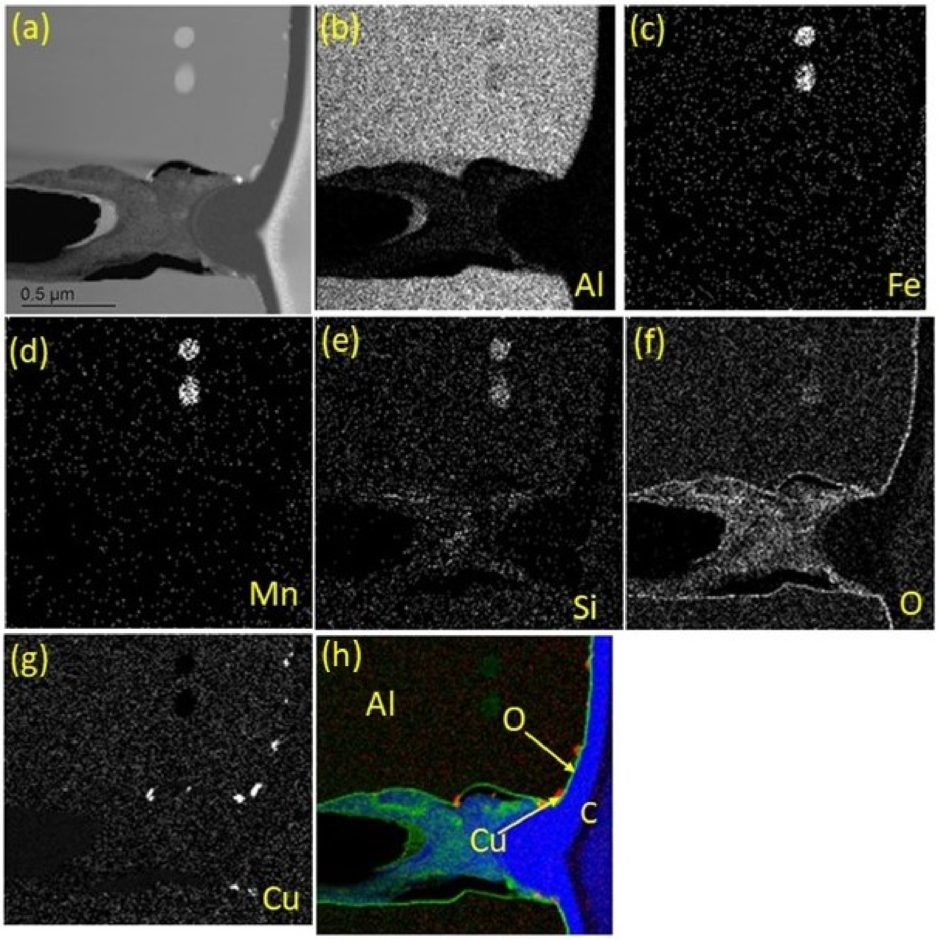

Fig. C1 (a) Annular dark-field (ADF) STEM image of the top surface of the AA6005 sample after 24 h corrosion in acidified chloride solution. EDS mapping of (b) Al, (c) Fe, (d) Mn, (e) Si, (f) O, (g) Cu. (h) EELS analysis for Al, Cu and O of the same analysis area.

Fig. C2a shows further EDS and EELS analyses of selected locations on the same corroded surface as in Fig. 4.8. Fig. C2b and e are the magnified images of yellow and red rectangle in Fig. C2a. EELS map shows the presence of Cu particles at the interface between oxide and metal substrate as shown in Fig. C2c and f. There was no Si enrichment in these Cu particles as can be seen in Fig. C2d and g.

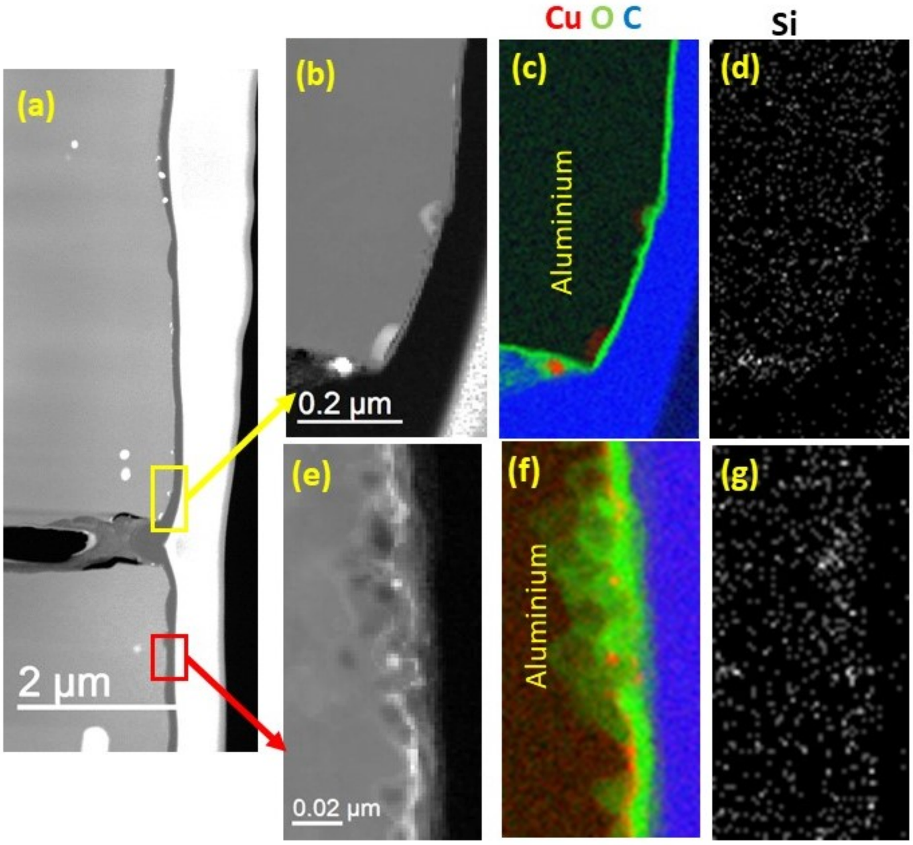

Fig. C2 (a) Annular dark-field (ADF) STEM image of the top surface of the AA6005 sample after 24 h corrosion in acidified chloride solution. (b) ADF STEM image of yellow box in (a) showing Cu particles at the matrix-oxide interface. (c) EELS maps of image (b) where red colour corresponds to Cu, green to oxygen and blue to carbon. (d) EDS map of Si in image (b). (e) ADF STEM image of red box in (a) showing discontinuous metallic Cu particles. (f) EELS map of image (e). (g) EDS map of Si in image (e).

Fig. C3a shows further analysis of the corroded grain boundary discussed in the previous figures. A small area (yellow box in Fig. C3a) is marked on the wall of the IGC fissure is shown in Fig. C3b at higher magnification. EDS (Fig. C3d) and EELS (Fig. C3e) analysis show segregated Cu film along the wall of the corroded grain boundary (Fig. C3d and e). Fig. C3c shows the presence of oxide layer along the corroded grain boundary.

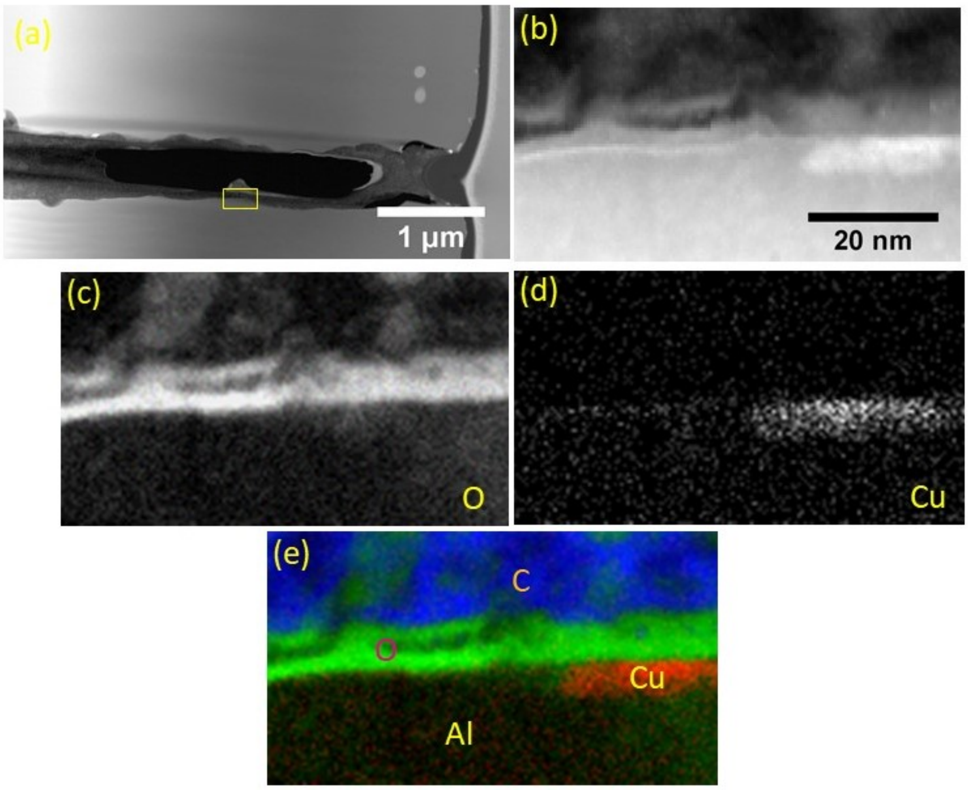

Fig. C3. (a) Annular dark-field (ADF) STEM image of the same corroded grain boundary area of alloy AA6005, shown in the previous figures for further analysis of the corroded walls of the IGC fissure . (b) Annular dark-field (ADF) STEM image of the yellow box in the image (a). EDS mapping of (c) O and (d) Cu. (e) EELS mapping of the image (a).

Fig. C4a shows a STEM image of another fissure wall on the fractured sample which was corroded for 24 h. Fig. C4b is the magnified image of the yellow box in Fig. C4a. EDS and EELS maps show the presence of Cu particles both at the metal oxide interface and the top of the oxide layer (Fig. C4d, e and g). There was no enrichment of Si along these particles (Fig. C4f).

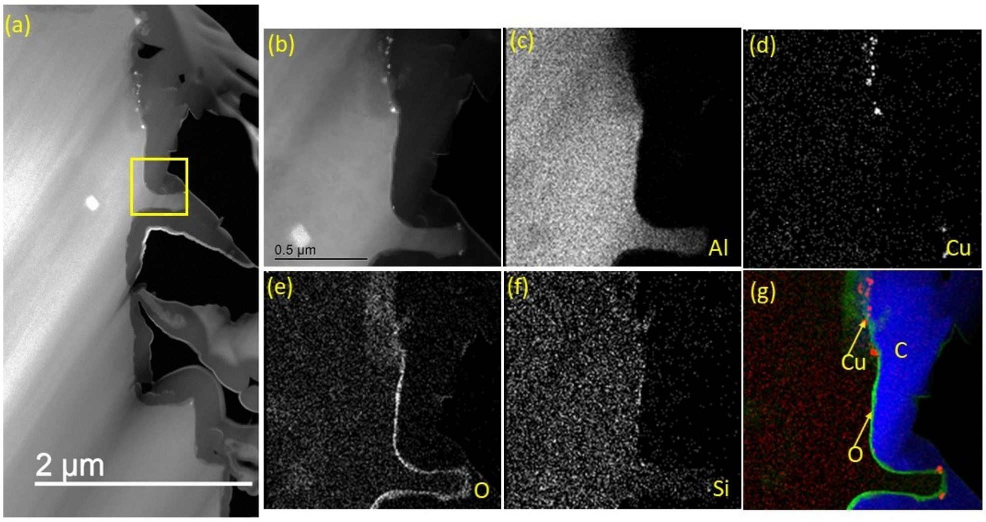

Fig. C4 (a) Annular dark-field (ADF) STEM image of a corroded fissure wall on the fractured surface of an AA6005 sample after 24 h corrosion in acidified chloride solution. (b) ADF image of the yellow box marked on (a) at higher magnification. EDS maps of (c) Al, (d) Fe, (d) Cu, (e) O, and (f) Si in the same area. (g) EELS map of image (b).

Appendix D Additional IGC results for Chapter 5

This appendix presents corrosion test results for as-received and 400 μm alkaline etched surfaces, which were not included in chapter 5. The experimental details are identical to those reported in section 5.2.

As-received surface

As-received surface shows no IGC attack after 1 h of exposure, as shown in Fig. D1a and b. As reported in chapter 3, the induction time for initiation of IGC for this type of surface is about 1 h after immersion. However, since the IGC propagation is not yet significant, it is difficult to detect IGC on cross-section images. After 5 h of exposure localized IGC was observed at 3 or 4 locations (Fig. D1c). Maximum depth of corrosion was around 150 μm as seen in Fig. D1d. After 10 h of exposure, IGC was observed at an increased number of locations (Fig. D1e), and a maximum depth of corrosion was about 260 μm, as shown in Fig. D1f. At larger times of exposure, IGC spread over the entire surface as observed for 15 h, 20 h and 24 h exposed samples as shown in Fig. D1(g, i and k). Maximum penetration depth for 15 h and 20 h exposure was about the same (Fig. D1h and j) as 10 h exposure. With further increase in exposure time, the fissures started penetrating deeper into the material. The deepest attack was found for 24 h corroded sample, which was about 490 μm as shown in Fig. D1l.

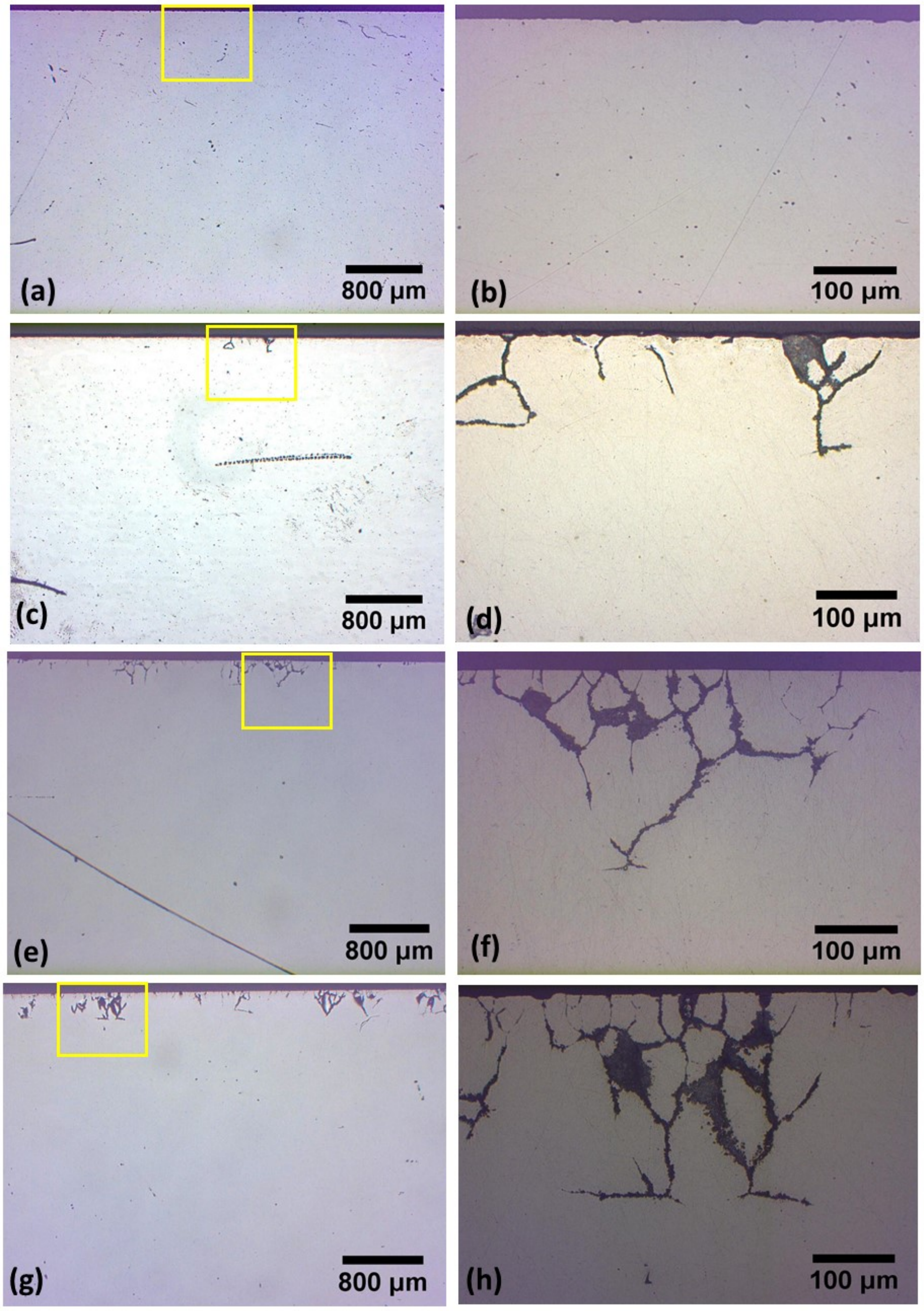
(a)
800 µm
(b)
100 µm
(c)
800 µm
(d)
100 µm
(e)
800 µm
(f)
100 µm
(g)
800 µm
(h)
100 µm

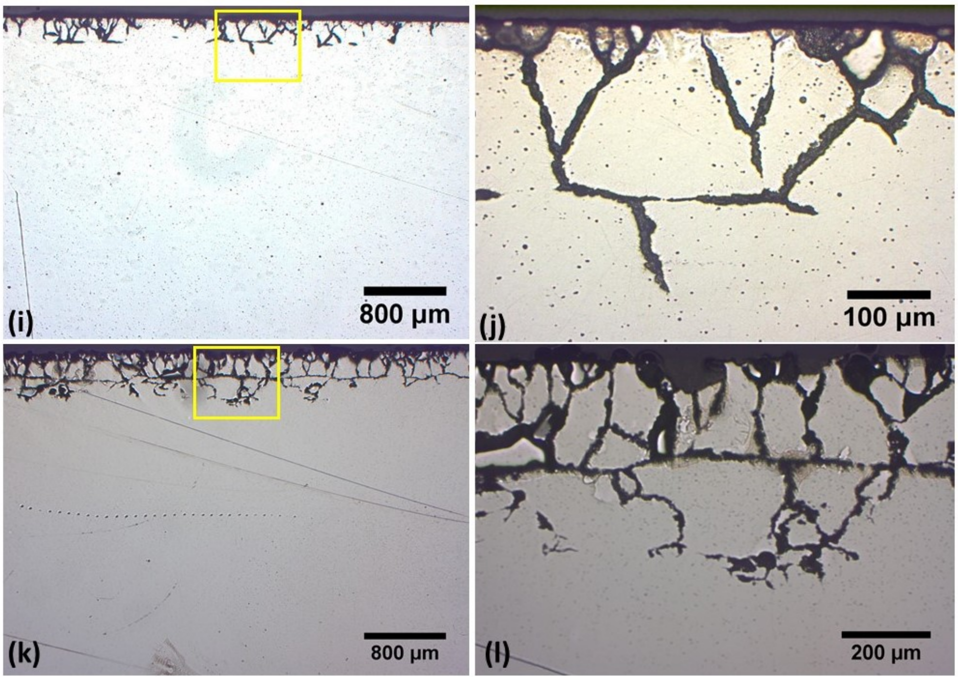

Fig. D1 Cross-sectional optical micrographs of as-received surface after different immersion times in the acidified chloride test solution: (a) After 1 h. (b) Magnified image of area marked with yellow box in (a). (c) After 5 h. (d) Magnified image of area marked with yellow box in (c). (e) After 10 h. (f) Magnified image of area marked with yellow box in (e). (g) After 15 h (h) Magnified image of area marked with yellow box in (g). (i) After 20 h. (j) Magnified image of area marked with yellow box in (i). (k) After 24 h (l) Magnified image of area marked with yellow box in (k).

400 µm milled surface

In this case, the first three-layers of coarse grains were removed by milling thus exposing the finer bulk grain structure (fourth layer) that are randomly oriented to the extrusion direction. In contrast to as-received surface with the coarse-grained layers, 400 µm milled surface shows no IGC attack after 24 h corrosion as shown in Fig. D2.

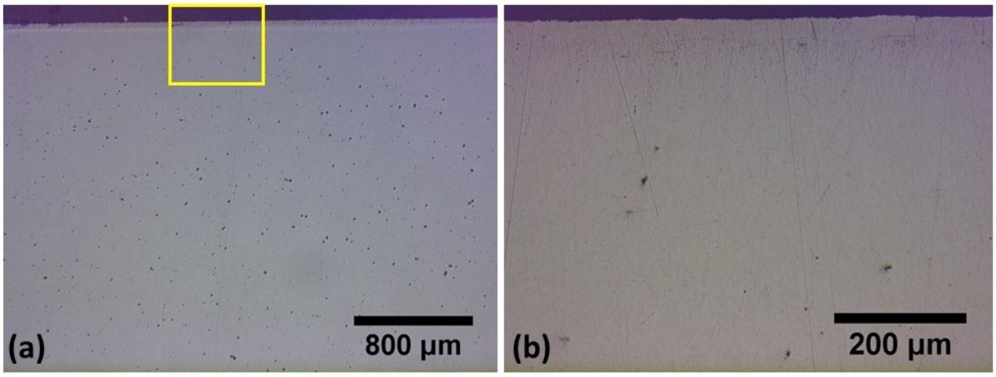

Fig. D2 Cross-sectional optical micrographs after 24 h corrosion test: (a) 400 µm milled surface (without larger recrystallized layer). (b) Magnified image of area marked with yellow box in (a).

As discussed in section 5.3.3 that from the cross-section images it was not very obvious that whether the attack is IGC or pitting. Therefore, the plan view of SEM images is included here to clarify this. Fig. D3a shows the SEM image of 400 µm milled sample that has been corroded for 48 h. It shows that the attack is grain boundary attack (Fig. D3a) while within the grains α-phases are corroded away (Fig. D3b). 400 µm milled surface corroded for 120 h also shows grain boundary attack (Fig. D3c,d).

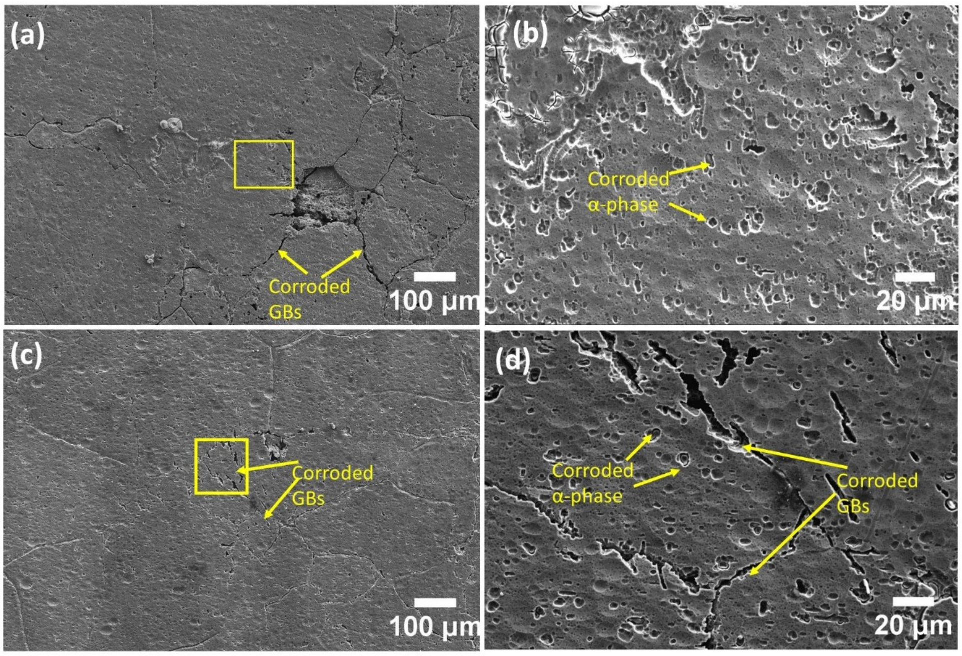

Fig. D3 SEM image of 400 µm milled surface: (a) 48 h corroded surface. (b) Magnified image of area marked with yellow box in (a). (c) 120 h corroded surface. (d) Magnified image of area marked with yellow box in (c).

Alkaline etched surface (400 µm removed layer)

In order to remove a 400 µm layer alkaline, etching was performed for longer time around 80 minutes in 7.5 wt.% NaOH at 55-60 °C followed by 2-5 min desmutting in concentrated HNO_3.

Similar to 400 µm milled surface, alkaline etched surface from which 400 µm layer have been removed shows no IGC attack at 24 h as shown in Fig. D4a.

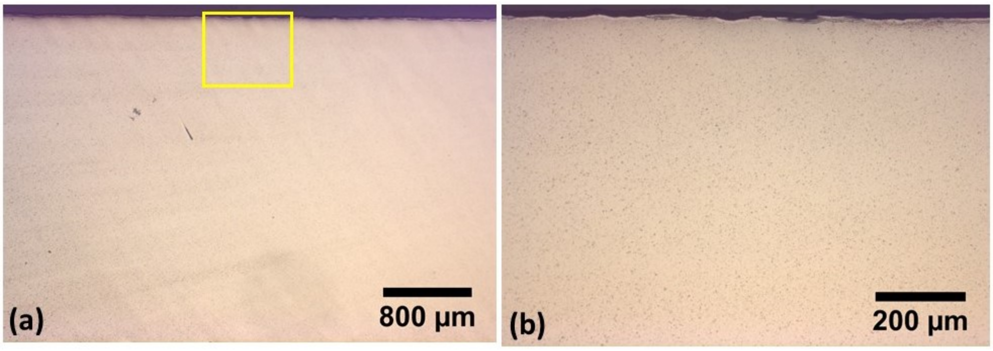

Fig. D4 Cross-sectional optical micrographs after 24 h corrosion test: (a) 400 µm alkaline etched surface. (b) Magnified image of area marked with yellow box in (a).

Localized IGC with around 400 µm propagation depth (Fig. D5a, b) was observed on the 400 µm alkaline etched surface. After that, IGC attack spread both laterally and in depth for 72 h ,96 h and 120 h immersion times as shown in Fig. D5(c,d,e,f,g,h). These results show that irrespective of the procedure used for removing the surface grains (physically or chemically) of around 400 µm layer, obtained IGC results were identical.

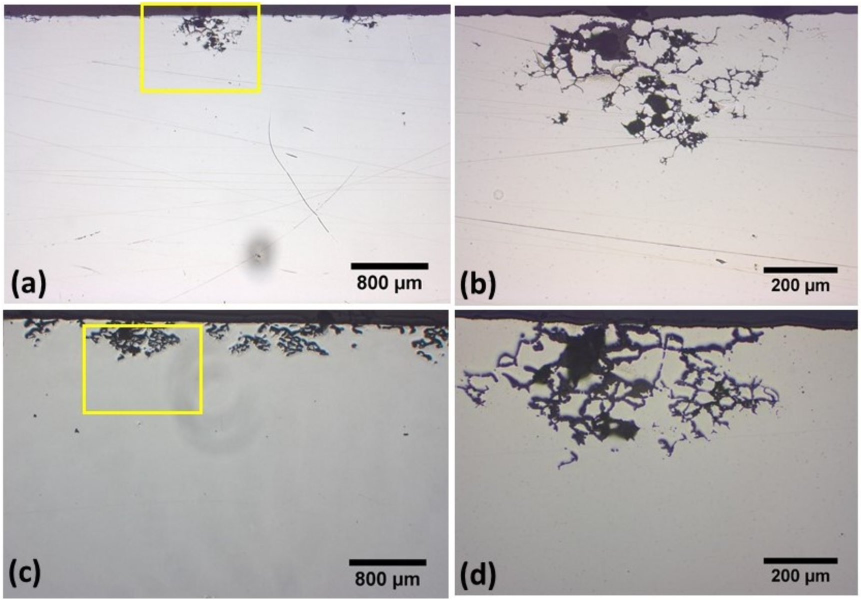

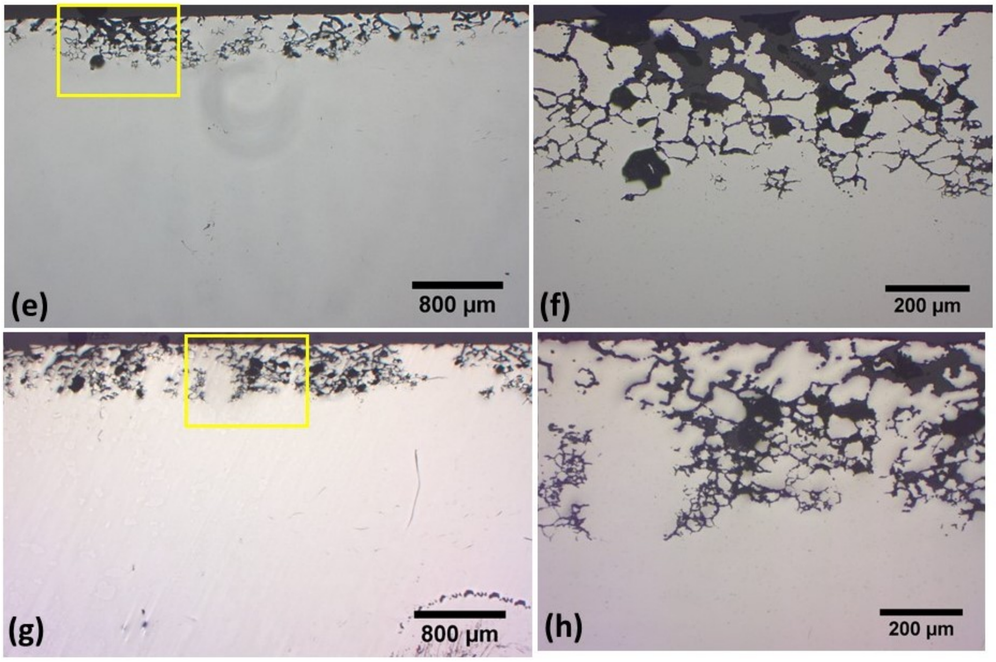

Fig. D5 Cross-sectional optical micrographs of 400 µm alkaline etched surface afterr different immersion times: (a) After 48 h. (b) Magnified image of area marked with yellow box in (a). (c) After 72 h. (d) Magnified image of area marked with yellow box in (c). (e) After 96 h. (f) Magnified image of area marked with yellow box in (e). (g) After 120 h. (h) Magnified image of area marked with yellow box in (g).